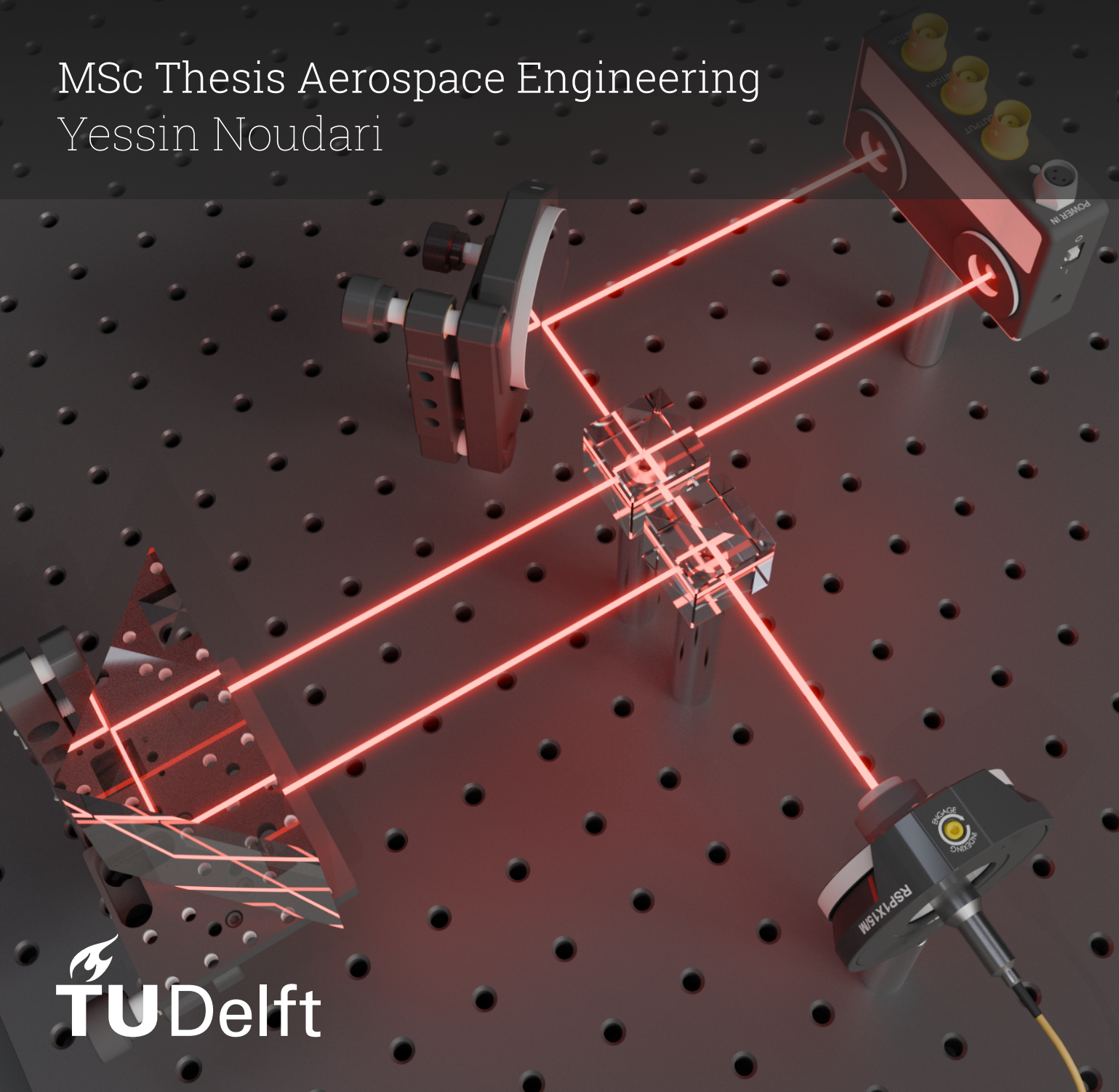


Coherent Free Space Detection for Differential Phase Shift Keying

A Hardware-Based Approach to Optical
Communication

MSc Thesis Aerospace Engineering
Yessin Noudari



Coherent Free Space Detection for Differential Phase Shift Keying

A Hardware-Based Approach to Optical
Communication

by

Yessin Noudari

to obtain the degree of Master of Science
at the Delft University of Technology,

to be defended publicly on Wednesday January 29, 2025 at 9:00 AM.

Student number: 4847814
Project duration: February, 2024 – January, 2025
Thesis committee: S. Speretta TU Delft, Committee Chair
Dr. A. Anisimov TU Delft, Examiner
Dr.ir. Rudolf Saathof TU Delft, Supervisor
Ir. J.J. Spaander TU Delft, Supervisor

Cover: A stylized and simplified rendering of the implemented hardware setup.

An electronic version of this thesis is available at <http://repository.tudelft.nl/>.

Preface

This thesis has been a long time in the making. Not only was conducting hardware-based research much more difficult than I anticipated, I also had to deal with an illness that posed a significant challenge to me. Despite these obstacles, you are reading these words, which means that I have successfully completed what I set out to achieve years ago when I began my studies here in Delft.

The completion of this thesis was done with the help of many others, whom I would like to thank here. Firstly, I want to express my gratitude to my supervisor Rudolf Saathof for his understanding and patience regarding my personal circumstances, as well as for his continued encouragement and support throughout my work on this thesis. I am also grateful for having had the opportunity to work with remarkable hardware.

I also would like to thank my second supervisor, Joshua Spaander, for offering his unique perspective and countless suggestions, which were invaluable. Finally, I want to thank my friends and family, especially my parents, for their support throughout these years. This has been a challenging yet rewarding time in my life, one that has taught me a great deal.

*Yessin Noudari
Delft, January 2025*

Summary

As demand for high-bandwidth data transmission continues to increase, future satellite constellations can leverage the benefits of free space optical communication, which provides significant advantages compared to traditional radio frequency systems. Despite the development of satellite laser communication terminals (LCTs) in recent years, one major challenge remains; coupling the incoming signal into an optical fiber. In addition, most terminals use intensity modulation to encode data, which is limited in its ability to reach high data rates. So-called *coherent* modulation schemes offer superior performance but are not widely implemented in satellite LCT's yet. A system that avoids fiber coupling while using coherent modulation could simplify designs, reduce complexity, and improve performance.

This thesis presents the design, implementation, and evaluation of such a coherent free space optical detection system. Differential Phase Shift Keying (DPSK) was chosen as the modulation scheme due to its balance of power efficiency and implementation simplicity, delivering performance comparable to other coherent schemes with a less complex receiver architecture.

The system was implemented using bulk optics and tested in a laboratory environment. A Delay Line Interferometer (DLI) was selected for DPSK demodulation. The system successfully achieved a data rate of 100 [Mbit/s], demonstrating the feasibility of DPSK-based coherent free space detection. Some performance limitations were identified, with DLI instability emerging as the most notable, which is primarily caused by the long length required for this data rate. This instability resulted in intermittent bit error rate values exceeding the required threshold. These findings show that DPSK demodulation using bulk optics is favored toward higher data rates, and thus shorter delay lines. Recommendations for future work would be to operate at a higher data rate, and implement active stabilization for operational systems.

Contents

Preface	i
Summary	ii
Nomenclature	v
1 Introduction	1
1.1 Problem Background	1
1.2 Research Objective and Questions	2
1.3 Motivation and Contribution	3
1.4 Thesis Outline	3
2 Coherent Detection Systems: Theory and Design	5
2.1 Coherent Modulation Schemes and Receiver Architecture	5
2.1.1 Coherent Detection	6
2.1.2 Delay Line Interferometry	8
2.2 Modulation scheme selection	10
2.3 System Architecture and Components	13
2.3.1 Laser source	14
2.3.2 Intensity/Mach-Zehnder Modulator	14
2.3.3 Modulation Bias Controller	17
2.3.4 Signal Generator	18
2.3.5 Detectors	19
2.3.6 Oscilloscope	20
2.4 Design Choices	20
2.4.1 Data Rate	20
2.4.2 Optical setup design	22
3 System Implementation and Verification	24
3.1 Half-wave voltage determination	24
3.1.1 Low frequency RF half-wave voltage determination	25
3.1.2 Higher frequency RF half-wave voltage determination	26
3.2 Optical Alignment	28
3.3 Bias Control Performance	31
3.4 Verification of DPSK Demodulation	32
3.5 Final Setup and Test Plan	33
4 Results and Discussion	36
4.1 Stability	36
4.2 Communication performance	38
4.3 Discussion	42
5 Conclusion and Recommendations	45
5.1 Conclusion	45
5.2 Recommendations for future work	46
References	47
A Derivations and Calculations	51
A.1 Photodetector current calculation	51
A.2 Incorrect half-wave voltage example calculation	52
A.3 Modulation Transfer Function	53
A.4 Coherence length	54

- A.5 Modulator bias and half-wave voltage determination 55
- B Gaussian Beam Parameters and Simulation 58**
- C Additional Results 62**
- C.1 Setup render 62
- C.2 Communication performance for non-ideal conditions 63
- C.3 Communication performance during stable conditions 67

Nomenclature

Abbreviations

AO	Adaptive Optics
AWGN	Additive White Gaussian Noise
BER	Bit Error Rate
BPSK	Binary Phase Shift Keying
COTS	Commercial Off The Shelf
DC	Direct Current
DLI	Delay Line Interferometer
DPSK	Differential Phase Shift Keying
DSP	Digital Signal Processing
FR	Functional Requirement
FSK	Frequency Shift Keying
FSO	Free Space Optics
FSOC	Free Space Optical Communication
IF	Intermediate Frequency
IM/DD	Intensity Modulation/Direct Detection
IR	Infrared
LEO	Low Earth Orbit
LCT	Laser Communication Terminal
LO	Local Oscillator
MBC	Modulation Bias Controller
MS	Modulation Scheme(s)
MZM	Mach-Zehnder Modulator
NDF	Neutral Density Filter
NFR	Non Functional Requirement
OOK	On-Off Keying
OP	Operating Point
OPPL	Optical Phase-Locked Loop
PER	Packet Error Rate
PLL	Phase-Locked Loop
PoISK	Polarization Shift Keying
PPM	Pulse Position Modulation
PRBS	Pseudo Random Binary Signal
PSK	Phase Shift Keying
QAM	Quadrature Amplitude Modulation
QPSK	Quadrature Phase Shift Keying
RF	Radio Frequency
SNR	Signal to Noise Ratio
SWaP	Size, Weight and Power
TBIRD	TeraByte InfraRed Delivery

Symbols

Symbol	Definition	Unit
A	Electric field amplitude	[-]
B	Bandwidth	[Hz]
c	Speed of light	[m/s]
E	Electric field	[V/m]
f	Frequency of electrical input signal	[Hz]
i	Photocurrent	[A]
I	Irradiance/Intensity	[W/m ²]
j	Imaginary unit	[-]
L_0	Center of Gaussian probability distribution	[-]
L_c	Coherence Length	[m]
L_{DLI}	Delay Line Interferometer length	[m]
P	Power	[W]
\mathcal{R}	Responsivity	[A/W]
R_B	Data Rate	[bit/s]
t	Time	[s]
T	Period	[s]
V	Voltage	[V]
V_0	Electrical signal amplitude	[V]
V_π	Half-wave voltage of the MZM RF port	[V]
$V_{\pi,DC}$	Half-wave voltage of the MZM DC port	[V]
α	Angle between the reference and delayed beam	[rad]
η_B	Bandwidth efficiency	[bit/s/Hz]
η_p	Power efficiency	[-]
θ	Phase or rotation angle	[rad]
λ	Optical wavelength	[nm]
ν	Frequency of light	[Hz]
σ	Standard deviation	[-]
ϕ	Phase	[rad]
ϕ_0	Bias phase drift of the MZM	[rad]
ϕ_{bias}	Bias phase delay of the MZM	[rad]
φ	Rotation angle	[rad]
φ_{DLI}	Delay Line Interferometer phase change	[rad]
ω	Angular frequency	[rad/s]

1

Introduction

1.1. Problem Background

Since the introduction of fiber optic communication, the global communication landscape has changed drastically, showing an ever growing demand in data, with estimates predicting the internet to grow by 30% each year. Specifically, a large part (70%) of internet users will be connected via mobile. [1] Mobile networks using 5G technology will play an important role in accommodating this growth. But coupled with an increasing number of devices that will need to be connected, massive amounts of data still need to be transmitted between data centers and access networks. A promising alternative to fiber optic links is the use of Free Space Optics (FSO), which has seen increasing interest in the last decade and can alleviate this issue. [2]

This growing demand is applicable not only to terrestrial optical networks, but also to satellite communication. For satellites, the increasing data bandwidth requirements are driven by consumer demand and the generation of more onboard data due to more and higher resolution instruments. [3, 4] Most of the current communication with satellites is done using the radio frequency (RF) spectrum. However, there are many limits to RF that hinder a substantial increase in data rate and bandwidth. Switching to the optical domain has many advantages such as smaller communication terminals, less weight, less power, higher frequency (and thus higher data rates), no licensing requirements, and finally a narrower beam that ensures a more secure channel. [5–8]

In the last decade, the space sector has seen an upward trend in the use of smaller satellites due to their cheaper development and launch costs. Because these smaller satellites are often restricted in size, weight and power (SWaP), laser communication terminals (LCT) are a well-suited option to replace RF terminals. Indeed, this is already being used as inter-satellite links for Low Earth Orbit satellite constellations (e.g. Starlink). In addition to inter-satellite links, the use of FSO has the same advantage for ground-to-orbit communication, and we are currently seeing implementation on nanosatellite form factors like the CubeSat. Several LCT's have been developed for CubeSat size, which predominantly focus on downlink, not uplink. A compilation of recent state-of-the-art LCT's for CubeSat platforms can be seen in the table below.

Table 1.1: Overview of the current State of Art LCT's for CubeSat format satellites. Source: [9, p. 248, Table 9-5].

Terminal	Launch Year	Data Rate [Mb/s]	Mass [kg]	Power [W]	Size [U]	Modulation
OCSD-B&C	2017	200	<2.3	20	1.5	OOK
VSOTA	2019	1	<1	4.33	-	OOK/PPM
OSIRIS4	2021	100	0.4	10	0.3	OOK
TBIRD	2022	200,000	<3	100	3	QPSK
CLICK-B/C	2022	20	1.5	30	1.2	PPM
CubeCat	2023	1000	<1.33	15	1	OOK

Most of these share a similar SWaP and modulation scheme, with the exception being NASA's TBIRD (TeraByte InfraRed Delivery), which has a higher SWaP in combination with a more advanced modulation scheme to achieve a higher data rate. The other LCT's use modulation schemes like On-Off Keying (OOK) and Pulse Position Modulation (PPM), which are relatively simple to implement. OOK works by encoding binary data in the power of the optical signal, where a 0 and a 1 represent low and high power, respectively. PPM works in a similar way, but instead the bits are encoded in the length of pulses. Both OOK and PPM can be classified under Intensity Modulated/Direct Detection (IM/DD) schemes and are not optimal in terms of power and bandwidth use.

NASA's TBIRD makes use of a modulation scheme called Quadrature Phase Shift Keying (QPSK). This modulation scheme encodes bits by varying (shifting) the phase of the optical signal in 4 different states ($0^\circ, 90^\circ, 180^\circ, 270^\circ$). Phase Shift Keying (PSK) modulation schemes require an optical signal whose phase relation is consistent over the link distance. This property is referred to as *coherence*. Coherent modulation schemes enable higher data rates than the simpler IM/DD schemes. NASA's TBIRD demonstrates that it can reach much higher data rates with a proportionally smaller increase in power.

The CubeSat design principle of using predominantly Commercial Off-The-Shelf (COTS) components also extends to the design of LCT's. The use of existing highly developed terrestrial fiber optic technology within satellite LCT's enables high data rates (upwards of 100 Gbit/s) at modest costs. [10] Furthermore, using individual components facilitates the separation of transmitter and receiver elements from optics. Consequently, this enables the use of components such as erbium-doped fiber amplifiers, increasing design flexibility, and overall increasing performance and reducing complexity, energy consumption, and costs. [11, 12]

However, utilizing COTS fiber optic components does come at a cost; to use them, the received signal must first be coupled into optical fiber, which results in significant signal losses, and this is often remedied with fiber amplifiers. For high data rates, these additional costs can be justified, but less so for links aiming for lower data rates and SWaP, where complexity plays a bigger role. [13] For coherent detection in particular, the signal must be coupled into single-mode fiber [12], which is more susceptible to pointing errors and atmospheric turbulence than multi-mode fiber or free space detectors [14]. The bigger width of multi-mode fiber allows for a higher field-of-view and less coupling loss, but requires additional optical devices to transform to single-mode fiber for correct detection. [15]

To mitigate coupling loss and atmospheric disturbances, FSO systems can make use of Adaptive Optics (AO). Basic forms of AO, like tip-tilt correction, are used to counteract atmospheric disturbances and align the spot for coupling into fiber. More advanced AO systems, which use a wavefront sensor and a deformable mirror, can further minimize the spot size, producing a diffraction-limited image. [12] For this reason, advanced AO systems are highly effective in increasing the coupling efficiency. [10, 16]

Still, the implementation of advanced AO systems is not straightforward and its use is "intricate and expensive", which should raise the question whether it is avoidable. [17] For the current development of LCTs, the cost of AO is not yet an issue since high data rate optical satellite communication is not done on large scales. It therefore makes sense to use COTS fiber based transceivers, since they have already been qualified for use in space, which saves time and money required for design and testing of custom components. However, for future optical links, the avoidance of fiber coupling could prove to be beneficial. Since photodiodes are larger than the core of a single mode fiber (depending on the bandwidth), many constraints could be eased, simplifying the system design.

Receiver systems that do not require fiber coupling are referred to as 'free space detectors'. So far, there is no literature showing what a coherent free space detection system would look like in small form factor satellites such as CubeSats. Many studies have been conducted on coherent FSO systems for terrestrial links, but none with a focus on systems that do not use fiber coupling.

Understanding how coherent free space detectors can be implemented and how they perform is a first step in evaluating their potential as an alternative to fiber coupling for future LCT design.

1.2. Research Objective and Questions

The research objective for this thesis is to:

Design, implement, and evaluate a coherent free space optical detection system using bulk optics, demonstrating functionality through the establishment of a communication link.

Research Questions

To achieve the objective mentioned above, the following research questions were addressed.

1. Which coherent modulation scheme is most suitable for hardware implementation in a free space optical communication system for this thesis?
2. How can a coherent free space optical detection system be designed and implemented in a laboratory environment using bulk optics?
3. What is the performance of the implemented detection system?

To assess whether the communication link is functional, several requirements were formulated and summarized below.

Table 1.2: Functional and Non-Functional Requirements (FR, NFR).

Requirement Label	Description
FR1	The communication link shall attain a data rate of at least 100 [Mbit/s].
FR2	The communication link shall achieve a maximum Bit Error Rate (BER) of 10^{-3} before error correction.
FR3	The communication link shall use a coherent modulation scheme.
FR4	The receiver system must correctly demodulate the chosen coherent modulation scheme, ensuring that the modulation type is as specified and not an unintended scheme (e.g., OOK).
FR5	The receiver shall not use fiber coupling to detect the signal.
NFR1	The communication link shall be implemented using only hardware that is already available to the Aerospace Engineering Faculty.
NFR2	The communication link shall comply with laser safety standards.

1.3. Motivation and Contribution

Recently, the Aerospace Engineering faculty of Delft University of Technology has installed a Mini Optical Ground station to facilitate research for its laser satellite communications group. Its main purpose is to provide an environment for testing and developing novel FSOC related technologies. Although it is currently not operational, many of the key hardware equipment for FSOC is already available. However, an optical coherent (free space) detection setup has not yet been realized. The work performed in this thesis will be the first implementation of such a system at the Aerospace Engineering Faculty. In this context, the work that has been done serves two primary purposes (in addition to addressing the research gap):

- Provide practical knowledge on how to implement a coherent free-space detection setup using bulk optics. The setup that has been implemented will serve as a proof-of-concept and a reference point for researchers and students attempting to build similar systems. In addition, many of the potential pitfalls identified during this thesis can be avoided.
- Offer an assessment of its performance, so that researchers and students can decide if it is worthwhile to perform further research into coherent free space detectors as an alternative to fiber coupling. Consequently, it reduces the risk that researchers invest significant time and resources to explore this approach without first understanding its feasibility of implementation and baseline performance.

1.4. Thesis Outline

This thesis is structured to present, in sequence, the design, implementation, and evaluation of a free space optical detection system using a coherent modulation scheme. In chapter 2, the background

of coherent modulation schemes and their receiver architectures are introduced, with an emphasis on PSK. Following this, the modulation scheme is chosen. Based on this modulation scheme, a receiver architecture is proposed with the selection of the components that are needed. Lastly, several choices are made and motivated to finalize the system design, such that it can be implemented using hardware.

Chapter 3 covers the implementation and verification of the chosen receiver architecture, performing several tests to ensure functionality.

The results of the hardware setup are presented in chapter 4, which mainly constitute the stability of the system and the communication performance in terms of Bit Error Rate (BER). The discussion offers explanations for some challenges encountered during testing.

Finally, chapter 5 summarizes the conclusions of the research and offers recommendations for future work.

2

Coherent Detection Systems: Theory and Design

This chapter will answer the first two research questions; *What* modulation scheme is most suitable and *how* it can be implemented. Firstly, which modulation scheme is most suitable for hardware implementation will be discussed. In the first section, background for coherent modulation schemes is established. Using this background, in the second section, the most suitable modulation scheme is chosen using a trade-off, resulting in the final selection for this thesis.

With this selected modulation scheme, its hardware implementation can be detailed. This is done first by proposing the general system architecture and describing the function and specifications of the chosen components. Subsequently, in the fourth section, on the basis of the constraints of each component, several design choices are made regarding the data rate and optics.

2.1. Coherent Modulation Schemes and Receiver Architecture

To communicate data via an optical signal, modulation schemes (MS) must be employed. Of the MS used in FSO communication, IM/DD schemes like On-Off Keying (OOK) and Pulse Position Modulation (PPM) are the most widely used because of their simplicity and low costs. [18–20] IM/DD works by encoding information in the intensity of light, where a photodetector translates the received optical energy into an electrical signal. Because IM/DD only uses the amplitude as a degree of freedom, it limits the maximum amount of information that can be encoded into the modulated signal. For fiber optic communication, these MS have started posing significant challenges at higher data rates (>40 [Gbit/s]), which is primarily due to the high bandwidth it occupies.

The amount of bandwidth that a MS occupies relative to the data rate is also known as the *spectral efficiency*. One way to increase the spectral efficiency is to encode information into light other than its intensity, such as the phase, frequency, and polarization. Modulation schemes that use any (or a combination) of these are referred to as coherent MS. Popular coherent MS for fiber (and FSO) communication are Phase Shift Keying (PSK), Quadrature Amplitude Modulation (QAM), and Polarization Shift Keying (PoSK). [21]

PSK is a MS that encodes data by changing the phase of a constant frequency carrier wave. In PSK, the phase of the light wave is modulated to represent different symbols. Common forms of PSK include Binary Phase Shift Keying (BPSK) which uses two phases ($0^\circ, 180^\circ$) to encode one bit per symbol and Quadrature Phase Shift Keying (QPSK) which uses four phases to encode two bits per symbol. The simpler BPSK MS is illustrated in Figure 2.1.

QAM is a MS that makes use of both amplitude and phase-shift keying to encode the data. This allows for a higher number of symbols and thus higher data rates. PoSK modulates the state of polarization of the light wave to encode data, but is used to a lesser extent than the others.

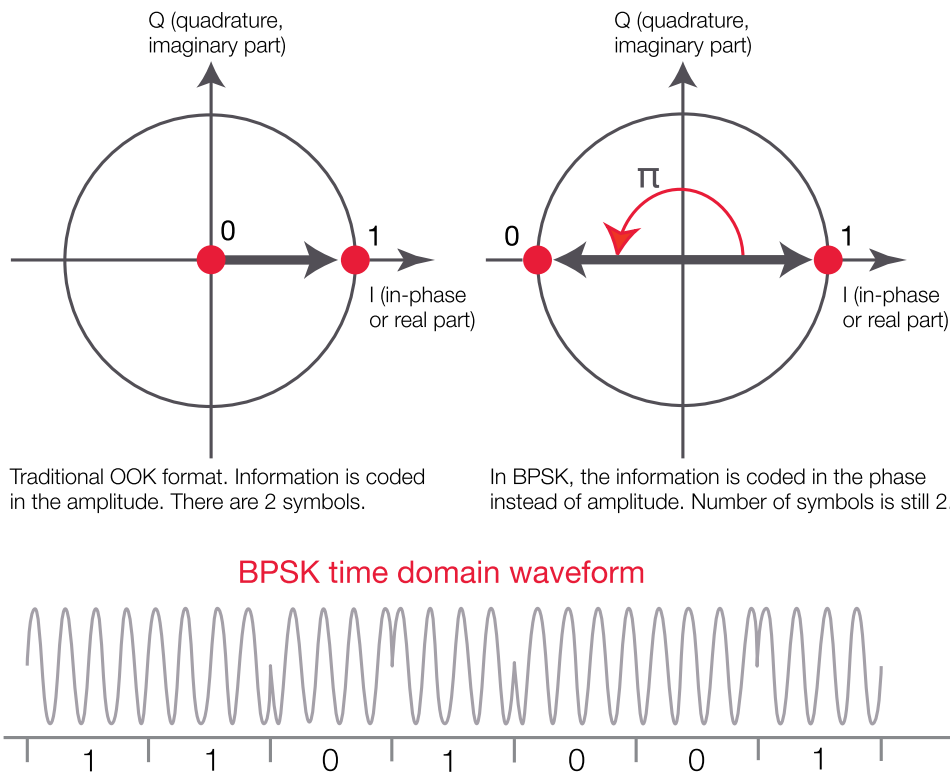


Figure 2.1: Diagram showing the constellation diagram of OOK (left) and BPSK (right). The time domain shows the phase shift of π (180°) that represents the changing of a bit. Source: [22, p. 16].

The main advantage that coherent MS offer is better spectral efficiency and higher power efficiency. As a result, it enables higher data rates than IM/DD schemes. [7, 21]

To detect a phase change from a coherent signal, simply using a photodiode does not work, since it can only convert the intensity of light into an electrical signal. The detection of coherent optical signals can be categorized into two groups:

1. Use of a coherent detection technique and signal processing.
2. Use of a Delay Line Interferometer (DLI).

Each detection method is discussed in the following sections.

2.1.1. Coherent Detection

Optical coherent detection was proposed in 1960, but a significant research interest emerged in the 1980s, when it became clear that it offered significant advantages over IM/DD. [23] The implementation of optical coherent detection was still costly and complicated however, and the concurrent progress on IM/DD systems reduced the need to commercialize coherent detection.¹[24] Only since the early 2000's has coherent detection seen more commercial use, mainly due to the progress of advanced digital signal processing (DSP). [25, 26]

The principal concept behind coherent detection is to mix the incoming modulated optical signal with a local oscillator (LO) that serves as a phase reference and allows for the complete recovery of the signal's amplitude and phase information. By having an absolute phase (and frequency) reference, any modulated changes in phase or frequency can be measured. In Figure 2.2, a basic block diagram of a coherent detector can be seen.

¹The main progress for IM/DD systems at the time can be attributed to: the introduction of cost effective EDFA's, and the use of wavelength division multiplexing both of which increased the data rates and reach of the links. [24, 25]

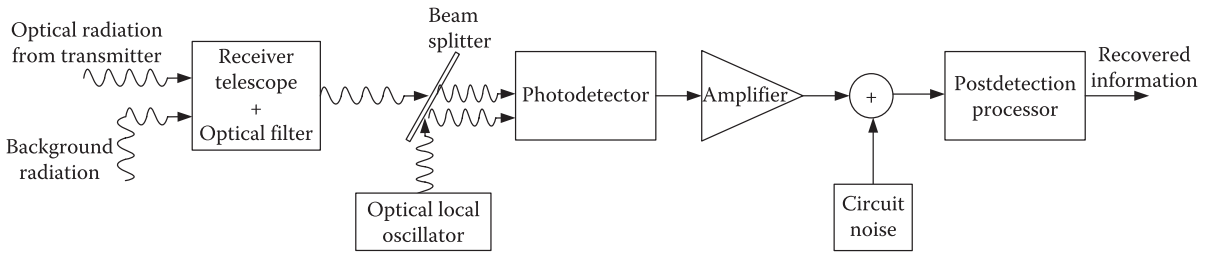


Figure 2.2: Block diagram of an optical coherent detector. Source: [20, p. 64].

By combining the modulated signal and the LO signal, the combined signal has some properties that make coherent detection favorable. To illustrate this, consider Equation 2.1 for the power output of the combined signals.

$$\begin{aligned} \text{Homodyne : } P(t) &= P_s A_s^2 + P_l + 2\sqrt{P_s P_l} A_s \cos(\theta_s(t) - \theta_l(t)) \\ \text{Heterodyne : } P(t) &= 2\sqrt{P_s P_l} A_s \cos((\omega_s - \omega_l)t + \theta_s(t) - \theta_l(t)) \end{aligned} \quad (2.1)$$

where A, P, ω, θ are the amplitude, power, angular frequency, and phase with subscripts s and l to indicate the carrier signal and LO respectively.²

Two distinct equations emerge based on the relationship between the local oscillator (LO) frequency and the modulated signal frequency. When equal, the intermediate frequency (IF) is 0 and this is called *homodyne* detection. When the modulated signal and the LO frequency are different (in the order [GHz]), it is referred to as *heterodyne* detection. Looking at both equations, the term that contains the data is the \cos term, which can be amplified by increasing the LO power P_l .

This property is uniquely different from amplifying the electrical signal after detection because of how noise interacts with the optical signal. The only noise source that is introduced by increasing the LO power is the shot noise, which arises from the randomness of photon arrivals on the photodetector. Increasing the LO power increases the shot noise, but other noise sources in the circuit such as background noise, dark current noise, and thermal noise remain constant. Therefore, by increasing the LO power, the shot noise starts to suppress the other noise sources, increasing the signal to noise ratio (SNR). This allows coherent detection to become *shot noise limited*, and combined with an increased photocurrent, this improves the SNR and thus reduces the BER. [18, 20, 27]

However, the use of an LO makes coherent detection more complex and expensive, which has been and is still the primary reason why it has not overtaken the use of IM/DD in optical links (both fiber and FSO).

The reason an LO makes coherent detection more complex is because additional hardware and circuitry is needed to ensure it functions correctly. In the case of homodyne detection (where $\omega_s = \omega_l$), the LO frequency must be synchronized with the modulated signal frequency, as well as tracking/matching the phase noise of the signal (ignoring the intended phase modulation) and can be achieved using an optical phase locked loop (OPPL). [26] This comes with the benefit of an increase in SNR of 3 [dB] compared to heterodyne detection.³ [24] However, combined with other requirements like a lower laser linewidth, homodyne detection is more costly and is why heterodyne receivers are more commonly used.

For heterodyne detection, a free-running LO can be used, where the second-stage demodulation is performed in the electrical domain, using a phase-locked loop and the aforementioned DSP approach. The basic receiver architecture of homodyne and heterodyne detectors for PSK MS can be seen in Figure 2.3.

²For the derivation of both equations, see section A.1.

³This is only the theoretical increase, which is around 2 dB lower in reality because of several implementation losses that are hard to overcome in homodyne systems. [16, p. 136]

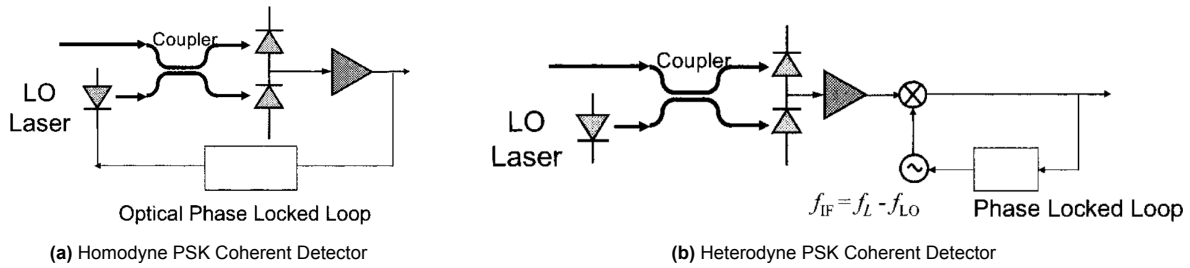


Figure 2.3: Main receiver structures for an optical BPSK signal. Source: [28, p. 7].

Although coherent detection can be performed with a single-branch receiver (as seen in Figure 2.2), this is neither commonly used nor most optimal. Instead, the receivers shown above use two photodiodes to measure the difference between the two, and this is referred to as *balanced detection*. A balanced detector is preferred for several reasons. Firstly, a balanced detector can remove the DC components, which would normally be done using additional filters. Secondly, by the subtraction it performs, it can also suppress the LO noise present in the two signals. [26, p. 296] [29, p. 185]

In addition to the aforementioned coherent detection techniques, many different variations exist. Some are briefly discussed here.

A variation of heterodyne detection is *intradyn detection*, which has a smaller frequency difference between the two signals, lowering the bandwidth requirements of receiver components such as photodiodes and amplifiers. [24]⁴ Because the LO runs unsynchronized with the carrier signal, a similar electronic DSP carrier recovery approach must be applied, but now requires a lower processing bandwidth. Intradyn detection performs similarly to ideal homodyne detection with an optical phase-locked loop (OPLL). [30, 31]

Another variation is *self-coherent detection*, which does not require the use of an LO at the receiver end and is instead moved to the transmitter side. On the transmitter side, both the modulated signal and the reference signal (or pilot tone) are propagated. This effectively reduces system hardware complexity and costs at the receiver end. One disadvantage is that it requires more complex signal processing and suffers from poor power efficiency (because the transmitter has to expend power on the pilot tone). [32–34] In addition, the pilot tone will be impacted by the same atmospheric distortions as the primary signal, which is avoided when using a LO.

Because coherent MS are investigated here for use in the context of FSO, several advantages of coherent detection are summarized below:

- Suppresses and rejects background noise well. [7, 19, 21]
- Increases receiver/detector sensitivity. To be precise, when bandwidth limited, coherent detection achieves the *best* sensitivity. [7, 19, 35]
- Is more resistant to atmospheric turbulence in general when DSP is used for phase correction.

Secondary advantages that result from increased sensitivity are; suppressing scintillation [36, 37], and helping to reduce the outage probability. [18, 38]

The primary disadvantage to coherent detection is that it is more complex than IM/DD. In addition to the circuitry required to drive the LO at the receiver end, the carrier recovery techniques require either an OPLL or an advanced DSP approach, both of which are not needed for IM/DD.

2.1.2. Delay Line Interferometry

The second way to detect coherent optical signals is to use a delay line interferometer (DLI), which converts phase information into intensity information by interfering the received optical signal with a

⁴Intradyn detection uses an intermediate frequency which is small enough to be in the signal bandwidth. An exemplary simulation uses a frequency offset of 100 MHz for intradyn detection. [30] In contrast the frequency difference for heterodyne detection is in the range of GHz.

delayed version of itself. This is illustrated in an example where a BPSK signal is delayed by a 1 bit duration in Figure 2.4.

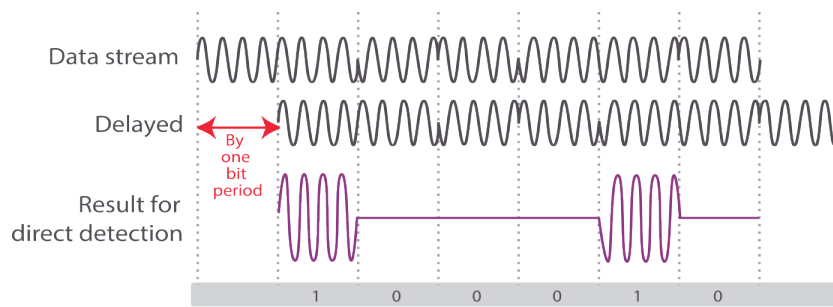


Figure 2.4: Time waveform of a BPSK signal that is delayed by 1 bit period. When interfered with itself, a phase change between the signals results in an intensity modulated signal that can be detected directly. Adapted from: [22, p. 17].

When the two signals share the same phase constructive interference occurs. Destructive interference occurs when they are 180° out of phase. In this way, the phase difference between consecutive symbols is converted into an intensity signal. So even though there is no knowledge about the absolute phase of the signal, the phase *change* can be known.

This method is called *differentially coherent detection* and when applied to PSK schemes, it is called Differential Phase Shift Keying (DPSK). The basic receiver architecture for DPSK can be seen in Figure 2.5, where the receiver on the left uses the DLI and the one on the right the previously discussed coherent detection method. Figure 2.5.

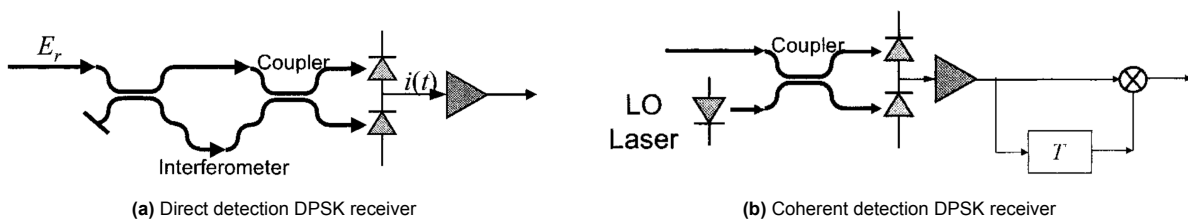


Figure 2.5: Main receiver structures for an optical DPSK signal. Source: [28, p. 9].

The DLI detection method can be performed for any order PSK scheme and even a variation of QAM, but requires either two (or more) DLI's or more complex hybrid couplers. [39] For the sake of simplicity, Binary DPSK will be referred to as DPSK unless stated otherwise.

Again in the receiver structure, the balanced detector is present. For differentially coherent detection of PSK, a balanced detector is required to obtain the full benefit of the MS. The performance of the balanced detector for a DLI is highly dependent on the phase difference that is introduced. A DLI needs to perform two functions; create a delay equal to one bit duration, and a phase shift that ensures optimal interference conditions. This can be seen in Figure 2.6.

The phase change introduced in the DLI should be equal to $\pm 90^\circ$ ($\pm \frac{\pi}{2}$), such that the additional phase change of 90° created by the coupler results in complete constructive and destructive interference on either branch. This can be seen in Figure 2.7, where the coupler is modeled as a beamsplitter. In this way, when constructive and destructive ports are subtracted from each other, the SNR increases by a factor of 2 (or 3 [dB]).

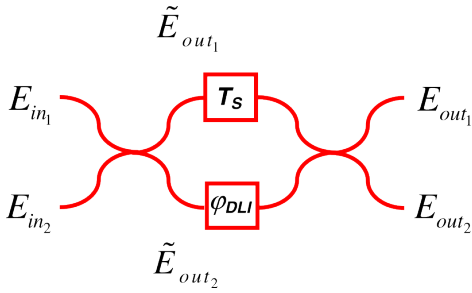


Figure 2.6: Structure of a Delay Line Interferometer (DLI), where T_s is the bit period and φ_{DLI} is the phase shift in one of the branches. Source: [39, p. 61].

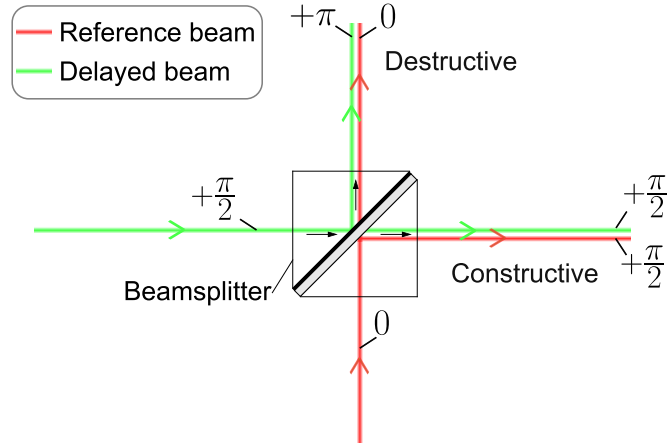


Figure 2.7: Overview of the reference and delayed beam combining in the final coupler of a Delay Line Interferometer (DLI). The constructive and destructive port are created by a $\pi/2$ phase change in the DLI and the $\pi/2$ created by the beamsplitter.

For the performance of DPSK, the DLI imposes the most stringent requirements, where the main one is that the branches must be stable to a small fraction of a wavelength such that φ_{DLI} stays at $\pi/2$. The tuning of this phase change in the DLI in a laboratory setting can be done by manually tweaking the length with an accurate translation stage. For operational use in real systems, passive stabilization is not sufficient, and some form of stabilization is required. This is either done by tracking the phase with PLL's or using an amplitude modulated pilot tone. [29, p. 203]

2.2. Modulation scheme selection

With the essential understanding of the coherent MS established, the most suitable option is chosen to answer research question 2. This selection process involves multiple criteria and the weighing of various trade-offs.

Many studies have been conducted on the influence of modulation techniques/schemes on the performance of FSO communication links. However, comparing studies is difficult because there are many factors that influence the results, such as the precise channel model, turbulence strength, detection schemes, link distance, noise levels, component specifications, etc. Therefore, it is more useful to look at studies focused on a direct comparison of MS and use these results to form an overall conclusion.

In comparing MS, a metric that is often used is the BER to SNR relationship. Although this is a useful metric that relates the transmitter power to the bit errors, it is not enough to make a decision. One reason is that each study has a highly specific set of variables and may not translate to the use case that is of interest. Therefore, it is imperative that a set of criteria is used.

A set of selection criteria originates from functional requirements and desirability for MS in general. Based on existing literature and key requirements, the chosen selection criteria are listed below. [20, 40, 41]

- **Power efficiency:** Because power is ideally minimized (to reduce mass/volume), it plays a role in choosing the MS. One can imagine that each MS has a different average power depending on how it encodes data. In the aim of defining the power efficiency, it is best to consider the average power required that is related to a certain BER and SNR. In mathematical terms, the power efficiency (η_p) is defined as the average power required to achieve the desired BER at a specified data rate:

$$\eta_p = \frac{E_{pulse}}{E_b} \quad (2.2)$$

where E_{pulse} and E_b are the energy per pulse and the average energy per bit, respectively. [20]

- **Spectral efficiency:** In theory one can transmit with an unlimited bandwidth. However, reality does not permit this due to the limitations of transmitters, detectors and distortions. The trade-off

between the two often arises when MS with high spectral efficiency require more power due to their complexity. The spectral (or bandwidth) efficiency (η_B) is defined as the achievable bit rate (R_b) divided by the bandwidth of the transmitter-receiver link:

$$\eta_B = \frac{R_b}{B} \quad [\text{bit/s/Hz}] \quad (2.3)$$

- **Atmospheric Transmission Reliability:** This is a broader term that is related to several performance indicators that depend on the modulation technique. Generally, it is meant that the MS should be able to attain a specified BER under the most adverse atmospheric conditions. Furthermore, it should be resistant to phase jitter (caused by fluctuations in signal power), pulse extensions and distortions. [20] This metric is not important for the results that this thesis needs, but represents the application favorability in real systems and communication links.
- **Implementation Difficulty:** One requirement is to use only hardware that is already available to the Aerospace Engineering faculty. Higher implementation difficulty often translates into specific hardware that may not be available. In addition, more complex MS require more time to test and implement, which may conflict with the duration of the thesis.

To make a trade-off, each criteria needs to be assigned a weight. Of the described criteria, power efficiency is seen as the most important, as it influences many other requirements in actual LCT's. For now, the chosen weight is 4-3-3-3. Evaluating each criteria has been done based on the information available in the literature. In the case that an objectively computed score is possible, a score between 1-4 is used where increments of 0.2 are possible to allow for small distinctions between MS. When this is not possible, the scoring will be done based on integer values where 4 is considered excellent, 3 good, 2 acceptable, and 1 poor.

Starting with the power efficiency, it can be evaluated by comparing the SNR [dB] of the MS at a given BER. This can be estimated using figures or precise values reported in tables, the latter of which is preferred. The higher the SNR required to achieve the specified BER, the worse a MS performs. The score is computed by normalizing the value of the best performing MS at 4. An example of a comparison between MS can be seen in Figure 2.8.

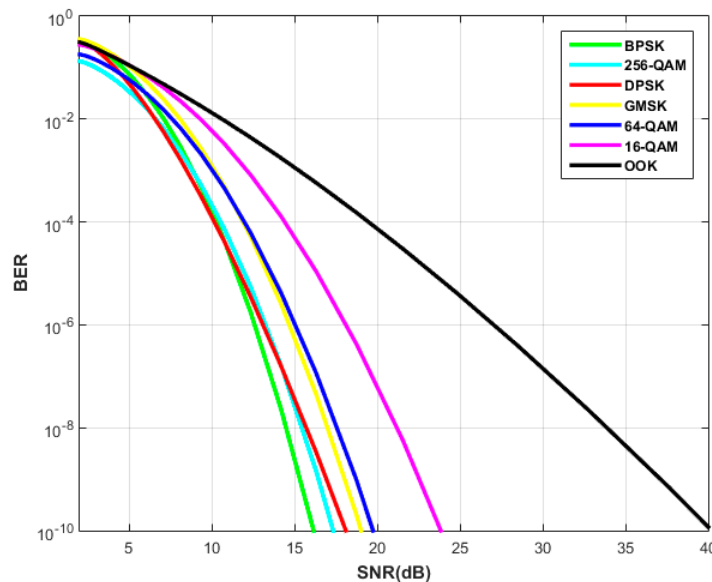


Figure 2.8: Example of the BER performance of different modulation schemes in a moderate turbulence channel. Source: [42].

The spectral efficiency is also quantifiable and given in [bits/s/Hz] often on a logarithmic scale. In this case, the data are used to rank MS with increments of 0.5, since finer distinctions are not needed. One of the comparisons in spectral efficiency can be seen in Figure 2.9.

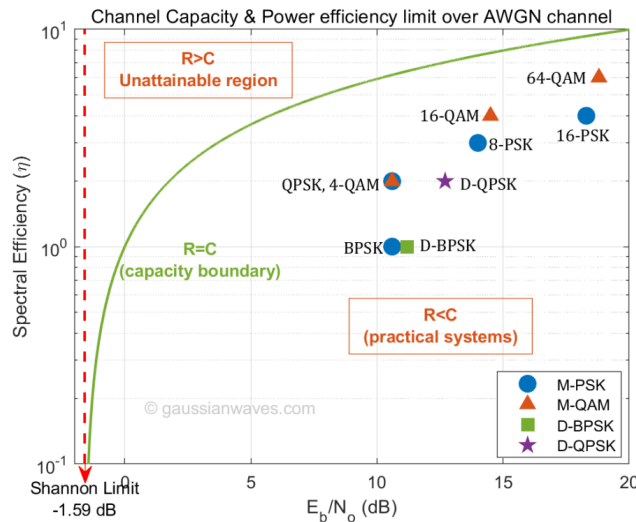


Figure 2.9: Spectral efficiency as a function of SNR (similar to E_b/N_0) for different modulation schemes at a BER of 10^{-6} . Source: [43].

To classify the transmission reliability of each MS, its performance for different weather conditions should be known. In most of the literature, the SNR is reported for each MS with turbulence levels varying from weak to moderate to strong. To quantify the transmission reliability, the ratio is calculated between the strong and weak performance. The smaller the ratio, the better the MS is resistant to adverse conditions.

Finally, the implementation difficulty must be evaluated for each MS. This is hard to quantify, and for that reason, each MS is judged individually. This judgement was based on expert opinion, the comparison of the respective receiver architecture, and MS comparison studies.

The MS that will be evaluated in the trade-off need to meet the following conditions: a majority of the criteria needs to be assessable, the MS needs to be established as practically usable in both commercial and experimental applications, and the MS needs to be included in at least 1 comparison study such that a ranking is possible. Some coherent MS like PolSK and frequency shift keying (FSK) are not considered in this trade-off, because they did not see any inclusion in comparison studies. Additionally, FSK is not implemented in optical coherent detection because it is inferior to PSK in both power and spectral efficiency. PolSK is occasionally implemented but makes the transmitter and receiver architecture too complex to be considered for this thesis.

The results of the trade-off can be seen in Table 2.1, where the results of higher order MS's have been combined into a single column that is indicated with the "+" suffix. Starting with OOK, it is the simplest, but suffers from poor power efficiency. PPM has a better power efficiency than OOK, but worse spectral efficiency. Suitable applications of PPM are for photon-starved links at low data rates (like deep space links). As the PPM-orders increase, the hardware complexity also increases greatly compared to OOK. [26]

For the coherent MS, BPSK and QPSK are the most used PSK schemes, which benefit from great power efficiency and the general benefits of coherent detection established previously. DPSK has a slightly lower power efficiency but makes up for it in complexity. While real systems need some kind of PLL mechanism like coherent detection systems, it does not need a LO and the hardware needed to operate it. Compared to IM/DD schemes such as OOK and PPM, DPSK also has better background noise rejection. DPSK is unique in the sense that it is more resistant to atmospheric effects than intensity modulation, but also less complex to implement than coherent detection schemes and at the same time capable of achieving high data rates. [26]

The higher order PSK schemes improve on spectral efficiency and transmission reliability but suffer in power efficiency and implementation difficulty. Finally, higher order QAM experiences the same effects as higher order PSK.

Table 2.1: A trade-off matrix that ranks the different modulation schemes.

Criteria	Weight	OOK	8-PPM+	BPSK	QPSK	DPSK	8-PSK	16-PSK+	16 QAM+
Power Efficiency ^(a)	4	1	1.6	4	3.8	3.4	3	2.2	3
Spectral Efficiency ^(b)	3	2	1.6	2	3	2	3	3.5	3.5
Transmission Reliability ^(c)	3	3		3	2.5	4	3	2	2
Implementation Difficulty ^(d)	3	4	2	3	2	3.5	2	1	1
Total (Weighted Score)		2.38	1.72	3.08	2.90	3.24	2.77	2.18	2.42

References

^a Figure 4.4 [44, p. 147] , Figure 8 [45, p. 6] , Table 2 [42, p. 10] , Table 3 [46, p. 13] , Figure 1 [47, p. 59] , Figure 1 and Table 2 [43] , [48, p. 26]

^b Table 2 and Figure 2 [43] , Table 1 [49, p. 7357] , Table 9 [48, p. 29] , Figure 1 [50, p. 2] , Figure 14 [26, p. 300]

^c Table 2 [42, p. 10] , Table 3 [46, p. 13]

^d [20, 25, 44, 51]

Looking at the total weighted score, DPSK and BPSK are the closest contenders. The primary trade-off between BPSK and DPSK is in their complexity. Between the two, DPSK is easier to implement. [29, p. 122]

For coherent detection of BPSK, there are several receiver architectures that differ in implementation difficulty. Homodyne detection of BPSK can be done using either an OPPL or a DSP method. Optical PLL's are currently in operational use for inter-satellite links, but for satellite-to-ground links, DSP techniques are more likely to be used in the future. [51, 52] This allows for a free-running LO, but still requires a PLL in the electrical domain. This can be aided by a dedicated lock-in amplifier, but this is still more difficult than the implementation of a DLI.

In addition, a second laser with a low linewidth is not available either, so homodyne detection would need to be performed with the same laser. This can be achieved by splitting the signal so that one part remains unmodulated, but there will still be no exact control over the frequency difference between the modulated signal and the LO reference.

Although heterodyne and intradyne detection can also use the DSP approach, they require a second laser with a controllable frequency which is not available.

For DPSK, no PLL has to be implemented for the bit detection itself, and no LO is needed. The most difficult part is ensuring the DLI is correctly aligned and stable, but this is more manageable than implementing the demodulation process for homodyne BPSK detection.

In summary, coherent homodyne detection of BPSK outperforms or equals differentially coherent DPSK detection in all areas except implementation difficulty. Given that DPSK can achieve potential similar to that of BPSK with lower implementation difficulty, DPSK's top placement in the trade-off is accepted as the most suitable MS to use for this thesis.

Revisiting Research Question 1: *"Which coherent modulation scheme is optimal for hardware implementation in a free space optical communication system for this thesis?"*, we can now answer that it is Differential Phase Shift Keying.

2.3. System Architecture and Components

Now that DPSK has been selected as the MS of choice, it needs to be implemented. To begin with, a basic receiver architecture is introduced that results in a functional communication link. This can be seen in Figure 2.10.

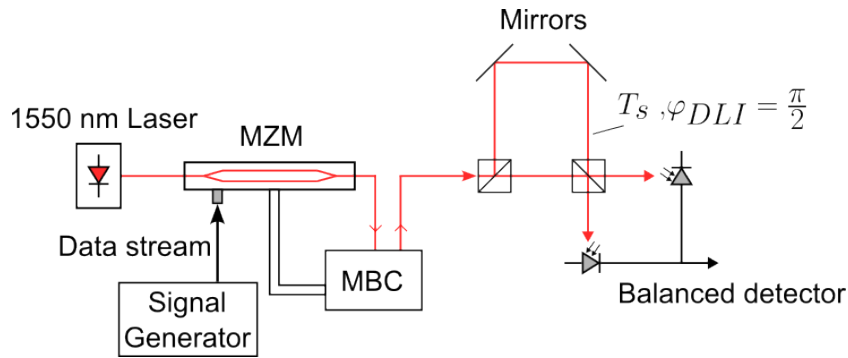


Figure 2.10: Schematic of the proposed setup for DPSK. The Mach-Zehnder Modulator (MZM) and MBC —Modulation Bias Controller ensures that BPSK modulation is performed at the transmitter side. The DLI has a delay of T_s and a phase shift of φ_{DLI} . Finally the optical signal is detected with a balanced detector.

This section will outline the primary components that are needed to construct a functioning hardware setup. For each component, the possible limitations and constraints it imposes will be discussed. For components such as the modulator and bias controller, an additional explanation is given as a foundational understanding for the verification tests in the next chapter. Finally, the design choices leading to the final setup are explained.

2.3.1. Laser source

The laser source that will be used for this thesis is the LAZ-LAB-NL-1560 from iXBlue. The most important metric for testing is the coherence length. The coherence length of a laser source is the propagation distance for which the wave maintains its phase relations. The reason this is important is because without a coherent wave at the receiver end, constructive/destructive interference does not work. The same is also true for any coherent MS.

The coherence length depends on the center wavelength and the linewidth. With an ultra-narrow linewidth of 0.1 [kHz] and a center wavelength of 1550 [nm], the coherence length is around 3000 [km].⁵ This far exceeds the required coherence length for a lab setup and imposes no constraints. The output power is tunable with a range of 10-40 [mW]. Depending on the tests that are going to be performed, reducing the output power is likely, and this can be achieved with Neutral Density Filters (NDFs).

The wavelength of 1550 [nm] is often used in FSO because of its low atmospheric absorption, which is important for real links passing through the air at significant distances. The laser is classified as "1M", which is deemed safe in all conditions under normal use. The power is deliberately kept at 10 [mW], resulting in about 1 [mW] when leaving the fiber. This means requirement **NFR2** is satisfied.

2.3.2. Intensity/Mach-Zehnder Modulator

An intensity modulator uses a Mach-Zehnder-type interferometer to control the optical output. An optical waveguide is split into two paths and recombined again. Its output is modulated by varying the delay in each path/arm. This delay is created by applying an electric field to the optical waveguide, which results in a change in the refractive index. The working principle behind this is the Pockels effect, and it applies to materials commonly used for optical waveguides such as lithium niobate (LiNbO_3). Phase modulation is converted into intensity modulation by interfering the two waves.⁶

The electric field can be created by applying voltage across the electrodes. For intensity modulators, two sets of electrodes are used; one for the modulation signal (RF), and one for setting the operation mode or bias (DC). These electrodes and the optical waveguide can be seen in Figure 2.11.

⁵For the exact calculation see appendix section A.4.

⁶Although in theory a phase modulator would suffice for producing a BPSK signal, an intensity modulator is used instead for several reasons. Firstly, it is more versatile and allows for testing of OOK as well. Second, it provides direct control over the bias of the modulator, which is not the case for the phase modulator that is available.

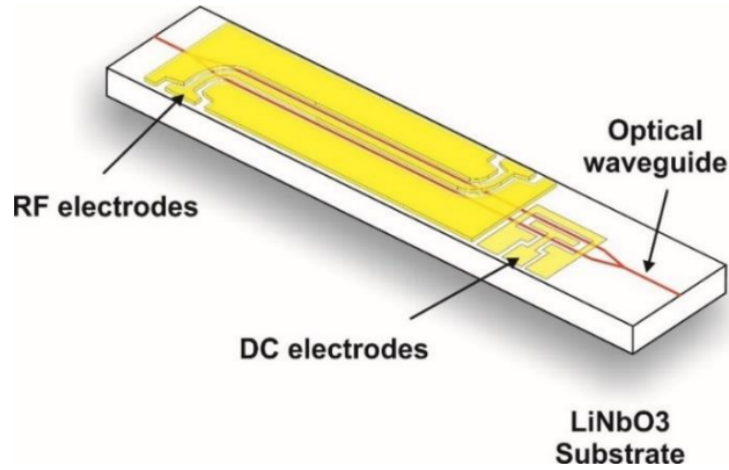


Figure 2.11: Schematic view of a lithium niobate (LiNbO_3), intensity modulator. The optical waveguide uses a Mach-Zehnder type interferometer to convert phase modulation into intensity modulation. The RF electrode is used to encode the electrical signal, and the DC electrode is for setting the desired operation mode. Source: [53].

For the electrodes seen in the schematic, a voltage is applied using a coaxial cable, where the outer electrodes share the same voltage. This creates an opposite but equal phase delay in each arm. This is referred to as a 'push-pull' configuration. For a voltage $V(t)$, the power output is given in Equation 2.4.

$$P_{out}(t) = P_{in} \cos \left(\phi_{bias}(t) + \frac{V(t)\pi}{2V_{\pi}} \right)^2 \quad (2.4)$$

where $P_{out}(t)$ is the output power, P_{in} is the input power of the unmodulated light source, ϕ_{bias} is the bias phase delay, $V(t)$ is the voltage applied at the RF electrodes and V_{π} is a characteristic of the modulator also called the half-wave voltage. (For the derivation see section A.3.) The bias phase delay (ϕ_{bias}) depends on the voltage applied at the DC electrodes, and is described by the following equation:

$$\phi_{bias}(t) = \frac{\pi V_{DC}(t)}{2V_{\pi,DC}} + \phi_0(t) \quad (2.5)$$

where ϕ_0 is the bias phase drift, V_{DC} is the voltage applied at the DC electrodes and $V_{\pi,DC}$ is the half-wave voltage for the DC electrodes.

The half-wave voltage, V_{π} , is the voltage needed to induce a π phase difference between the two paths.⁷ In other words, it represents the voltage needed to go from constructive to destructive interference (and vice versa).

In addition to the power of the output, the primary interest for DPSK is the phase of the optical field. The phase information of the optical output is represented by the electric field and is given in the equation below.

$$E_{out}(t) = E_{in} \cos \left(\phi_{bias}(t) + \frac{\pi V(t)}{2V_{\pi}} \right) \quad (2.6)$$

where E_{in} and E_{out} are the in-and-output electric fields, respectively. The field and power transfer functions have been plotted for three different operation modes and are illustrated in Figure 2.12.

⁷For a single phase-modulator, V_{π} simply represents the voltage needed to induce a π phase shift. This difference in definition is explained further in the Appendix section A.3, but is not critical to understanding this section.

Field transfer function
Power transfer function

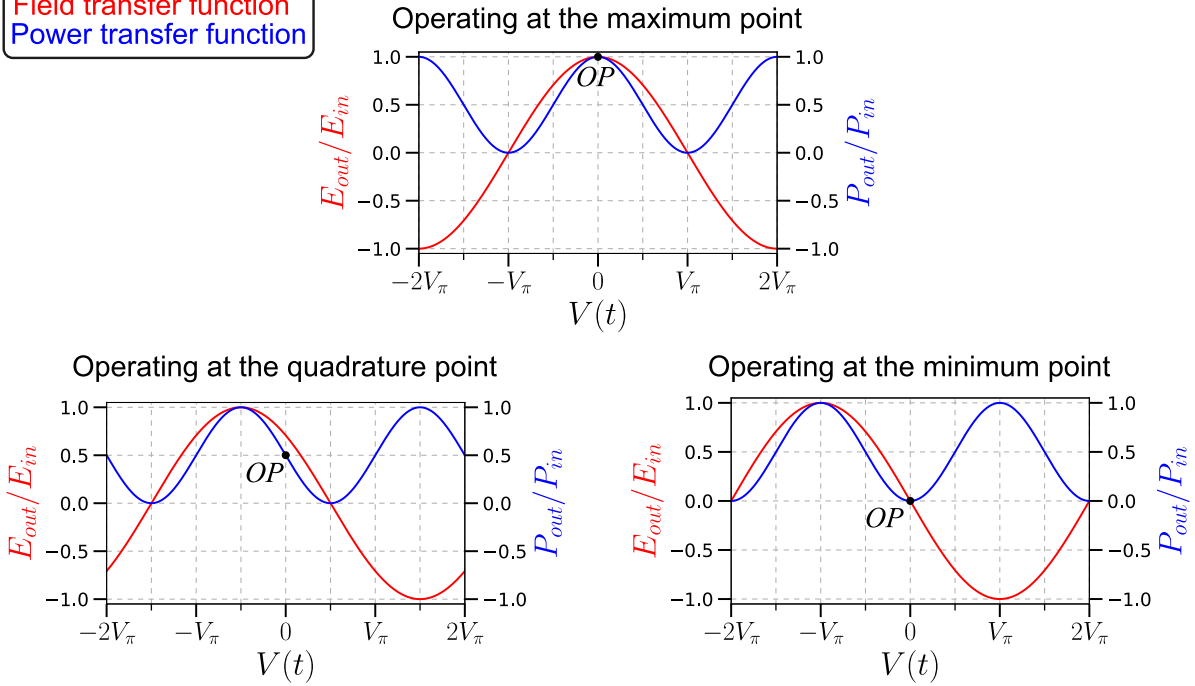


Figure 2.12: The field and power transfer function of a Mach-Zehnder intensity modulator operated at different bias points. The Operating Point (OP) (or bias), depends on the modulation format that is chosen. For OOK and B/DPSK, the quadrature and minimum operating point are used, respectively.

Each operation mode is achieved by setting the correct ϕ_{bias} . The bias phase delay for each mode is given below:

- The maximum (or full-carrier) operating mode is achieved when: $\phi_{bias} = 0 + k\pi, \quad k \in \mathbb{Z}$.
- The quadrature operating mode is achieved when: $\phi_{bias} = \pm \frac{\pi}{4} + k\pi, \quad k \in \mathbb{Z}$
- The minimum operating mode is achieved when: $\phi_{bias} = \frac{\pi}{2} + k\pi, \quad k \in \mathbb{Z}$

The operation mode is dictated by the MS or other purpose that needs to be achieved. The use of the maximum operating mode will be shown in section 3.1. The quadrature mode is used for OOK, with a $V(t)$ that has an amplitude of $V_\pi/2$, swinging between the maximum and minimum power output and thus creating an intensity-modulated signal. For DPSK (or BPSK), the minimum operating mode is used to go between a phase of 0 and π . This is illustrated more closely in Figure 2.13.

A square wave or Pseudo Random Binary Signal (PRBS) with an amplitude of V_π applied at the minimum operating point causes a swing between the two maximum points. When going through the minimum point, a dip in power occurs, which can be seen in the output signal. The phase change from 0 to π is caused by the change of the electric field compared to the input. Looking at the field transfer function for the minimum mode in Figure 2.13, it can be seen that the output field changes from 1 and -1 , which is equivalent to a π phase shift. To conclude, if the right amplitude of V_π is chosen for the electrical input signal, and the minimum point bias is maintained, phase shift keying is achieved, and DPSK demodulation can be performed at the receiver end.

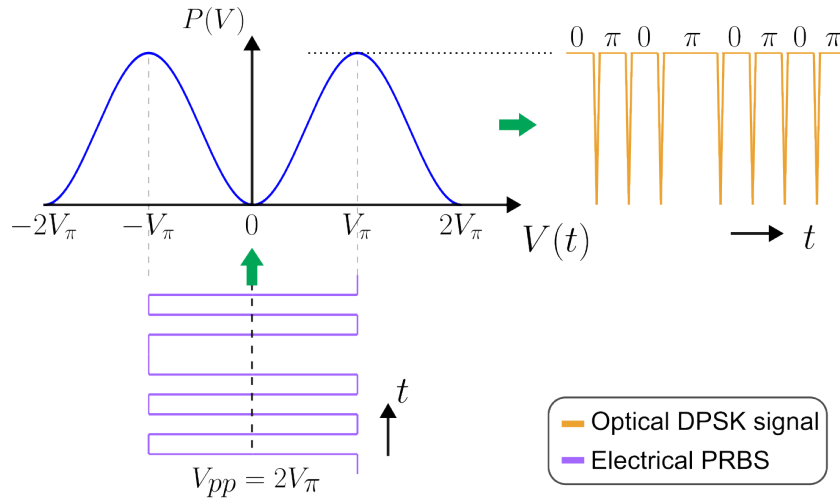


Figure 2.13: Power transfer function biased at the minimum point for the DPSK modulation format. The electrical signal is a PRBS with a peak-to-peak voltage (V_{pp}) of $2V_\pi$. The optical output power stays at the maximum mostly, with dips caused by crossing the minimum point. The phase of the optical signal alternates between 0 and π , accomplishing phase shift keying (PSK).

It is important to note that while in theory the optical power swings between the full minimum and maximum of the transfer function, this is not achieved in reality due to losses in the modulator.

The modulator used for this thesis is the MX-LN-0.1 from iXBlue, and has an electro-optic bandwidth of 400 [MHz], allowing data rates up to 400 [Mbit/s]. Higher bandwidth modulators were also available but ultimately not needed, so this bandwidth is not a constraint.

2.3.3. Modulation Bias Controller

In the previous section, the role of the DC bias electrodes was discussed. Depending on the voltage applied, the bias point and subsequently the operation mode change. The modulation bias controller (MBC) takes care of finding the correct DC voltage to apply to the electrodes. In addition to setting the operating point, the MBC also compensates for phase drift in the modulator (ϕ_0). This phase drift is caused by changes in temperature, non-uniformity of heat distribution, material aging, effects due to photorefraction, and the build-up of static electrical charges. [53] The modulator also has a static phase delay that is caused by small differences between the two optical paths, but this term can be lumped together with the drift to make up ϕ_0 .

The MBC accomplishes this control by applying a low-amplitude and low-frequency dither signal to the DC bias electrodes. This causes the optical output to contain harmonics at the frequencies of the dither signal. This output is detected with a monitoring photodiode. Using DSP based on a Fast Fourier Transform analysis, the desired DC bias voltage can be determined, and a lock on the operating point can be established. [54] This concept is further explored in section 3.1 and section A.5.

A schematic showing how the MBC is connected to the modulator can be seen in Figure 2.14. In the figure, the fiber coupler and the monitoring photodiode are illustrated as external to the MBC, but in reality, the MBC model that is used incorporates these components internally, eliminating the need for an extra coupler or photodiode. The MBC model used is the MBC-DG-LAB-A1 from iXBlue. It's nominal dither frequency is 1 [kHz] and has a locking accuracy of $\pm 0.5^\circ$ at the quadrature point. The dither amplitude is variable but is in the range of 20-50 [mV] mostly and should not interfere much with high-frequency modulation.

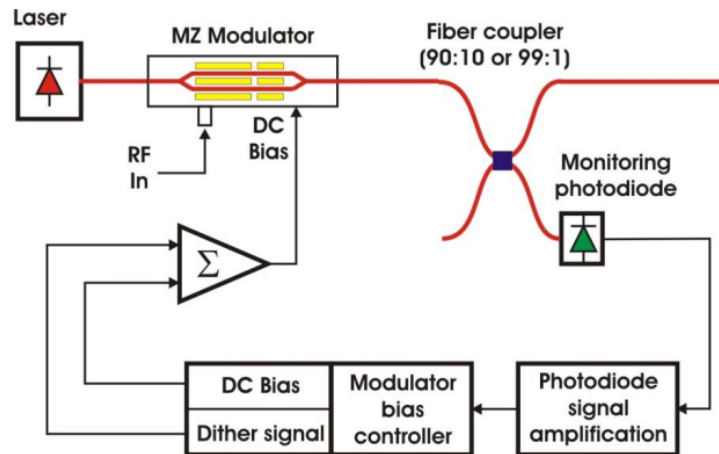


Figure 2.14: Basic schematic of a Mach-Zehnder Modulator and the Modulation Bias Controller (MBC). Source: [55].

2.3.4. Signal Generator

The signal (or function) generator needs to provide an electrical signal to the modulator's RF input port. The main constraint that must be considered in the selection of a signal generator is its bandwidth. For DPSK, the length of the delay line dictates what data rate needs to be chosen. The higher the data rate, the shorter the delay line, which is preferable. The upper limit of this data rate is constrained by the sample rate of the oscilloscope and the bandwidth of the photodetector. For the purpose of testing the requirement, a data rate of at least 100 [Mbit/s] must be attained.

Another constraint is the use of available equipment. Specialized hardware that can generate PRBS at high data rates are hard to come by, and were unavailable at the time this thesis was conducted. Therefore, the only available signal generator that satisfied the data rate requirement was chosen. The TTI TG5011, has a bandwidth up to 50 [MHz], but cannot generate a PRBS, only a square wave.

However, it is important to note that a signal generator does not generate the same square wave for all frequencies. In Figure 2.15, the square wave can be seen for a number of frequencies. The main metric by which to evaluate the 'squareness' of a PRBS or square wave, is by looking at the rise/fall time of the signal. In Figure 2.16, the rise and fall time of the square wave has been measured for several frequencies. A clear increase of the rise/fall time with respect to the total period can be seen as the frequency increases. So a higher data rate comes at the cost of a longer rise/fall time (in relation to the period). It is important to note that the total rise/fall time is 4 times the individual rise/fall time. So, any ratio above 25% no longer represents a real square wave but becomes sinusoidal.

For a square wave, it is also important that the low and high pulses are of somewhat equal duration. The duty cycle of the high pulse was measured across a range of frequencies and is displayed in Figure 2.17. No clear trend is visible, but there is a distinct outlier at 25 [MHz] with a 43% duty cycle. These two factors should be taken into account when selecting the frequency/data rate of the square wave.

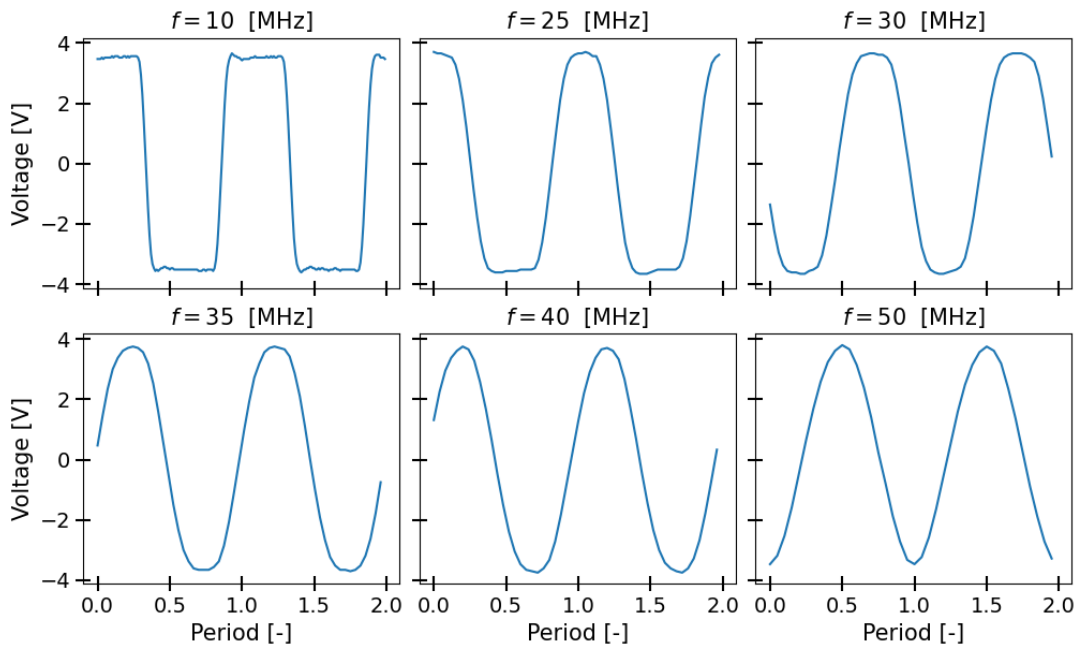


Figure 2.15: The square wave generated by the TTI TG5011 signal generator for a number of frequencies at an amplitude of 3.56 [V]. This amplitude is equal to the V_{π} that is used for the final tests. As the frequency increases, the square-wave becomes less square and more sinusoidal.

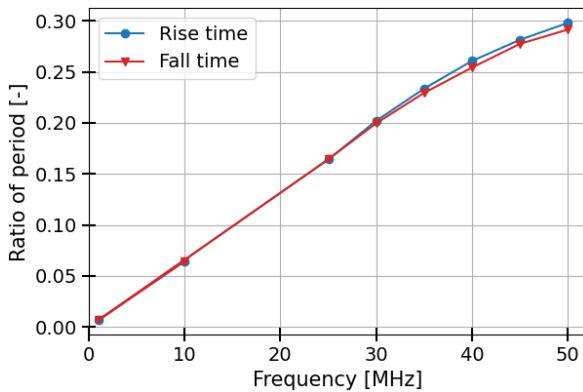


Figure 2.16: Rise and fall times (90/10) of a square wave, expressed as a ratio of the period. Frequencies ranging from 1 to 50 [MHz] were tested. As the frequency increases, the rise/fall time compared to the total period becomes larger.

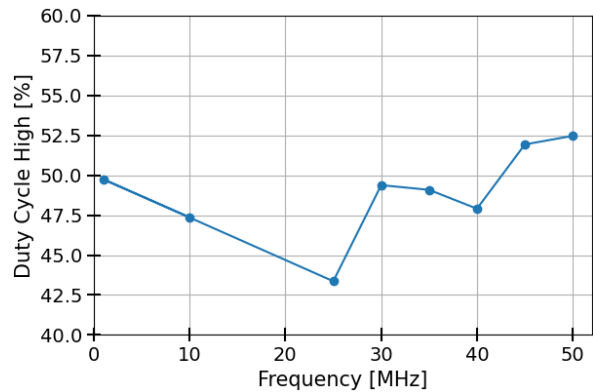


Figure 2.17: Duty cycle (high) of a square wave created by the signal generator. Frequencies ranging from 1 to 50 [MHz] were tested. Ideally, the duty cycle is 50%, but for this signal generator, it varies for the selected frequency.

2.3.5. Detectors

For the photodetectors that will be used, the most important variable is the bandwidth. A bandwidth that is too low restricts the maximum data rate and, therefore, the length of the delay line. As discussed earlier, the benefits of DPSK with respect to OOK can only be unlocked with a balanced detector as opposed to a single photodetector. However, for reference purposes, a single detector will *also* be used.

Another important constraint that a photodetector imposes is the size of the photodiode. Depending on the divergence of the beams, a smaller photodiode may make the setup easier to align for interference but more difficult to focus, and depends on the optical setup that is used. For both the single and balanced photodetector, the most important specifications have been listed in Table 2.2.

Table 2.2: Specifications of the single and balanced detector that were selected for this thesis.

	Single (PDA015C)	Balanced (PDB230C)
Bandwidth (-3 dB)	400 [MHz]	100 [MHz]
Responsivity @ 1550 nm	1.03 [A/W]	1.02 [A/W]
Active area diameter	150 [μm]	300 [μm]
Transimpedance gain (High-Z)	$5 \cdot 10^4$ [V/A]	$5 \cdot 10^4$ [V/A]
Common Mode Rejection Ratio	-	> 30 [dB]
NEP	20 [pW/ $\sqrt{\text{Hz}}$]	7.5 [pW/ $\sqrt{\text{Hz}}$]
Overall output voltage noise	9 [V_{rms}]	< 6.5 [V_{rms}]
Output dark/DC offset	20 [mV]	< ± 10 [mV]

2.3.6. Oscilloscope

An oscilloscope is used to store and analyze the photodetector output. For this thesis, the available oscilloscope was the PicoScope 3406D. The most important constraint it imposes is a bandwidth of 200 [MHz] and a maximum sampling rate of 1 [GS/s]. The sampling rate does not place a strict limit on the data rate since it needs to be a minimum of two times the bandwidth. Instead, the bandwidth limits the data rate to 400 [Mbit/s]. However, this is only possible if sampling is performed in the right instance, which requires a timing recovery loop. Because this is not used, the number of samples available per bit determines how close one can get to the maximum intensity of the bit. Therefore, a trade-off needs to be made between the data rate and the number of samples per bit.

2.4. Design Choices

Given that the limitations and constraints of the main components of the system have been discussed, the specific details of the final setup can be decided. The majority of decisions have been made in an iterative manner throughout the thesis, but the motivation behind them will be discussed here in no particular order. Firstly, the data rate that is chosen will be motivated. Secondly, a number of choices regarding the optics used in the setup will be discussed.

2.4.1. Data Rate

One of the main constraints imposed by the signal generator is that it cannot generate a PRBS, only a square wave. Unlike a PRBS, a square wave only alternates between 1 and 0. Supposing that a square wave period represents 2 bits, when delayed by 1 bit duration, the interference of the two signals is only destructive. This would mean an endless sequence of 0s, which does not allow one to detect the other signal level for constructive interference. Therefore, no SNR can be determined. Thus, for performance evaluation, the data must at least alternate between 0 and 1. This can be done by imagining that there are 4 bits per period of the square wave, and delaying it by 1 bit. This can be seen in Figure 2.18.

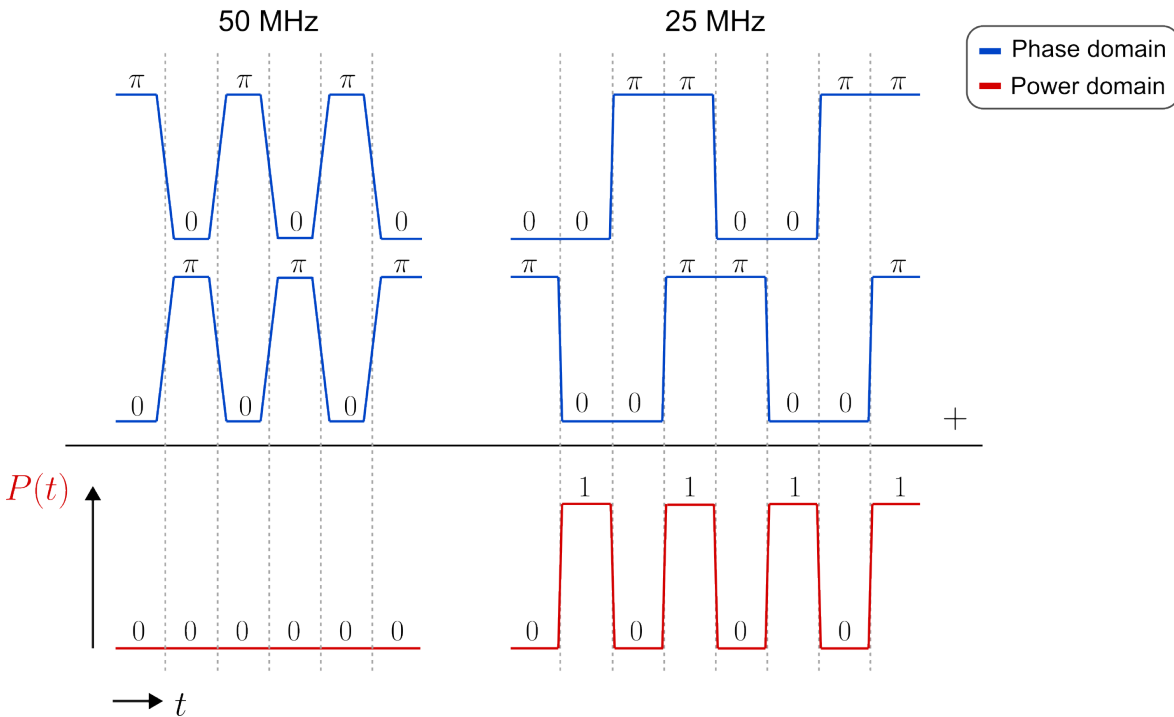


Figure 2.18: Diagram showing how the encoded phase from a square wave translates into the power detected when DPSK demodulation is performed. The left shows a square wave with 2 bits per period, whereas the right shows a square wave with 4 bits per period. For alternating bits at the detector, 4 bits per period are required.

So, even though the 50 [MHz] signal meets the minimum data rate requirement, it is not sufficient to test the performance. Unfortunately, performing the 4 bits per period trick on the 50 [MHz] signal is not possible, since it has a very high rise/fall time. In particular, all square waves above 35 [MHz] are too sinusoidal to be split into 4 separate bits.⁸ Interfering these signals would only leave a very small window of time for which total constructive/destructive interference can occur. So, the longer rise/fall time at high frequencies limits the suitable frequency range to 25-30 [MHz].

A major disadvantage to lower data rates is that the DLI needs to be longer. The length of the DLI is inversely proportional to the data rate R_b , as seen in the equation below:

$$L_{DLI} = \frac{c}{R_b} \tag{2.7}$$

A longer delay line increases the likelihood for instability, which degrades the SNR. Ultimately, choosing between 25 and 30 [MHz] is a trade-off between a shorter delay line and a longer rise/fall time. A longer rise/fall time leads to fewer samples per bit, and without timing recovery or a DSP approach for bit determination, a shorter rise/fall time is preferred. The difference in delay line length (50 [cm] total) was not substantial enough to consider a longer rise/fall time. Therefore, a frequency of 25 [MHz] was chosen. With 4 bits per period, this gives a data rate of 100 [Mbit/s], which requires a delay line length of 1.5 [m] (or 3.0 [m] round-trip).

In retrospect, too much emphasis was put on the rise/fall time, without taking into account the duty cycle. As seen in Figure 2.17, at 25 [MHz], the duty cycle is highly unequal (43%). A better choice would have been to test frequencies between 25 and 30 Mhz that had a better duty cycle. The small increase in rise/fall time would be insignificant compared to the improvement in duty cycle.

Given that the sampling rate is high enough for 25 [MHz] (10 samples per bit), the unequal duty cycle should not affect the bit determination greatly.

⁸See Figure 2.15.

2.4.2. Optical setup design

To implement and test a functional coherent detector, it follows that the final optical signal needs to be received on a photodiode. The biggest constraint in designing an optical setup that achieves this is the total path length. As the path length increases, the divergence of the beam becomes more significant, and any small angular offsets make alignment more difficult. To create the long delay line (1.5 [m]) there are two main options:

1. On an optical breadboard, a series of mirrors is used in such a way that a total distance of 3 [m] is achieved.
2. Using a prism placed at a distance of 1.5 [m] from the beam splitters.

The primary advantage of the first option is that it could be situated on a single breadboard, resulting in a more stable delay line. However, the number of single mirrors needed and the size of the optical breadboard make aligning it much harder. The second option (prism) will not fit on a single breadboard, making the delay line less stable.

A major advantage of the prism is that the two faces are guaranteed to be perpendicular ($\pm 0.05^\circ$), eliminating two degrees of freedom that are not needed. Essentially, it guarantees that the incoming and outgoing beams are parallel to each other even if there is a rotational offset. This can be seen in Figure 2.19(a). This reduces the degrees of freedom to two: lateral displacement and vertical rotation. This can be seen in Figure 2.19(b,c).

For the first option, each mirror has 4 degrees of freedom each: 2 for displacement and 2 for rotation. On a small breadboard, the number of mirrors required to create a long delay line would be at least 4. The total number of degrees of freedom this adds makes alignment much more difficult and is not strictly necessary for creating a functional receiver. Therefore, the simpler optical setup using the prism was chosen.

To use this delay line, a collimated beam is required. For a Gaussian beam exiting a fiber, perfect collimation is not achievable, and there will always be some divergence. The main objective that collimating aims to accomplish is minimizing this divergence. Specifically for this delay line, a small divergence is preferred, since the reference (fixed) and delayed beams will be interfering.

Without any additional optics, the light exiting the fiber has a divergence far too large for interference to occur at the beam splitter, in addition to most of the power being lost. Therefore, some optics are needed to correct for this. To choose the right optics for collimation, two main factors should be considered:

- Preferably, the beam divergence is as small as possible. This can be achieved with a larger beam diameter.
- The beamsplitter has a circular opening with a diameter of 12.5 [mm]. When the beam diameter is larger than the opening, clipping occurs, resulting in diffraction effects. These effects introduce fringes, making alignment more difficult.

One of the more straightforward options for collimation is to place a lens at the focal distance from the fiber exit. The larger the focal distance, the larger the diameter of the beam, which results in a smaller beam divergence. The issue with a larger beam diameter is that it causes clipping at the aperture of the beam splitter. This can be seen in Figure 2.19(d). A solution to this issue would be to use beamsplitters with a larger aperture. However, the prism's dimensions constrain the beamsplitters size, allowing only smaller ones to be suitable.

Another option is the use of a triplet collimator, which is mounted directly after the fiber mount. It can be seen in Figure 2.19(e). The main benefit of the triplet collimator is that it requires less alignment and results in a beam diameter smaller than the beamsplitter aperture. The largest beam diameter observed was for the delayed beam, measuring 1.9 [mm], which is much smaller than the 12.5 [mm] aperture. The big drawback is that there is a significant beam divergence for the 3 [m] distance. Although this is not ideal for interfering the fixed and delayed beams, it is functional. (The effect of this divergence is further explored in section 3.2.)

Finally, once the collimated beam reaches the photodetector, focusing is typically performed. Because

the beam diameter is much larger than that of the photodiode, when it is not focused, most of the power is lost. In a real setup, this should be done to minimize power loss. However, given that the objective is not to get the best possible performance, adding a focus lens complicates things by creating another element to align. In addition, the photodetector has a saturation power and a damage threshold. For testing purposes, a larger power is not needed.

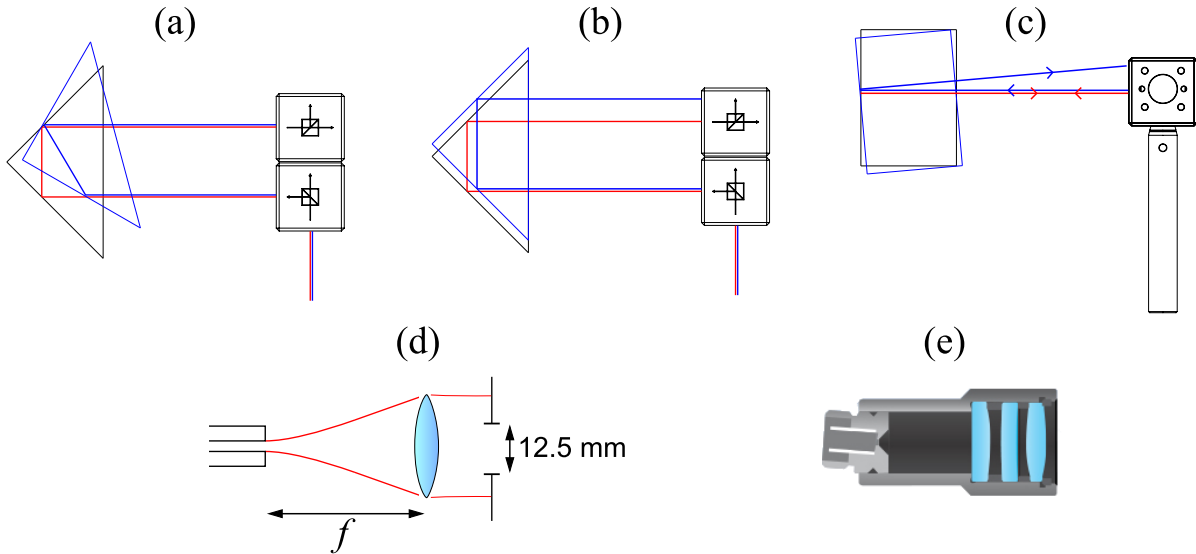


Figure 2.19: Optical setup illustrations (a) Top view of a delay line using a prism. When the prism is rotated, the in-and-out coming beams remain parallel. (b) Top view of a delay line with a prism that has an offset. The offset causes the returning beam to miss the entrance of the beamsplitter. (c) Side view of the prism. A rotation in this plane causes the returning beam to be misaligned. (d) Manual collimation setup using a single lens. The aperture stop behind the lens represents the opening of the beamsplitter. (e) Cross-section of a triplet collimator. Source(e): [56]

We can now provide an answer to Research Question 2; *"How can a coherent free space optical detection system be designed and implemented in a laboratory environment using bulk optics?"*, which is:

- With the system architecture laid out in Figure 2.10.
- Using the components specified in section 2.3 and Table 2.3.
- With the DLI having a length of 1.5 [m] compatible with a data rate of 100 [Mbit/s].
- With the optical setup described in subsection 2.4.2. Main choices are the use of a prism for the DLI and a triplet collimator for the collimation of the beams.

Table 2.3: Summary of the most important components used for the final setup.

Component	Part Name
Laser Source	LAZ-LAB-NL-1560
Intensity Modulator	MX-LN-0.1-PD-P-P-FA-FA
Modulation Bias Controller	MBC-DG-LAB-A1
Signal Generator	TTi TG5011
Single Photodetector	PDA015C
Balanced Photodetector	PDB230C
Triplet Collimator	TC12FC-1550
Oscilloscope	PicoScope 3406D
Infrared Camera	Cheetah

3

System Implementation and Verification

After selecting the system components, completing the optical design, and choosing the data rate, the setup can be implemented on an optical breadboard. Before performing tests immediately to obtain the final results, it should be ensured that critical system components are working as expected and performing the desired function. This chapter will cover a number of verification tests to ensure that implementation is performed correctly.

In the first section, the half-wave voltage of the modulator is determined, such that the output signal correctly alternates between 0° and 180° . In section two, the alignment of optical elements of the setup is verified, such that optimal interference conditions occur for detection on the photodiode. In the third section, the performance of the MBC is verified, which is needed to continuously output the correct signal. In section four it is verified that actual DPSK demodulation is performed. Finally, in section 5, the final implemented hardware setup is presented as well as the test plan.

3.1. Half-wave voltage determination

Operating the modulator correctly, requires two conditions:

1. The bias point is set appropriately to the modulation scheme
2. The appropriate amplitude of the RF input signal. For OOK and BPSK this is $V_\pi/2$ and V_π , respectively.

As seen in subsection 2.3.2, the bias point depends on the half-wave voltage of the DC port of the modulator. Since the bias controller finds the correct bias point regardless of the specific $V_{\pi,DC}$, it does not need to be determined or verified. This is not applicable to the RF port as the amplitude of the signal must be set manually. For this reason, the manufacturer provides the measured half-wave voltage in the test report. The V_π for the RF port is reportedly 3.2 [V] at a frequency of 50 [kHz] when using a pure sine-wave input.

However, this value cannot be taken for granted. First, the half-wave voltage of a modulator is known to be frequency-dependent. Second, the half-wave voltage is specific to the signal generator that is used. This is because a signal generator is not guaranteed to produce the exact same amplitude at different frequencies.

To illustrate the importance of using the correct V_π , suppose the following example; a value of V_π of 3.2 [V] is used, when in reality it is 3.8 [V]. For OOK, this would mean that you reach 98% of the maximum attainable power. For DPSK, this mistake in V_π causes the wrong phase change and causes suboptimal interference. With this particular example, around 12% of the total power is lost. (See Appendix section A.2 for the calculation.) Although this power loss is not catastrophic, it can easily be avoided by using the correct half-wave voltage. Furthermore, this example assumes an ideal scenario

in which the power of each interfering beam is exactly equal.¹ If one wave has more power than the other, the effect of an incorrect V_π amplifies the power loss.

Given that the V_π at 25 [MHz] is unknown, the best course of action is to determine it.

3.1.1. Low frequency RF half-wave voltage determination

Determining the half-wave voltage is done by finding the voltage difference between the maximum and minimum power. The maximum and minimum power can be inferred by the power transfer function. Reproducing the transfer function can be achieved by relating the voltage of your input signal to the power output of the modulator at every sample. The transfer function is finalized by plotting the input signal on the x-axis and the output power on the y-axis. The hardware setup needed for this can be seen in Figure 3.1.

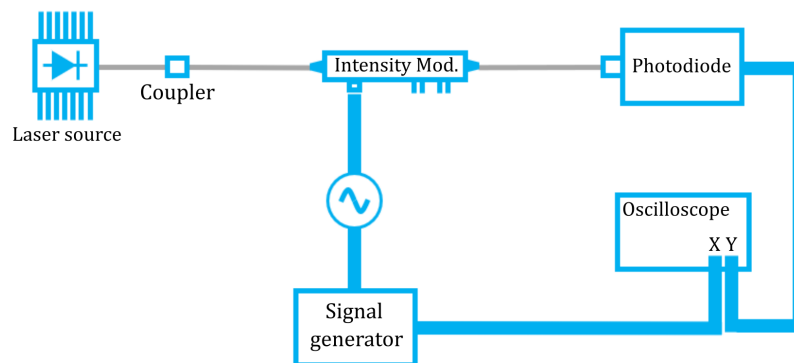


Figure 3.1: Diagram showing the hardware setup needed to produce the transfer function of an intensity modulator, such that the half-wave voltage V_π can be determined. Adapted from [57, p. 21].

One issue with this setup is that it requires the signal generator to produce two signals. Unfortunately, the available signal generator has only a single output. This issue can be circumvented by splitting the signal to go to both the signal generator and the oscilloscope.

For the test itself, an amplitude must be chosen for the input sine wave. The amplitude of the signal should be high enough such that the maximum and minimum of the transfer function can be easily identified. For a presumed V_π of 3.2 [V] this would mean a peak-to-peak voltage (V_{pp}) greater than 3.2 [V]. In this case a V_{pp} of 6 [V] was chosen, at a frequency of 50 [kHz]. Furthermore, it is important to note that this test is done with a sine wave instead of a PRBS or square wave, since these contain higher-order harmonics that distort the results. The transfer function can be seen in Figure 3.2.

¹As we will see in subsequent sections, this is not the case.

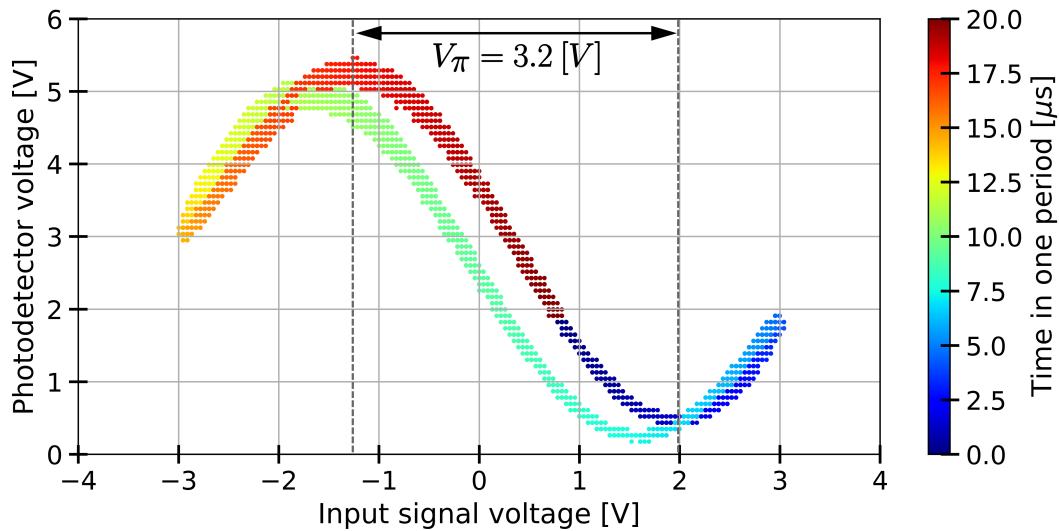


Figure 3.2: The transfer function of the tested intensity modulator using an input signal of $V_{pp} = 6$ [V] at a frequency of 50 [kHz]. The color map shows the time in one period. The half-wave voltage V_{π} is the voltage between the minimum and maximum output, which is marked with dashed lines.

Although a single-valued sinusoidal function is expected, the transfer function shows two outputs for the same input voltage. These 'shifted' paths are caused by a delay between the input signal and photodetector output signal. For this particular input signal, the delay is around 0.07 [rad], or 4° . This is equivalent to around 223 [ns]. At higher frequencies this delay changes the shape of the transfer function to such a degree it no longer is sinusoidal, and the half-wave voltage cannot be determined.

This delay can be corrected in post-processing, but the extent depends on the sample rate and frequency of the input signal. The available oscilloscope has a sampling rate of 500 MS/s for each channel, giving a resolution of 0.314 rad (18°). How close one can get to the actual transfer function will depend entirely on the phase relative to the scope timing, which is random. Therefore this method cannot be used reliably for higher frequencies given the available equipment.

There are simpler methods that could be used for higher frequencies, but these require the estimation to be done visually and have a significant margin of error (± 0.5 [V]).²

3.1.2. Higher frequency RF half-wave voltage determination

A more accurate method has been proposed in a patent from 2001 ([58]), which requires only basic equipment and also works at higher frequencies. The basic method is using a sine wave as input, and measuring the average output power. Then by comparing it to the unmodulated maximum power, the half-wave voltage can be calculated. The process can be summarized as follows:

1. Bias the modulator at the maximum power.
2. Measure the average power without input signal (off).
3. Input an RF signal of known amplitude and frequency.
4. Measure the average power with input signal (on) .
5. Use the ratio of the average powers to calculate V_{π} .

The power transfer function and the input signal that illustrate this process can be seen in Figure 3.3.

²One simple method is to perform OOK modulation with a square wave and vary the amplitude of the input signal until a maximum signal difference is reached. As noted before this method's accuracy depends on how good the eyeballing is, and the higher harmonics of a square wave undermines its validity.

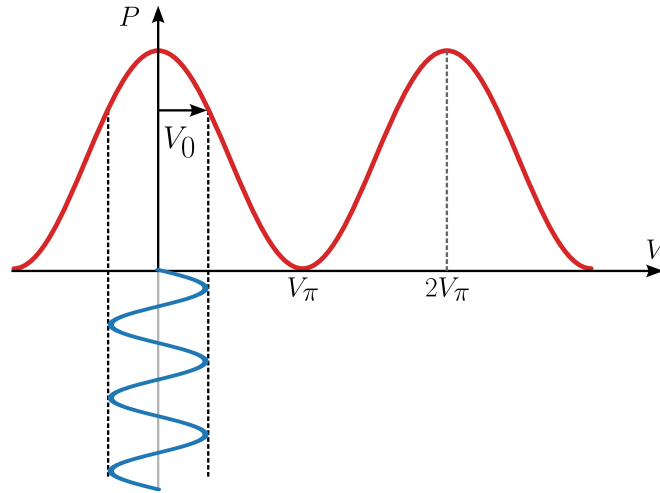


Figure 3.3: Diagram showing the power transfer function of the intensity modulator when biased at the maximum point. The input signal is a sine wave with amplitude V_0 . The power output is used to determine the half-wave voltage of the intensity modulator.

The only complexity of this method is to verify that the modulator is truly biased at the maximum point when the input signal is turned on. Even with a modulation bias controller, this should be verified, as it is essential for this method to work. The simplest way to verify this is by observing the spectrum of the photodetector voltage. When biased at the maximum point, the odd harmonics should disappear. The reasoning and derivation showing why this is the case can be seen in the Appendix section A.5.

Observing both the spectrum and average power simultaneously can be done using a beam splitter. The setup used can be seen in Figure 3.4. This setup can be simplified further if the oscilloscope can calculate the average output power and view the spectrum simultaneously, making the power sensor and beam splitter redundant.

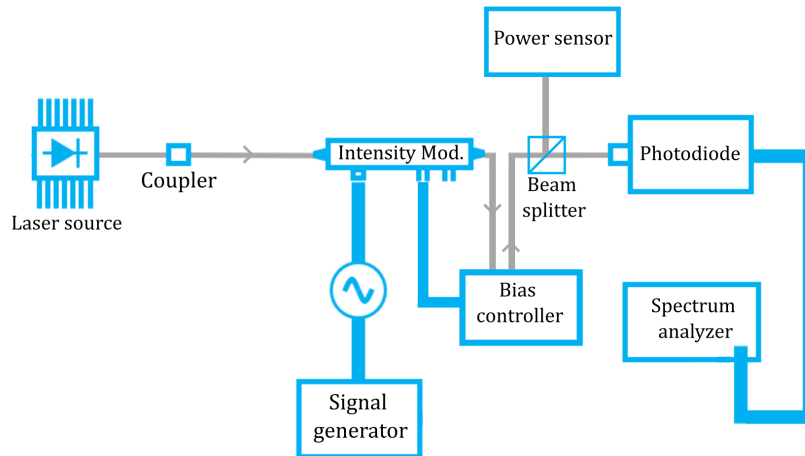


Figure 3.4: Diagram showing the hardware setup needed to determine the half-wave voltage of an intensity modulator, using the method described in [58]. (Adapted from [57])

With the power measured for the input signal on and off, the half-wave voltage can be determined by finding the value of V_π that satisfies the following equation:

$$\frac{P_{avg}(\text{On})}{P_{avg}(\text{Off})} = \frac{1}{T} \int_0^T \left[\cos \left(\frac{\pi}{2V_\pi} V_0 \cos(2\pi ft) \right) \right]^2 dt \quad (3.1)$$

The left side of the equation is determined using the measurements, whereas the integral is evaluated numerically. The results across a range of frequencies are presented in Figure 3.5.

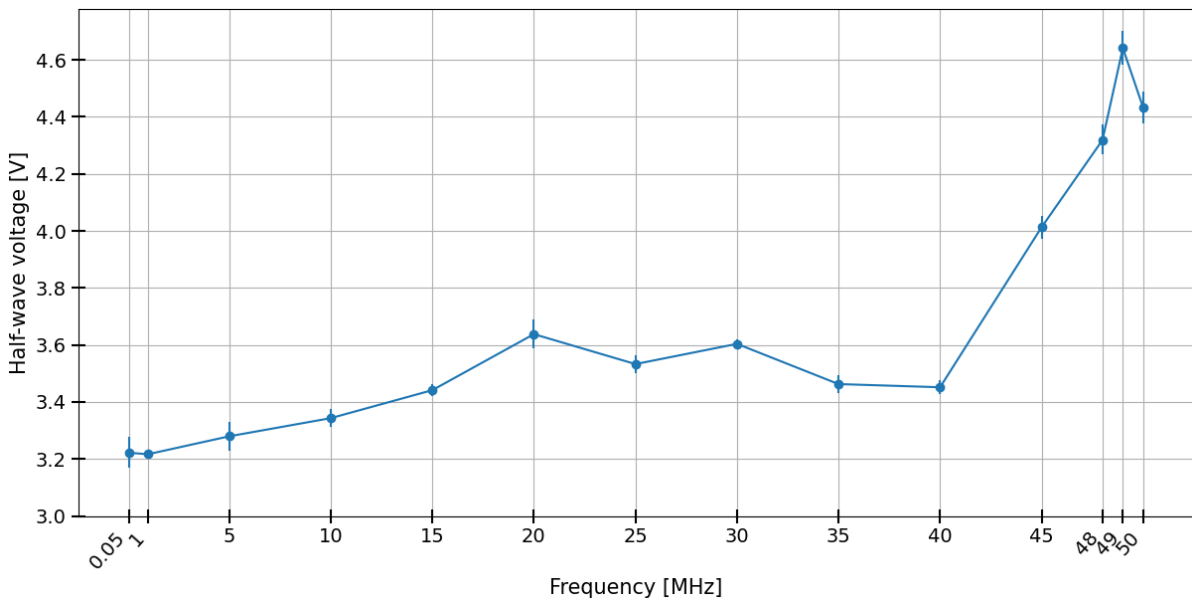


Figure 3.5: Half-wave voltage for the MX-LN-01 intensity modulator across different frequencies. Error bars indicate a one standard deviation difference in the power ratio. For the final tests performed at a frequency of 25 [MHz], $V_{\pi} = 3.53$ [V].

From the V_{π} values seen in the figure, a general increase can be seen as the frequency increases. Toward the limit of the signal generator (50 [MHz]), the V_{π} increases drastically. This can largely be explained because the signal generator's output amplitude decreases with an increase in frequency. So when an amplitude of $V_0 = 1.0$ [V] is selected, in reality the output amplitude is lower (0.96[V]).

3.2. Optical Alignment

Before tests can be performed, it must be ensured that the photodiode and beams are aligned correctly. The key requirement for DPSK to work is the following:

- The photodiode must be placed inside a fringe. This necessitates that the fringe width be larger than the size of the photodiode.

If both requirements are not met, the photodiode will be averaging the power across the fringes. This would be equivalent to averaging the power levels of a '1' bit and a '0' bit, thus completely eliminating any possibility of accurately identifying the bit. Therefore, satisfying this requirement is essential and thus requires proper alignment.

Because the laser is invisible to the human eye, a dedicated Infrared (IR) camera is used to align the fixed and delayed beams. Although a visible laser can be used for rough alignment, it is not sufficient because collimation and propagation of Gaussian beams is wavelength dependent.

For the alignment of the fixed beam and the delayed beam, ideally their axes of propagation are coincident. When this is the case, the spot that is seen will depend on the phase difference between the two beams. For a number of phase differences, the intensity across the center of the spot is plotted in Figure 3.6. When the beams have the same phase, the resulting spot is perfectly Gaussian. However, when the phase difference increases, the spot becomes lower in intensity and wider. For destructive interference (180° phase difference), the center of the spot almost reduces to 0, but not fully.

It is important to note that these intensity cross sections are simulated using the real beam divergences of the delayed and fixed beam. Depending on the exact parameters of the Gaussian beams, these plots will change slightly. For example, if both beams had the same divergence, the intensity in the center of the spot for a phase difference of 180° would be 0. However, even with slight changes, the overall takeaway remains the same. For the exact parameters of the beams and the equations used to generate these (and more) images, see the Appendix Section B.

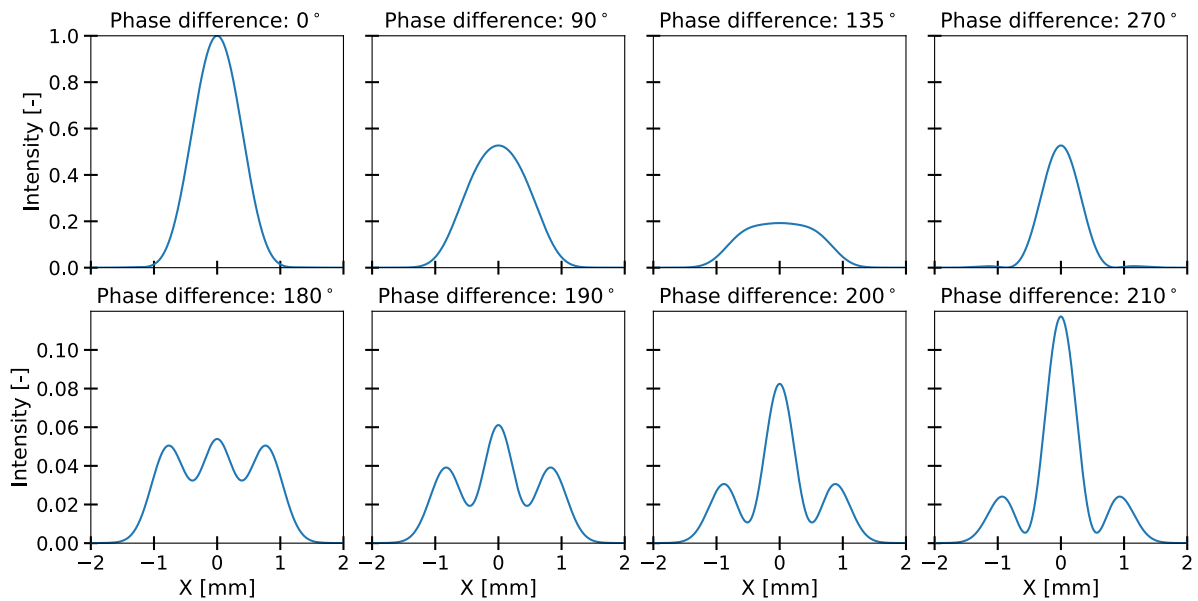


Figure 3.6: Intensity across the center of the spot for two Gaussian beams with coincident propagation axes, shown for several phase differences between the beams.

However, the ideal case is not achieved by default. Aligning the beams so that the spots arrive at the same point is not enough; their axes of propagation also need to be coincident. In Figure 3.6, a schematic of misaligned beams can be seen.

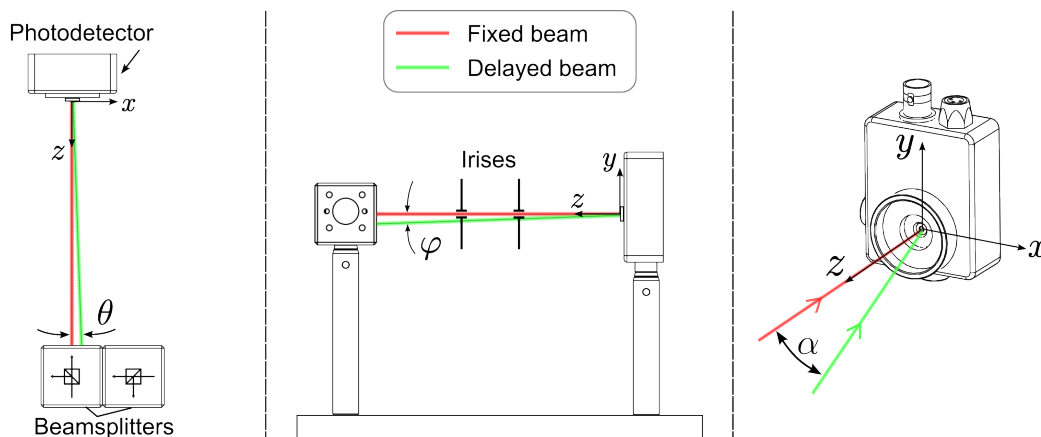


Figure 3.7: Diagram showing misalignment between the fixed and delayed beam. The view on the left is seen from the top, containing only a rotation of θ around the y axis. The middle view is seen from the side, containing only a rotation of φ around the x axis. Two irises are used to verify that the axes of the beams are coincident. The view on the right shows a perspective view of the photodetector, where the beams have an angle of α between them.

Although the beams arrive at the same point on the photodetector, their axes are offset by an angle. The angle α between the two beams determines the width of the fringe. The larger it is, the smaller the fringe width becomes. This is illustrated in Figure 3.8, which shows the progression from misalignment to ideal alignment. When both θ and φ are greater than 0, the orientation of the fringes rotates in the XY plane. Correcting for the angle θ results in only a tilt in the Y axis, producing horizontal fringes. In addition, the fringe width also increases.

Correcting for these angles is done by using the degrees of freedom in the prism and the first beamsplitter³, while viewing the image with an infrared camera. Two irises serve as the main reference to confirm

³Both the prism and first beamsplitter were placed on a kinematic platform mount, allowing for tip and tilt correction.

the coincidence of the beam axes, which are connected by a cage system to ensure their centers align. When this correction is performed, a Gaussian spot is created, which has the widest possible fringe width and is therefore ideal.

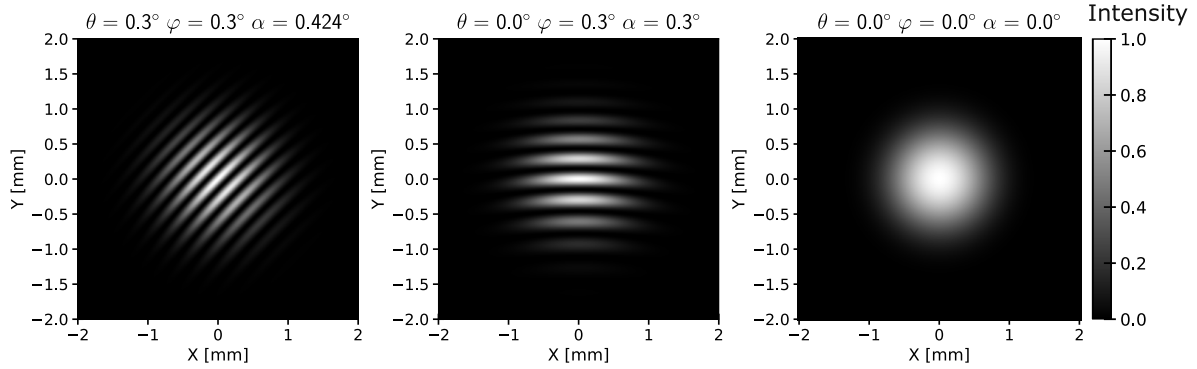


Figure 3.8: Simulated image of the spots seen at the center of the photodiode, for a number of angular differences between two Gaussian beams. For all three cases, both Gaussian beams have the same phase. For the left image, both a horizontal and vertical angle are present. In the center image, only the vertical angle φ remains. When both are removed, the Gaussian spot in the right image is produced.

The results of this alignment process can be seen in Figure 3.9. For the first image that contains both X-and-Y tilt, the fringe width is approximately $140 \text{ } [\mu\text{m}]$, which does not satisfy the requirement, since the photodiode has a diameter of $150 \text{ } [\mu\text{m}]$. The second image has a fringe width of $265 \text{ } [\mu\text{m}]$, which does satisfy the requirement, but is not ideal. Correcting both angles produces the expected spots. The destructive spot is not fully dark in the center because the fixed and delayed beams have different divergences.

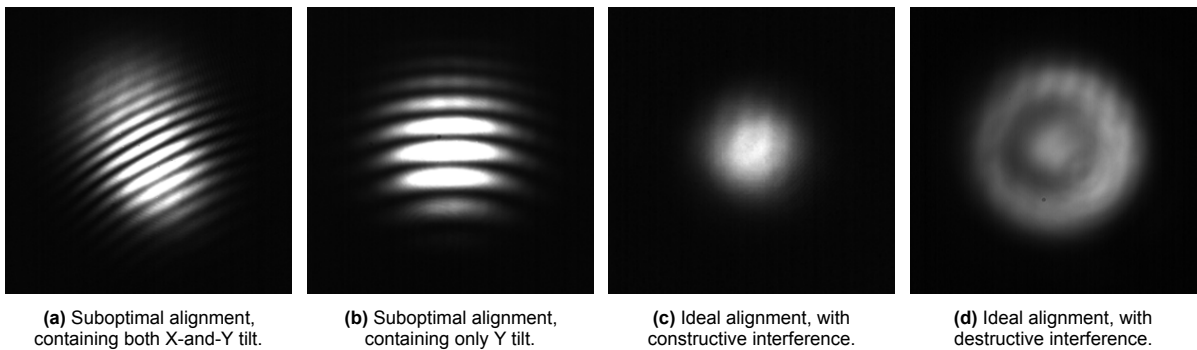


Figure 3.9: Interference image of the fixed and delayed beam, captured with an infrared camera. Figures 3.9a, 3.9b show the interference pattern that is present when X-Y-tilt and Y-tilt is present respectively. Figures 3.9c and 3.9d show the correctly aligned spot, with constructive and destructive interference respectively. Each image represents a size of $5.44 \text{ } [\text{mm}] \times 5.44 \text{ } [\text{mm}]$ on the IR camera sensor.

Given that the produced spot satisfies the requirement, all that is left is to place the photodiode at the center. This procedure was performed as follows:

1. Turn on the laser source.
2. Bias the modulator at the maximum point.
3. Read out the photodetector voltage using the oscilloscope.
4. Isolate the fixed beam from the delayed beam, and vice versa. (This can be achieved easily by placing a piece of paper between the beamsplitters and the delay line, or between the beamsplitters.)
5. Using a 3D-translation stage, the position of the photodetector is adjusted until the voltage is maximal.

Although the requirement is now satisfied, it is important to note that a large portion of the total power of the spot is not seen by the photodiode. Although this could be fixed by using a focus lens, it is not required for the purpose of this thesis and further complicates the alignment process.

3.3. Bias Control Performance

When performing OOK or DPSK modulation, it is critical that the desired bias point remains consistent. Because the modulator's bias voltage is known to drift over time, the MBC corrects for it with an active control loop. Although visual inspection is sufficient to confirm that it works as intended, the maximum error should be quantified, so that we can be sure that at any point in time the modulator is producing a signal within an acceptable margin.

In section 3.1, the half-wave voltage V_π , was determined using a method that requires the modulator to be biased precisely at the maximum point. With the input signal being a sine-wave, this could be confirmed by observing that the uneven harmonics (1st, 3rd etc.), disappear in the spectrum view of the output signal. The degree to which these uneven harmonics are removed can be used to determine the error in the DC bias voltage (V_{DC}). Performing this test and observing the spectrum, it was seen that the 1st harmonic is not fully removed. Instead it fluctuates between completely disappearing into the noise floor and showing a noticeable peak.

To find the error in the biasing, a spectrum for the simulated signal needs to be produced that has the same magnitude for the first harmonic. Looking at the transfer function in the equation below, this is achieved by varying ϕ_{bias} .

$$P_{out}(t) = P_{in} \left[\cos \left(\phi_{bias} + \frac{V(t)\pi}{2V_\pi} \right) \right]^2 \quad (3.2)$$

Because the first harmonic fluctuates, a worst-case scenario was used to determine the error. Both the real spectrum for this test and the simulated signal can be seen in Figure 3.10. Although the first (and third) harmonic are still clearly present, considering that it is on a logarithmic scale, their impact on the signal is of small significance.

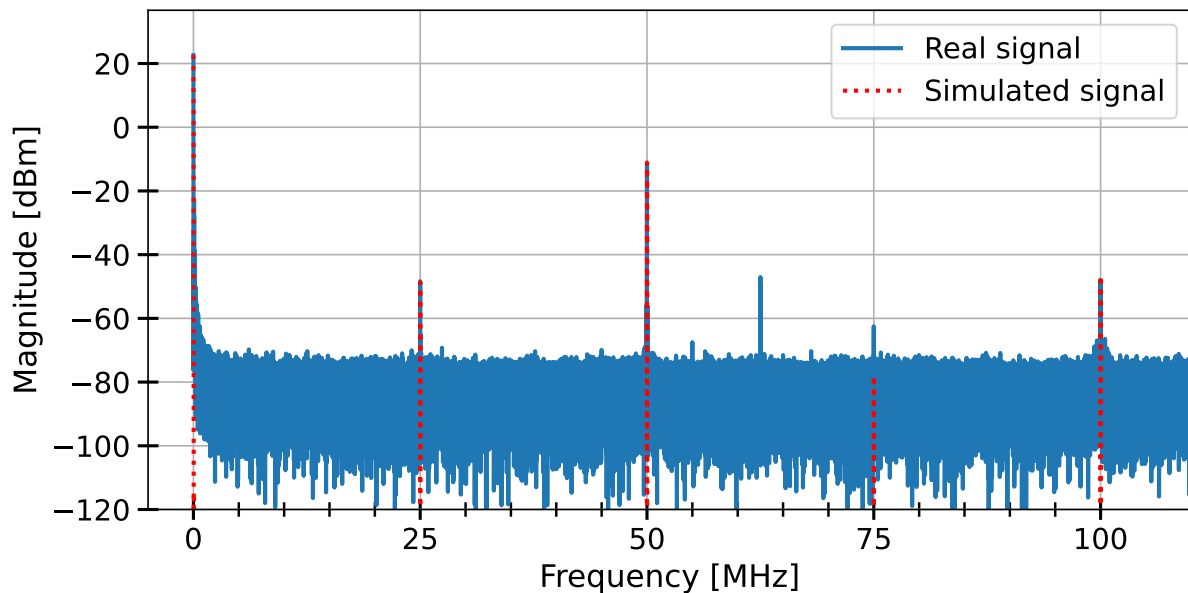


Figure 3.10

Using this simulation, it was found that $\phi_{bias} = 0.0015$ [rad], which is equivalent to 0.086° . For DPSK, this phase difference is negligible. Therefore, it can be concluded that the MBC performance is satisfactory for reliable testing.

3.4. Verification of DPSK Demodulation

At this stage, the primary verification has been completed, and in theory, the final tests can be performed. However, it is essential to verify that the setup actually performs DPSK demodulation rather than a form of direct detection, to fulfill the requirement **FR4**.

The method to verify this is by simulating the output in the case that the fixed (reference) and delayed beam are purely intensity signals. If the actual output with the delay line matches that of the simulation, the demodulator does not function correctly. To achieve this, the fixed beam and delayed beam need to be isolated from each other and measured separately on the photodetector.

The results of this test are illustrated in Figure 3.11. The combined signal was recorded with the condition that the phase between the delayed beam and the fixed beam was 90° (or $\pi/2$), creating constructive interference. (As will be seen in the results section, this condition is not always achieved). The simulated signal is created by adding the isolated signals together, where one of the signals is delayed by 1 bit duration.

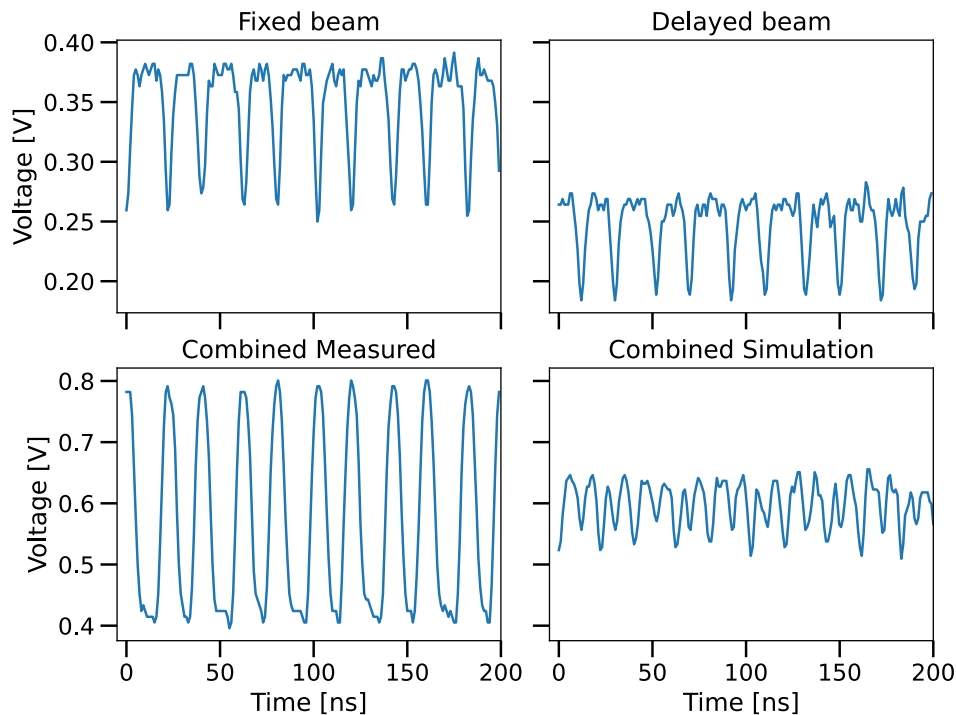


Figure 3.11: Photodetector voltage over time for isolated and combined beams for DPSK modulation. The top row shows the isolated signals for the fixed and delayed beam. The delayed beam has a delay of 1 bit duration with respect to the fixed beam. The 'Combined Measured' signal shows the actual voltage when both beams interfere constructively. The 'Combined Simulation' signal is made by adding the fixed and delayed beam. The difference between the actual and simulated signal implies that DPSK demodulation is working correctly.

At first glance, it is apparent that the overall voltage level of the fixed beam is higher than that of the delayed beam. This is because the delayed beam divergence is 32% larger than that of the fixed beam.⁴ With a higher divergence, the power is more distributed, leading to a lower power in the center where the photodiode is placed. This difference makes interference less effective. To illustrate this, for constructive interference, around 25% (1.25 dB) of the maximum intensity is lost. (See Figure B.3 in the appendix for the precise effects of the same and different divergence.)

The second observation is that the duration of the maximum voltage level alternates between short and long. As seen in Figure 2.17 this is caused by the signal generator itself, where the square wave has an unequal duty cycle for the low and high pulse.

⁴The exact beam parameters can be found in the Appendix section B.

The combined measured signal shows a clear square wave pattern with a frequency of 50 [MHz] (or a data rate of 100 [Mbit/s]), which is expected. The combined simulated signal is more irregular, lower in voltage levels, and has a higher main frequency at 100 [MHz]. This already shows that the real signal is produced with DPSK demodulation and not just a combination of intensity signals.

Another simple way to confirm this is to look at the maximum voltage levels of the isolated beams. For the fixed and delayed beam, the maximum voltage is 0.39 [V] and 0.28 [V], respectively. If these were purely incoherent intensity signals, combining them would only yield 0.67 [V], which is lower than the 0.80 [V] maximum in the real combined signal. This can only be explained by the interference of coherent beams. Therefore, it can be confirmed that the setup is performing the DPSK demodulation correctly, albeit with a significant loss caused by the difference between the two beams.

A more intuitive way to confirm the demodulation of DPSK is to look at the spot with the infrared camera and to vary the frequency of the modulator's input signal. Because the frame rate of the camera is much lower than this frequency, when the frequency matches that of the delay line, the square wave that is produced will be averaged and result in a uniform Gaussian spot. Subsequently, when the frequency is varied to mismatch the delay line, the interference pattern will appear. By sweeping through these frequencies the functioning of the delay line was also inferred visually.

3.5. Final Setup and Test Plan

Now that all the verification tests have been completed, the final research question can be addressed. To do this, performance must be evaluated. Referring back to the modulation scheme trade-off, the only criterion of it that can be tested is power efficiency. Specifically, this relates the SNR to the BER of the received signal. By finding the BER at specific SNR's, the curve can be constructed and compared to the ideal additive white Gaussian noise (AWGN) curve. There are two primary ways to vary the SNR: by varying the data rate or by varying the signal power.

Given that the data rate is restricted by the signal generator and delay line, varying the power is the only way to alter the SNR. Since the laser is already set on the lowest possible power, additional NDF's are placed right after the fiber mount.⁵ With various combinations of the NDF's, different SNR's can be reached. The SNR range that must be tested is related to the BER range of interest. To test requirement **FR2** it is necessary to test a BER range of at least 10^{-2} to 10^{-4} .

The NDF's are placed in front of the first beamsplitter such that power reductions for single and balanced detection are consistent. A top view of the balanced detection optical setup can be seen in Figure 3.12. Additional images of the setup can be seen in Figures 3.13, 3.14 and 3.15.

Furthermore, the most important parameters used for the final tests have been summarized in Table 3.1.

Table 3.1: Summary of the most important parameters used for the final tests.

Parameter	Value
Data Rate	100 [Mbit/s]
Square wave frequency	25 [MHz]
DLI Length	1.5 [m]
Half-wave voltage V_{π}	3.56 [V] ^(a)
Sampling rate	1.0 [GS/s]

(a) In Figure 3.3, the V_{π} at 25 [MHz] was determined to be 3.53 [V]. However, tests were conducted with 3.56 [V] due to a calculation error discovered later. This difference is within the margin of error and has little to no impact on the results.

⁵With the placement of NDF's, alignment may be changed slightly. To avoid this, alignment is checked with and without the NDF placement to ensure no differences throughout testing.

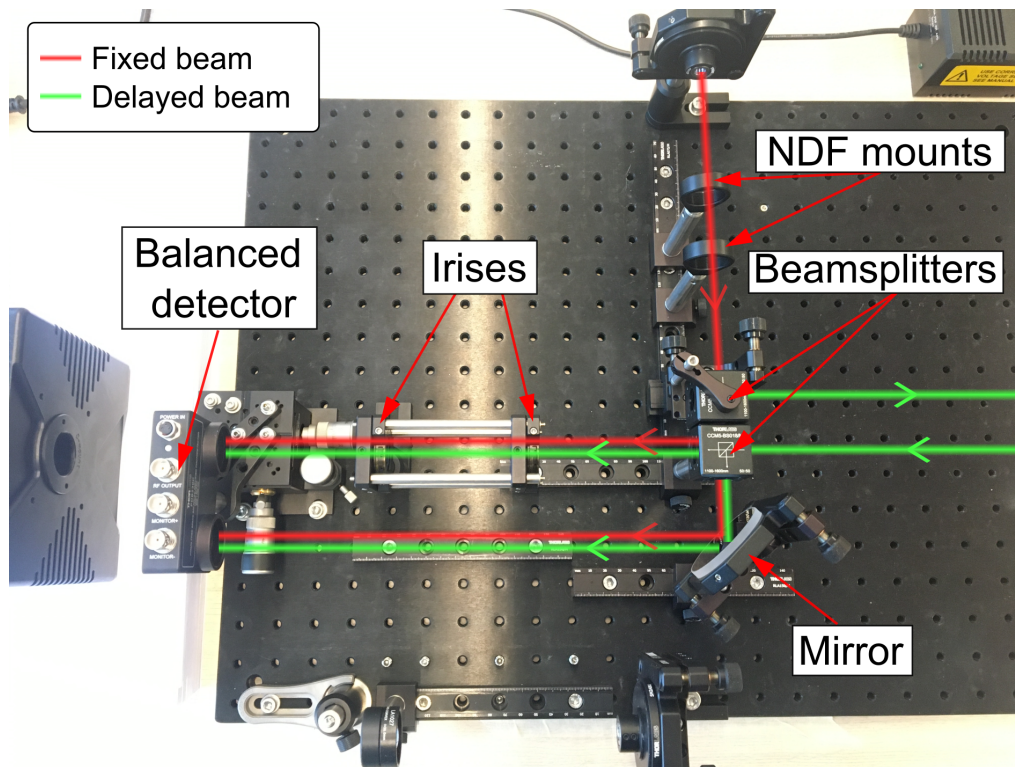


Figure 3.12: Top view of the balanced detection optical breadboard designed for performing DPSK demodulation. The delayed beam is aligned to reflect back using a prism that can be seen in Figure 3.13

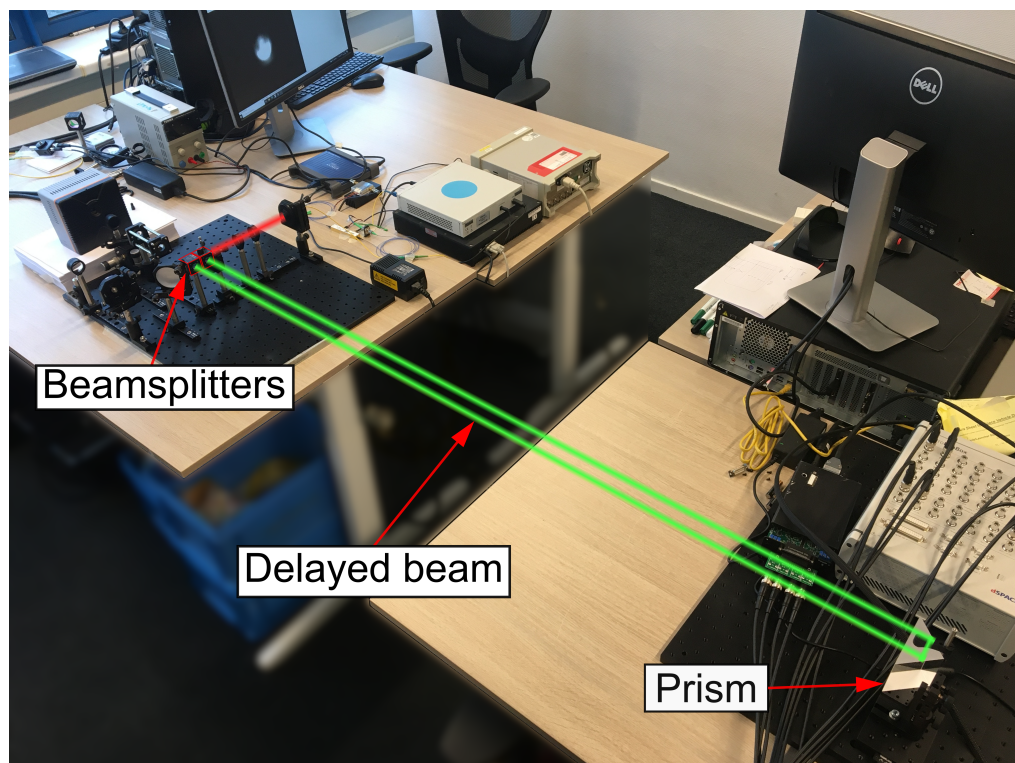


Figure 3.13: View of the final hardware setup, showing the entirety of the delay line. Two beamsplitters and a prism are used to complete the delay line.

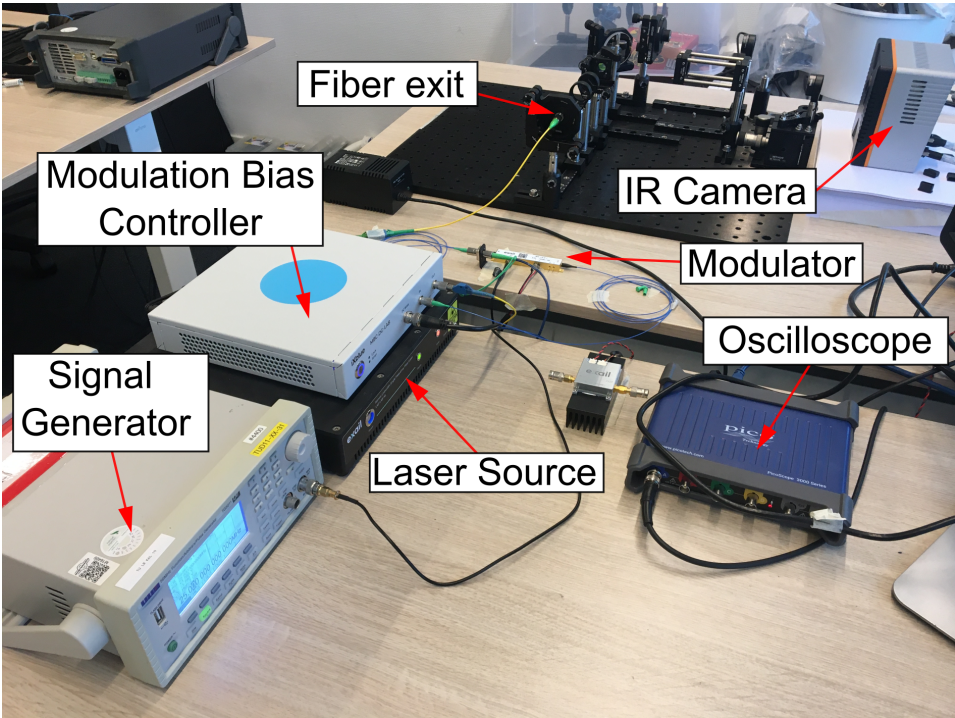


Figure 3.14: Front view of the hardware setup, including the components needed to transmit, receive and process the signal.

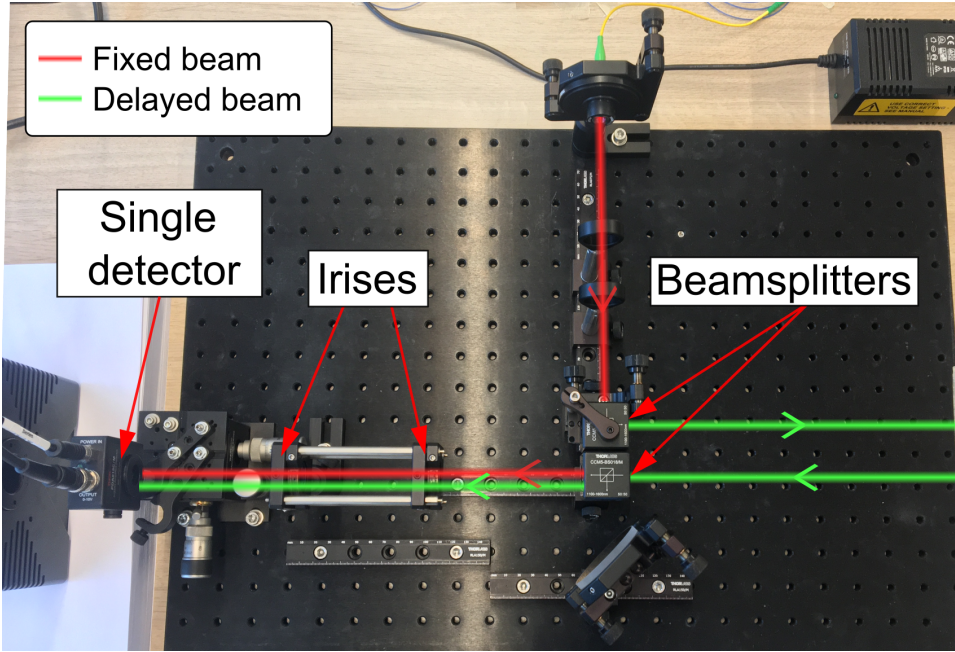


Figure 3.15: Top view of the single detection optical breadboard designed for performing DPSK demodulation.

4

Results and Discussion

With the detection setup implemented and verified, the tests presented in the previous chapter can be carried out, so that research question 3 can be answered. This chapter presents the results of the tests, followed by a discussion. The first section focuses on the stability of the test setup and evaluates how consistently it operates at maximum power levels. The second section addresses communication performance, examining the relation between SNR and BER. Finally, in the discussion, the results of the stability and communication performance assessments are analyzed.

4.1. Stability

As discussed in subsection 2.1.2, the working principle of a DPSK detector is the precise introduction of a time delay T_s and phase shift φ_{DLI} of the optical signal. Although the exact time delay is important, it is less susceptible to fluctuations and drift as the phase shift. To illustrate, a 390 [nm] change in the delay length is sufficient to induce a 90° phase shift, while introducing only a time delay in the order of 10^{-15} [s]. With a data rate in the order of Mbit (or even Gbit), such a shift in time is negligible to overall performance.

To characterize the variability of the phase shift, we need to observe the change in the interference pattern. In section 3.2, it was shown that the phase shift in the delay line changes the magnitude of the center of the spot. Therefore, by measuring this magnitude over time, the variability of the phase shift can be inferred. This requires no additional phase or magnitude change to be introduced, so no signal should be applied on the modulator.

The test setup is the same as for single detection DPSK, instead now we bias the modulator on the maximum and apply no RF signal. For the 15 [m] delay line, the photodiode output can be seen in Figure 4.1

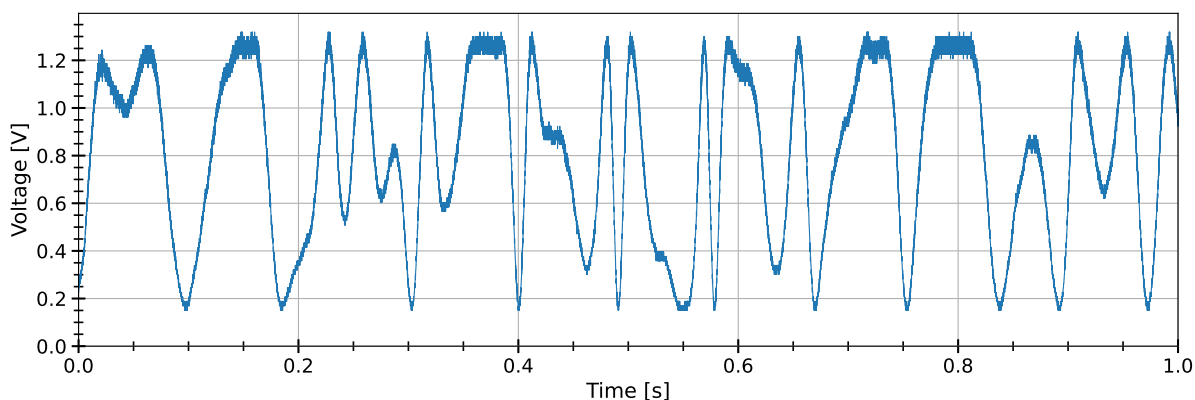


Figure 4.1: Voltage output of the photodiode over time, with the modulator biased on the maximum operating point.

Ideally, it should stay on either the maximum or minimum voltage level continuously, but as seen in the figure, the output is highly unstable. The longest duration for which it remains stable is approximately 30 ms. Furthermore, it also spends a significant amount of time outside the minimum and maximum voltage levels. For this particular waveform 81% of the time is spent outside the maximum and minimum voltage levels (including a 10% rise/fall).

There are multiple explanations for why this instability occurs. For a bulk optics delay line, several environmental factors influence the introduced phase variation. Firstly, mechanical vibrations affect the placement of the beamsplitters relative to the prism, which alters the path length, shifting the phase. When the length of the delay line is increased, the exposure to mechanical vibrations increases. Furthermore, the way the beamsplitter and prism are coupled is important. When rigidly mounted to the same optical breadboard, any vibration effecting the breadboard is translated onto both the prism and beamsplitters, which is to say that they are coupled. In the final setup however, this is not the case, and the prism and beamsplitters are mounted on different breadboards on different tables. This decoupling causes any mechanical vibrations to affect the total optical path length to a higher degree.

Secondly, temperature fluctuations affect the index of refraction, thereby changing the total optical path length and, consequently, the phase shift. The length of the delay line determines the amount of air the light has to travel through. The longer the delay line, the higher the probability for there to be variations in temperature, both in time and space. Therefore a shorter delay line would be less susceptible to temperature fluctuations.

To make the delay line more stable, both reducing the length and placing it on the same optical breadboard should be effective. To test this hypothesis, an additional stability test was performed with the prism mounted on the same breadboard as the beamsplitters in combination with placing it more closely. This can be seen in Figure 4.2.

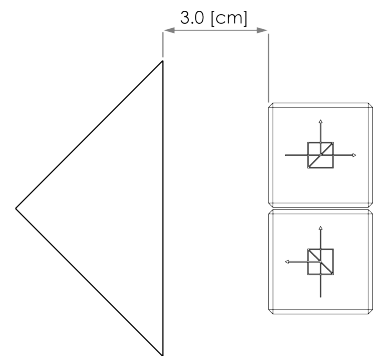


Figure 4.2: Schematic of the closer prism placement with respect to the beamsplitters.

The results of the test can be seen in Figure 4.3a. It is observable that the signal is much more stable, staying at the minimum voltage level for a duration of 2 [s], which is the total time of the waveform. But without any disturbances, it could continue like this indefinitely. To show the response to disturbances (particularly mechanical vibrations), intentional oscillations were introduced with light taps on the table. The response to such a single disturbance can be seen in Figure 4.3a. Although the signal experiences a high amount of fluctuations during the disturbance, it settles. Considering these results, it is clear that a shorter delay line, where the optical elements are coupled, greatly improves stability. However, as discussed in section 2.4, the length of DLI was restricted by the modulation speed of the signal generator, and therefore all DPSK tests must be performed at a length of 1.5 [m].

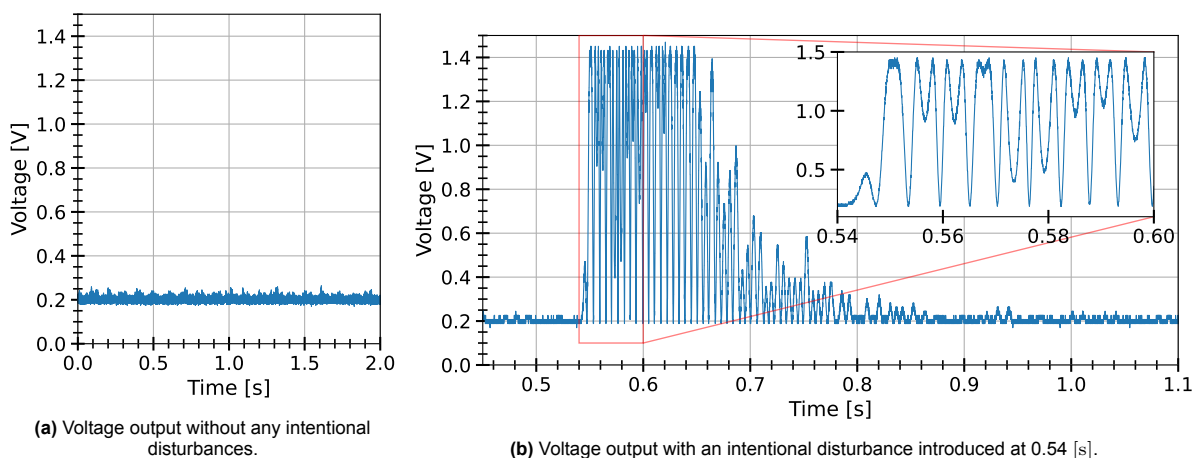


Figure 4.3: Voltage output of the photodetector with the prism placed 3 [cm] away from the beamsplitters.

Another way to compare the stability of both delay lines is by looking at their respective frequency responses. Both the 'long' (1.5 [m]) and 'short' (3 [cm]) delay line frequency responses can be seen in Figure 4.4. When comparing the two responses, the long delay line contains much more energy in the 0-100 [Hz] range than the short delay line, again showing that the long delay line is much more unstable than the short one.

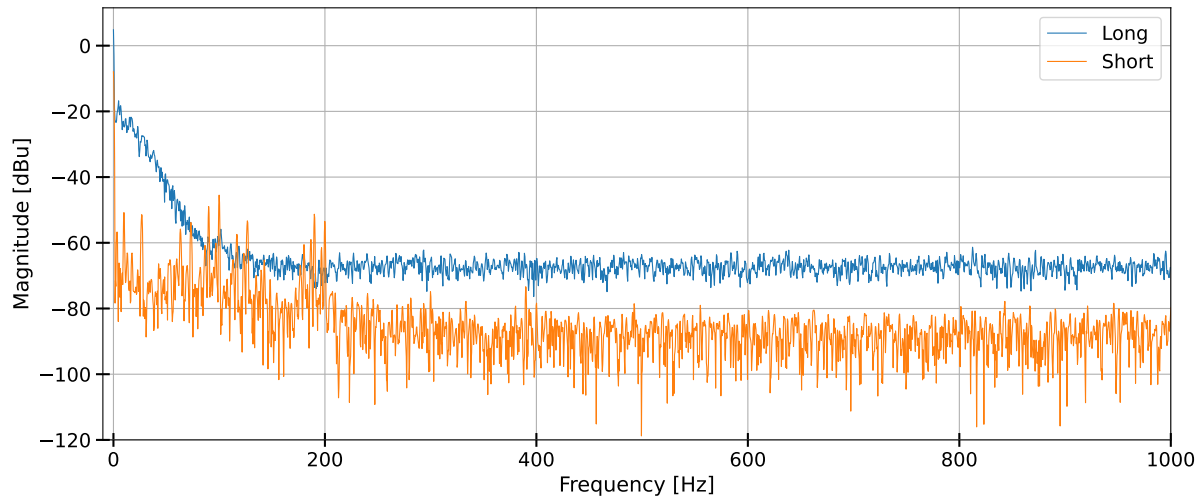


Figure 4.4: Frequency response up to 1 [kHz] for the long and short delay line. 'Long' and 'short' denote the lengths of the delay line, at a distance of 1.5 [m] and 3 [cm] respectively. The higher magnitudes for the long delay line in the low frequency range show it is much more unstable than the short delay line.

4.2. Communication performance

There are many ways to quantify the communication performance of a link. Two popular metrics are the Bit Error Rate (BER) and Packet Error Rate (PER). In real systems, the PER is often more relevant, since error correction methods are employed to correct for individual bit errors within a packet. However, testing the PER is not possible with the available signal generator and is not necessary to test the requirement. Therefore, the method used here is to evaluate the BER at various power levels.

To determine the BER for a given signal, a voltage threshold must be chosen, as well as the points in time at which the signal is sampled. Firstly, to determine the optimal threshold, a probability distribution must be generated at the sampling times. This can be done by constructing an *eye diagram*.

In essence, an eye diagram is made by cutting a signal at every bit length and superimposing it on top of each other. By finding out the number of times these signals overlap in each pixel, a 2D histogram can be created. An example of an eye diagram for a received OOK signal can be seen in Figure 4.5.

The eye diagram gets its name from the shape seen in the middle, which roughly resembles the shape of an eye. The color bar in the plot indicates how many times the signal overlaps/crosses itself at that point. This occurs most frequently at what is called the 'cross point' and can be seen twice for this signal. Upon close inspection, it is apparent that this particular eye diagram looks different from those typically seen in the literature. Specifically, the minimum and maximum voltage levels would be continuous and would not contain a gap as seen in the figure. This is because BER tests are performed with a PRBS, which contains sequences of repeating bits, unlike the purely alternating bits from a square wave.

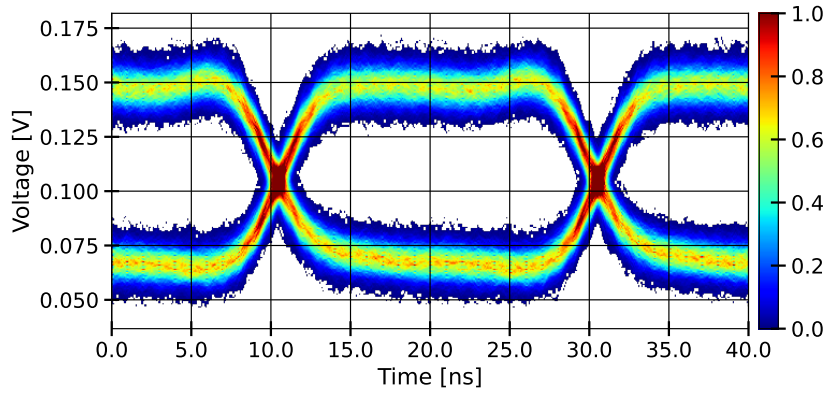


Figure 4.5: Eye diagram of a 50 [Mbit/s] OOK signal with a square wave input. The color bar represents the number of times the signal overlaps on a single pixel. The maximum and minimum number of counts are normalized to 1.0 and 0.0 respectively.

Using this eye diagram, the probability distribution can be found by slicing the eye diagram vertically at the desired time. For this example, the distribution at 20 [ns] can be seen in Figure 4.6

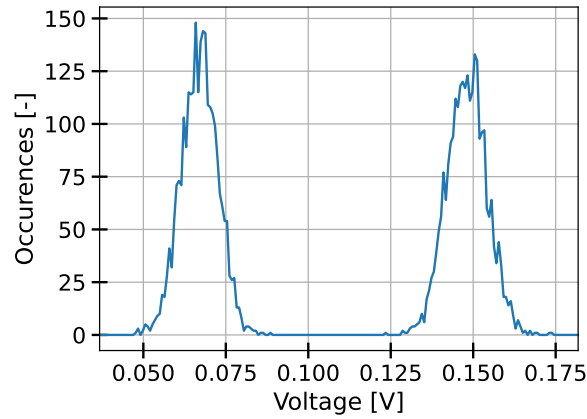


Figure 4.6: Probability distribution at 20 [ns], for the signal in Figure 4.5.

This distribution can be approximated using two Gaussian curves. Subsequently, the optimal threshold is determined by finding the intersection between the two curves. An example of two Gaussians fitted to the data of the eye diagram can be seen in Figure 4.7. Using the parameters of each Gaussian fit, the SNR can be determined as follows:

$$SNR_{Eye} = \frac{L_1 - L_0}{\frac{1}{2} \cdot (\sigma_1 + \sigma_0)} \quad (4.1)$$

where L_1 and L_0 are the means, σ_1 and σ_0 are the standard deviations of the two Gaussians. Subsequently the power SNR is calculated by squaring the eye SNR:

$$SNR_{Power} = \left(\frac{L_1 - L_0}{\frac{1}{2} \cdot (\sigma_1 + \sigma_0)} \right)^2 \quad (4.2)$$

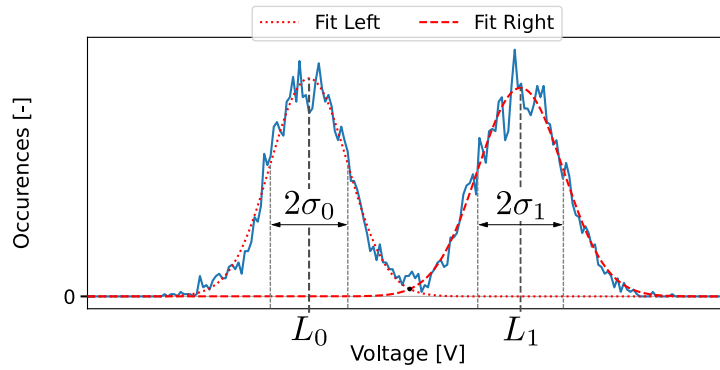


Figure 4.7: Example of Gaussian fits of the probability distribution from an eye diagram. The mean and standard deviations are denoted with L_i and σ_i respectively.

Making eye diagrams for DPSK is less straightforward than for OOK, since the delay line is highly unstable. For about 80% of the time, the signal does not reach its optimal SNR. Therefore, any BER determination would depend entirely on the phase change inside the delay line at that time, which is not representative of the system performance. Given that there is no way to correct for the instability at this time, instead only sections of the waveform are used that have the optimal SNR, satisfying the 90° phase difference condition. Sections that do not satisfy this condition dramatically exceed the BER requirement of 10^{-3} and are therefore not discussed here. To see the performance outside of the best SNR, see appendix section C.2.

For the best sections of the signal, examples of eye diagrams of a DPSK signal can be seen in Figures 4.8 and 4.10 for single and balanced detection, respectively.

In both eye diagrams, four crossing points can be seen. These are caused by the signal generator producing a square wave with unequal durations for the high and low voltage. Furthermore, for balanced detection, the center of the eye crossing is not exactly located at 0.00 [V], but has a slight offset of -0.007 [V].

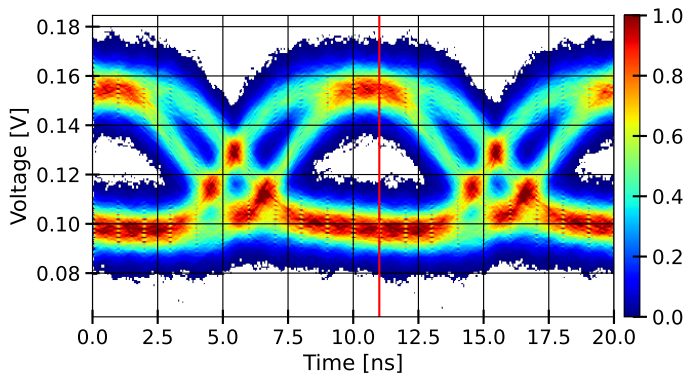


Figure 4.8: Eye diagram of a 100 [Mbit/s] DPSK signal detected with a single photodetector. The red line shows the sampling time for which the SNR is optimal. This signal has a SNR of 19.28 [dB].

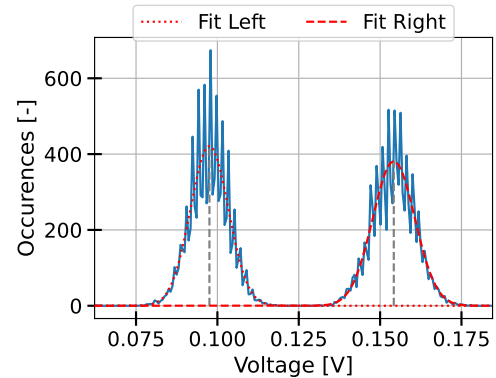


Figure 4.9: Probability distribution at the sampled time seen in Figure 4.8. The distribution has been fitted with two Gaussians, one for the left and one for the right bit.

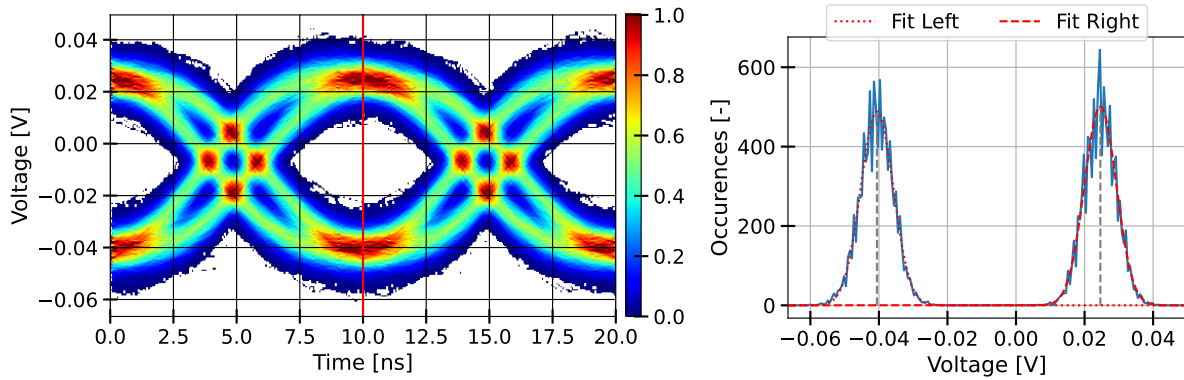


Figure 4.10: Eye diagram of a 100 [Mbit/s] DPSK signal detected with a balanced detector. The red line shows the point where the sampling time for which the SNR is optimal. This signal has a SNR of 22.83 [dB].

Figure 4.11: Probability distribution at the sampled time seen in Figure 4.10. The distribution has been fitted with two Gaussians, one for the left and one for the right bit.

Using the eye diagram, the time at which it should be sampled can also be determined. For the best BER, the time index that has the maximum SNR should be chosen. Subsequently, because the expected data is known to be a square wave, all wrong bits can be determined. For the stable/optimal sections of the signals, the SNR-BER curve can be created by determining the BER and SNR for a number of different signal powers. This power is varied using NDFs, thus creating a range of SNRs and BERs. Finally, a polynomial can be fitted to the data points. For each point a 95% confidence interval is added in the form of an error bar to account for the number of samples that were used to determine the BER. These intervals were calculated using the Wilson score interval.

The results for a single and balanced detection DPSK BER curve are shown in Figure 4.12. In addition, OOK was also tested and is presented in Figure 4.13.

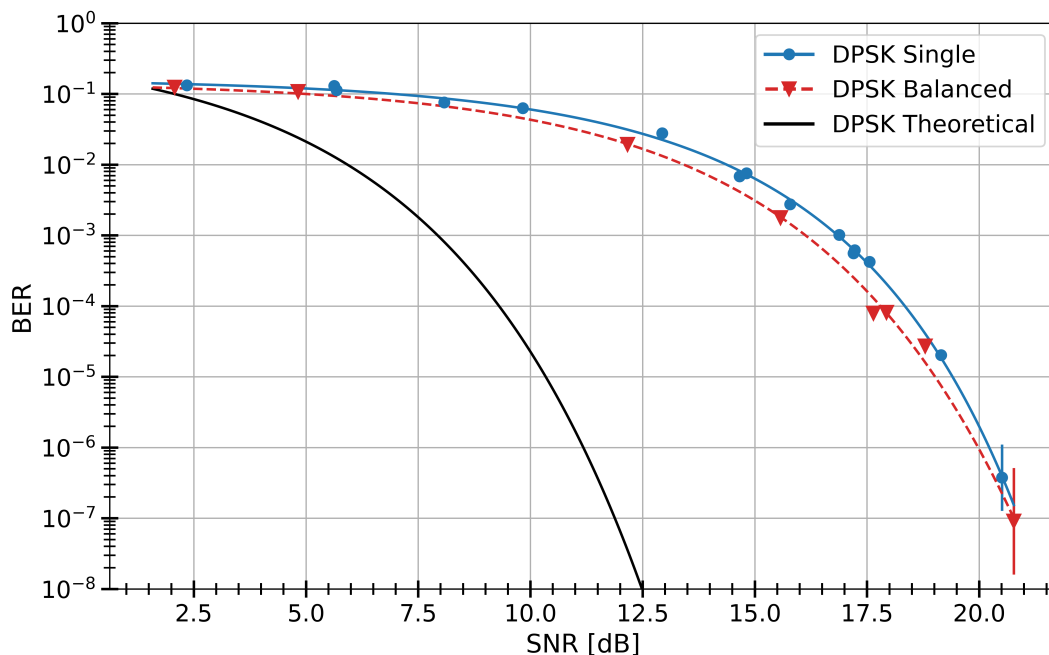


Figure 4.12: BER performance of the DPSK modulation scheme, for a single detector and a balanced detection setup. Error bars indicate a 95% confidence interval. Some error bars are obscured by the size of the markers.

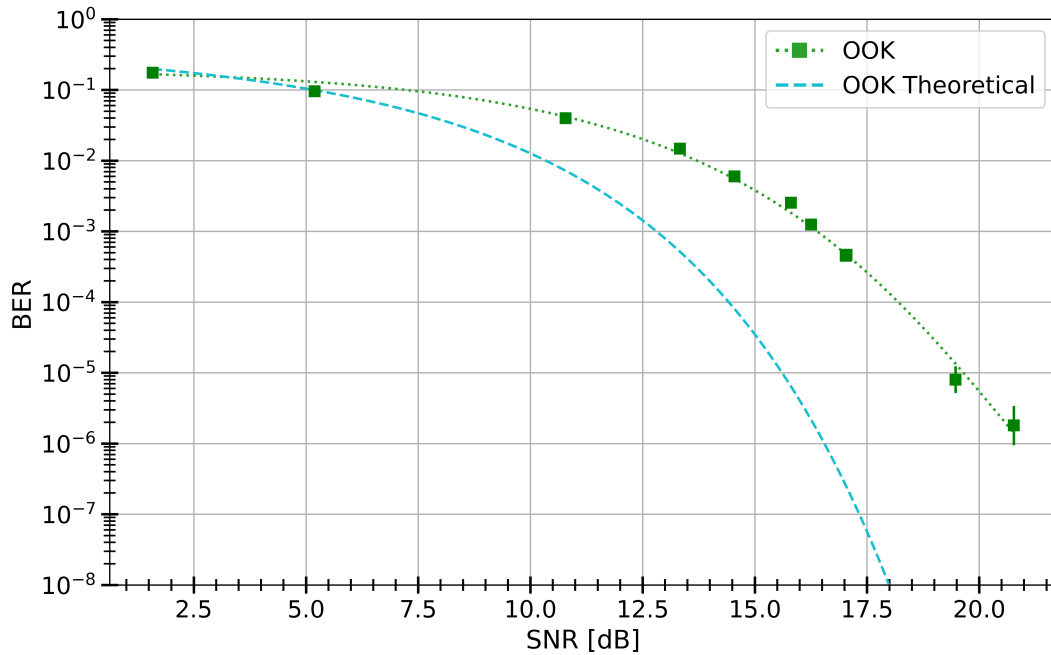


Figure 4.13: BER performance of the OOK modulation scheme.

Analyzing the BER curve for DPSK, a significant SNR penalty with respect to the theoretical/ideal DPSK performance can be seen. At a BER of 10^{-4} there is a 8.5 [dB] difference. Between balanced and single detection, the SNR advantage is 2.9 [dB] for the highest BER's, going down to 0.1 [dB] for the lowest BER's.¹

For OOK at a BER of 10^{-4} there is a SNR penalty of 3.7 [dB] with respect to the theoretical AWGN case.

Returning to Research Question 3; "What is the performance of the implemented detection system?", we can answer that:

- The interferometer is highly unstable, which does not allow continuous operation. Therefore, the BER requirement of $< 10^{-3}$ (FR2) was not met.
- Ignoring these unstable moments, DPSK communication is carried out successfully at a data rate of 100 [Mbit/s], albeit with a SNR penalty, which can be seen in Figure 4.12.

4.3. Discussion

This section will explain the discrepancies in the analysis. In addition, the relevance of the project to actual implementation in satellites is discussed.

Delay line instability

As seen in the results, the main issue with the receiver is the instability of the delay line. The primary cause of this instability is the lack of mechanical coupling between the prism and beamsplitters, as they are not mounted on the same optical breadboard. This is exacerbated by the long length of the delay line, which introduces even more phase shifts caused by temperature differences in the air.

In a lab environment, this issue can be easily solved by shortening the delay line so that both the prism and beamsplitters fit on the same optical breadboard. Mounting the prism close to the beamsplitters on the same breadboard resulted in a stable delay line.

¹This difference highly depends on the curve fit of the points. If any one of the points on changes, the fit of the curve and subsequently the SNR difference also changes. To see the full difference across the SNR range, see Figure C.17 in the appendix.

However, shortening delay line demands an increase in the data rate of the link. This makes it so that this kind of DPSK receiver architecture is heavily favored towards high data rates. For small satellite form factors like the CubeSat, realistically the delay line cannot exceed more than 9 [cm] at best. This is equivalent to a data rate of 1.67 [Gbit/s].

Even when the delay line is shortened, control over the phase shift in the delay line is required. In a lab environment, this can be achieved by using fine translation stages. In orbit, vibrations would not be a significant issue, but thermal expansion/contraction is enough to offset a delay line over time. So for actual implementation, a dedicated stabilizer/control mechanism of the delay line is needed. This can be done with a motorized fine translation stage combined with a PLL or amplitude modulated pilot tone.

Performance penalties

As seen in the results, both the OOK and DPSK performance is far from ideal. Focusing solely on DPSK, a SNR penalty of 8.8 dB was observed at a BER of 10^{-6} between AWGN (ideal) and real balanced detection. This penalty can be attributed to a number of factors, which have been listed below.

- Because the divergence of both beams is not equal, the power at the center of each beam differs, leading to inefficient interference and significant power loss. Another power difference between interfering beams is caused by unequal beam splitting.
- The selection of 'stable' waveforms has been done manually, and some variation is still present between them.
- There are many sources of noise that are not purely AWGN. They come primarily from the detector. For the detector, significant sources of noise are: thermal noise, shot noise, and dark noise. The laser noise sources like frequency noise, phase noise, and Relative Intensity Noise (RIN) are negligible compared to detector noise.
- The oscilloscope has 10 samples per bit and no timing recovery loop, which results in the fact that the optimal SNR of the signal does not always occur exactly at the sampling time. If the channel does not contain purely AWGN, the BER equation no longer holds for this suboptimal SNR, causing deviations.
- The square wave from the signal generator has a significant rise/fall time and an unequal duty cycle for the high and low pulse, narrowing the optimal sampling window and thus more likely to sample at suboptimal SNR's.
- The determination of the SNR relies on the construction of an eye diagram and fitting Gaussian curves to the probability distributions. These are only approximations, which means that the threshold that is chosen is not perfect.
- Because the oscilloscope uses 8 bits to represent the voltage, at the sampling time, many samples will register the same voltage. Consequently, when making the eye diagram, at the sampling time, the probability distribution will not be entirely smooth but contain spikes. This can be seen in Figure 4.9. This causes the Gaussian fit to be less reliable.
- The dither signal applied by the MBC to control the bias point of the modulator is an additional noise source on the transmitter side.
- The delay line may not be perfectly matched to the data rate and may differ by 0.5 [cm]. For the balanced detection setup, the path length from the mirror is longer by 5-6 [cm]. Together, these facts would lead to an SNR penalty of around 0.3 [dB]. [59]

Coherent satellite receiver architecture

An important result that cannot be directly quantified is how difficult it is to implement a DPSK free space detector. In the initial trade-off, DPSK was said to be easier to implement than BPSK, but this statement comes with a few conditions. Firstly, it depends on the right equipment being available. A slow signal generator requires a longer delay line, making it more difficult to implement. Secondly, DPSK is described to be much easier than BPSK because the most common architecture uses a fiber-based delay line. Although this does not fundamentally change the functioning of the demodulator, a fiber-based delay line can be designed for a much wider range of data rates. In addition, it is more

stable and a stabilizer in the fiber domain is easier to implement. Regarding the overall complexity of implementing DPSK, it is much more difficult than OOK. Besides the precise alignment needed for interference, ensuring the DLI is stable can be a major challenge.

For the fiber-based DPSK architecture the primary issue is that it requires fiber coupling. If fiber coupling is going to be performed in a CubeSat, it seems more reasonable to immediately switch to modulation schemes like BPSK or QPSK since their receivers have been implemented many times before. Another important consideration is the photodiode size. For free space detectors, a larger photodiode makes alignment easier for focusing. At the same time, a larger photodiode comes at the cost of a lower bandwidth, which translates to a longer delay line. In addition, a larger photodiode necessitates a larger fringe width, which requires good alignment and collimation. This creates a trade-off between data rate, alignment requirements and SWaP. For smaller satellites at high data rates, this means alignment is more stringent for focusing, but easier in terms of fringe width.

More importantly, the stability of the DLI needs to be ensured in actual LCT's. Although a closer prism placement that is coupled to the beamsplitters leads to a much more stable signal, active stabilization is still likely needed to deal with temperature effects in space. This would include the need for controllable translation stages and a PLL or amplitude modulated pilot tone. In turn, this complicates the DPSK bulk optics receiver. Although a complicated DSP approach for homodyne BPSK detection was not chosen for this thesis, it could be an attractive option for implementation as a free-space detector.

So, while a bulk optical DPSK detector is possible, it requires very high data rates to operate inside a small form factor if one were to choose this 'single prism' architecture. The alignment requirements this imposes should be weighed against the difficulty of fiber coupling.

Regarding the trade-off, many improvements could be made in retrospect. For instance, too little emphasis was put on the implementation difficulty and the simplicity of DPSK was overestimated. Other criteria like transmission reliability were likely given too much weight, given that the data highly depends on how a modulation scheme is implemented. Although it is useful as an approximation, it is not as important as the implementation difficulty. Still, given the hardware that was available, the choice for DPSK remains the most suitable choice for this thesis project.

5

Conclusion and Recommendations

This final chapter will provide a conclusion to the research that has been done, and several recommendations for future work.

5.1. Conclusion

This thesis successfully demonstrated the design, implementation, and evaluation of a coherent free space Differential Phase Shift Keying (DPSK) detection system using bulk optics. The research was motivated by the growing demand for high-bandwidth data transmission in satellite constellations and the advantages of free space optical (FSO) communication over traditional radio frequency (RF) systems.

The research centered on developing a coherent detection system that does not rely on fiber coupling, which is among the most difficult challenges associated with current laser communication terminals (LCTs). By avoiding fiber coupling and the associated systems that are required, the proposed system aims to simplify the design, reduce complexity, and potentially lower costs for future LCT implementations.

In the context of FSO, coherent modulation schemes like PSK enable the higher data rates that cannot be achieved as easily with more traditional schemes like On-Off Keying. Out of the many different coherent schemes, DPSK was chosen to implement because it had similar good performance compared to other coherent detection schemes and also has a simpler architecture that only requires a Delay Line Interferometer (DLI).

The receiver was implemented with successful demodulation of DPSK, but its performance did not meet the required standards. Specifically, the DLI was too unstable, which caused the bit error rate (BER) to significantly exceed the BER requirement of 10^{-3} at times. The instability of the DLI was caused by the large distance needed to create the delay needed for DPSK, which is inversely proportional to the data rate. Due to hardware constraints, a higher data rate could not be chosen.

Ignoring these unstable moments, a data rate of 100 [Mbit/s] was achieved. Using these stable/optimal moments a BER curve was constructed, which relates the BER to the SNR. For balanced detection of DPSK a SNR penalty of 8.5 [dB] was observed with respect to the ideal DPSK performance. One reason for this is the large beam divergence of the delayed beam.

From these results and the entire implementation process, several insights were gained:

- The implementation of DPSK using bulk optics is highly favored toward data rates in the [Gbit/s] range.
- Although a shorter DLI is passively stable, for actual implementation in satellite LCT's active stabilization methods are required. The methods needed to enable this are not much different than other control methods for coherent detection. Homodyne detection of BPSK using a free-running local oscillator may be worth exploring.

- The performance of the signal generator imposes significant constraints on the entire receiver architecture for DPSK demodulation. For many multi-frequency signal generators, the signal degrades as the frequency increases. In particular, its rise/fall time increases, resulting in only a small amount of time in which the signal can be sampled optimally, which degrades the BER.
- Optical alignment can be done in many different ways, and there is no single correct method. The approach that was found most effective for this thesis was to only add degrees of freedom where necessary, and otherwise remove them.
- The half-wave voltage of a Mach-Zehnder Modulator is specific to the output of the signal generator and cannot be separated from one another when testing.

5.2. Recommendations for future work

Over the course of this thesis, many decisions have been made which in retrospect were not all correct. The recommendations can be roughly divided into two parts:

1. Specific recommendations pertaining to the setup that has been constructed in this thesis.
2. General recommendations for future research in this area.

Firstly, there are many areas for improvement. The main performance impediment was the instability of the DLI. This can be fixed by using a higher data rate such that the DLI becomes shorter and thus more stable. A faster signal generator with a low rise/fall time would also guarantee that the optimal SNR moment can be sampled. However, this does depend on the sampling rate of the oscilloscope with respect to the data rate. For higher data rates with a limited sampling rate, timing recovery methods should be implemented. In addition to better stability, a shorter DLI also reduces beam divergence, making interference more effective. Other smaller improvements are the use of more accurate eye diagram software and the use of a PRBS signal for a more accurate performance evaluation.

Secondly, there are other options besides the use of a prism or a series of mirrors to create a DLI. One option could be to create length by using an optical cavity where the beams do not interfere with each other. This could be investigated for a free space implementation of lower data rate DPSK detectors.

Other implementations of a DLI-based coherent receiver are also possible. For instance, using two DLI's and a separate intensity detection branch, DQPSK and Star QAM are possible, but these are better suited for larger satellites. [39, p. 67]

Besides DLI-based coherent receivers, actual coherent detectors using LOs may also be worthwhile. If LOs can be miniaturized enough, a free running LO only requires DSP in post-processing. While this is not straightforward, similar methods would also need to be used for stabilization in free space DPSK detectors. This makes free space coherent detection of BPSK another promising alternative for future research.

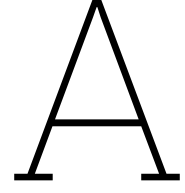
References

- [1] Cisco Systems. *Cisco Annual Internet Report (2018-2023)*. White Paper. Mar. 9, 2020. URL: <https://www.cisco.com/c/en/us/solutions/collateral/executive-perspectives/annual-internet-report/white-paper-c11-741490.html>.
- [2] Alberto Carrasco-Casado et al. "NICT's versatile miniaturized lasercom terminals for moving platforms". In: *2022 IEEE International Conference on Space Optical Systems and Applications (ICSOS)*. Mar. 2022, pp. 213–217. DOI: 10.1109/ICSOS53063.2022.9749711.
- [3] Emily Clements et al. "Nanosatellite optical downlink experiment: design, simulation, and prototyping". In: *Optical Engineering* 55.11 (Sept. 13, 2016), p. 111610. DOI: 10.1117/1.0E.55.11.111610.
- [4] Geuk-Nam Kim et al. "The VISION – Concept of laser crosslink systems using nanosatellites in formation flying". In: *Acta Astronautica* 211 (Oct. 1, 2023), pp. 877–897. DOI: 10.1016/j.actaastro.2023.07.014.
- [5] Aizaz U. Chaudhry and Halim Yanikomeroglu. "Free Space Optics for Next-Generation Satellite Networks". In: *IEEE Consumer Electronics Magazine* 10.6 (Nov. 2021). Conference Name: IEEE Consumer Electronics Magazine, pp. 21–31. DOI: 10.1109/MCE.2020.3029772.
- [6] Gurpreet Kaur, Pratap Ravesh, and Atipriya Sharma. "Space Optical Communication Techniques: A Review". In: *2022 3rd International Conference on Computing, Analytics and Networks (ICAN)*. Nov. 2022, pp. 1–11. DOI: 10.1109/ICAN56228.2022.10007394.
- [7] Chao Zhang et al. "Recent trends in coherent free-space optical communications". In: *Metro and Data Center Optical Networks and Short-Reach Links IV*. Ed. by Madeleine Glick, Atul K. Srivastava, and Youichi Akasaka. Vol. 11712. Online Only, United States: SPIE, Mar. 5, 2021, p. 117120M. DOI: 10.1117/12.2582415.
- [8] Guanhua Wang et al. *Free Space Optical Communication for Inter-Satellite Link: Architecture, Potentials and Trends*. Oct. 26, 2023. DOI: 10.48550/arXiv.2310.17505.
- [9] Bruce Yost and Sasha Weston. *State-of-the-Art: Small Spacecraft Technology*. Tech. rep. Ames Research Center, Jan. 1, 2023. URL: <https://ntrs.nasa.gov/citations/20220018058>.
- [10] Daoman Rui et al. "Probability enhancement of fiber coupling efficiency under turbulence with adaptive optics compensation". In: *Optical Fiber Technology* 60 (Dec. 1, 2020), p. 102343. DOI: 10.1016/j.yofte.2020.102343.
- [11] Neal W. Spellmeyer. "Use of Commercially Available Fiber Optic Components in Emerging Space Laser Communications Applications: Optimizing Performance, Cost, and Reliability". In: *2021 Optical Fiber Communications Conference and Exhibition (OFC)*. June 2021, pp. 1–3. URL: <https://ieeexplore.ieee.org/document/9489456>.
- [12] Mo Chen et al. "Experimental results of 5-Gbps free-space coherent optical communications with adaptive optics". In: *Optics Communications* 418 (July 1, 2018), pp. 115–119. DOI: 10.1016/j.optcom.2018.03.003.
- [13] Scott E Palo, Ryan Kingsbury, and Jon C Twichell. "Cobalt: The Next Step in Low SWaP-C Optical Terminal Design". In: Aug. 4, 2022. URL: <https://digitalcommons.usu.edu/smallsat/2022/all2022/170/>.
- [14] Shane M. Walsh et al. "Demonstration of 100 Gbps coherent free-space optical communications at LEO tracking rates". In: *Scientific Reports* 12.1 (Oct. 31, 2022), p. 18345. DOI: 10.1038/s41598-022-22027-0.
- [15] David J. Geisler and Bryan Robinson. "Coherent Architectures for Free-Space Optical Communications". In: Conference on Lasers and Electro-Optics, Optical Society of America. San Jose, CA, May 2020. URL: <https://ntrs.nasa.gov/citations/20200006812>.

- [16] Hamid Hemmati and David Caplan. "Chapter 4 - Optical Satellite Communications". In: *Optical Fiber Telecommunications (Sixth Edition)*. Ed. by Ivan P. Kaminow, Tingye Li, and Alan E. Willner. Optics and Photonics. Boston: Academic Press, Jan. 1, 2013, pp. 121–162. DOI: 10.1016/B978-0-12-396960-6.00004-3.
- [17] Noelia Martinez. "Atmospheric Pre-Compensation of Ground-to-Space Communications with Adaptive Optics: Past, Present and Future—A Field Review". In: *Photonics* 10.7 (July 2023), p. 858. DOI: 10.3390/photonics10070858.
- [18] Mingbo Niu, Julian Cheng, and Jonathan F. "Terrestrial Coherent Free-Space Optical Communication Systems". In: *Optical Communication*. Ed. by Narottam Das. InTech, Oct. 3, 2012. DOI: 10.5772/48284.
- [19] Parmesh Kumar. "Comparative Analysis of BER Performance for Direct Detection and Coherent Detection FSO Communication Systems". In: *2015 Fifth International Conference on Communication Systems and Network Technologies*. Gwalior, India: IEEE, Apr. 2015, pp. 369–374. ISBN: 978-1-4799-1797-6. DOI: 10.1109/CSNT.2015.42.
- [20] Zabih Ghassemlooy, W. Popoola, and S. Rajbhandari. *Optical wireless communications: system and channel modelling with MATLAB*. Boca Raton, FL: CRC Press, 2013. ISBN: 978-1-4398-5235-4.
- [21] Mohammad Ali Khalighi and Murat Uysal. "Survey on Free Space Optical Communication: A Communication Theory Perspective". In: *IEEE Communications Surveys & Tutorials* 16.4 (2014), pp. 2231–2258. DOI: 10.1109/COMST.2014.2329501.
- [22] Keysight. *Everything You Need to Know About Coherent Optical Modulation*. Mar. 25, 2019. URL: <https://www.keysight.com/us/en/assets/7018-06114/application-notes/5992-2888.pdf>.
- [23] L. Kazovsky. "Balanced phase-locked loops for optical homodyne receivers: Performance analysis, design considerations, and laser linewidth requirements". In: *Journal of Lightwave Technology* 4.2 (Feb. 1986). Conference Name: Journal of Lightwave Technology, pp. 182–195. DOI: 10.1109/JLT.1986.1074698.
- [24] Zhensheng Jia and Luis Alberto Campos. *Coherent Optics for Access Networks*. Boca Raton, FL: CRC Press, Oct. 28, 2019. 122 pp. DOI: 10.1201/9780429284106.
- [25] Darli Augusto De Arruda Mello and Fabio Aparecido Barbosa. *Digital Coherent Optical Systems: Architecture and Algorithms*. Optical Networks. Cham: Springer International Publishing, 2021. DOI: 10.1007/978-3-030-66541-8.
- [26] B. D. Guenther and Duncan G. Steel, eds. *Encyclopedia of modern optics*. Second edition. OCLC: 1027706598. Amsterdam, the Netherlands: Elsevier, 2018. ISBN: 978-0-12-814982-9.
- [27] *Coherent Detection*. Fosco Connect. URL: <https://www.fiberoptics4sale.com/blogs/wave-optics/coherent-detection>.
- [28] *Phase-Modulated Optical Communication Systems*. 1st ed. New York: Springer-Verlag, 2005. ISBN: 978-0-387-24392-4. DOI: 10.1007/b135576.
- [29] Arun K. Majumdar and Jennifer C. Ricklin. *Free-Space Laser Communications: Principles and Advances*. New York, NY: Springer New York, 2008. DOI: 10.1007/978-0-387-28677-8.
- [30] Semjon Schaefer, Werner Rosenkranz, and Mark Gregory. "Comparison of homodyne and intradyne detection for high-order modulation schemes in optical intersatellite communication systems". In: *2015 IEEE International Conference on Space Optical Systems and Applications (ICSOS)*. Oct. 2015, pp. 1–5. DOI: 10.1109/ICSOS.2015.7425086.
- [31] Funan Zhu et al. "Inter-satellite laser-ranging based on intradyne coherent detection". In: *Applied Optics* 60.28 (Oct. 1, 2021). Publisher: Optica Publishing Group, pp. 8930–8938. DOI: 10.1364/AO.434807.
- [32] Isiaka Alimi et al. "A Review of Self-Coherent Optical Transceivers: Fundamental Issues, Recent Advances, and Research Directions". In: *Applied Sciences* 11.16 (Aug. 17, 2021), p. 7554. DOI: 10.3390/app11167554.

- [33] Nelson J. Muga et al. "Self-coherent optical detection for access and metro networks". In: *2019 21st International Conference on Transparent Optical Networks (ICTON)*. July 2019, pp. 1–4. DOI: 10.1109/ICTON.2019.8840560.
- [34] Mahdi Naghshvarianjahromi, Shiva Kumar, and M. Jamal Deen. "Free Space Ground to Satellite Optical Communications Using Kramers–Kronig Transceiver in the Presence of Atmospheric Turbulence". In: *Sensors* 22.9 (Jan. 2022). Publisher: Multidisciplinary Digital Publishing Institute, p. 3435. DOI: 10.3390/s22093435.
- [35] Yixiao Zhu et al. "Comparative study of cost-effective coherent and direct detection schemes for 100 Gb/s/λ PON". In: *Journal of Optical Communications and Networking* 12.9 (Sept. 1, 2020), p. D36. DOI: 10.1364/JOCN.390911.
- [36] Jasjot Kaur Sahota and Divya Dhawan. "Reducing the effect of scintillation in FSO system using coherent based homodyne detection". In: *Optik* 171 (Oct. 1, 2018), pp. 20–26. DOI: 10.1016/j.ijleo.2018.06.019.
- [37] Zixiong Wang, Wen-De Zhong, and Changyuan Yu. "Performance Improvement of OOK Free-Space Optical Communication Systems by Coherent Detection and Dynamic Decision Threshold in Atmospheric Turbulence Conditions". In: *IEEE Photonics Technology Letters* 24.22 (Nov. 2012), pp. 2035–2037. DOI: 10.1109/LPT.2012.2218652.
- [38] Etty J. Lee and Vincent W.S. Chan. "Diversity Coherent and Incoherent Receivers for Free-Space Optical Communication in the Presence and Absence of Interference". In: *Journal of Optical Communications and Networking* 1.5 (Oct. 1, 2009), p. 463. DOI: 10.1364/JOCN.1.000463.
- [39] Matthias Seimetz. *High-Order Modulation for Optical Fiber Transmission*. Vol. 143. Springer Series in Optical Sciences. Berlin, Heidelberg: Springer Berlin Heidelberg, 2009. DOI: 10.1007/978-3-540-93771-5.
- [40] Md. Yeakub Ali, Tamanna Hossain, and Md. Munjure Mowla. "A Trade-off between Energy and Spectral Efficiency in Massive MIMO 5G System". In: *2019 3rd International Conference on Electrical, Computer & Telecommunication Engineering (ICECTE)*. Dec. 2019, pp. 209–212. DOI: 10.1109/ICECTE48615.2019.9303551.
- [41] Ahmed Nabih Rashed and Mohammed Salah Tabbour. "The Trade Off Between Different Modulation Schemes for Maximum Long Reach High Data Transmission Capacity Optical Orthogonal Frequency Division Multiplexing (OOFDM)". In: *Wireless Personal Communications: An International Journal* 101.1 (July 1, 2018), pp. 325–337. DOI: 10.1007/s11277-018-5690-9.
- [42] Sonali Chauhan et al. "Performance Analysis and Enhancement of Free Space Optical Links for Developing State-of-the-Art Smart City Framework". In: *Photonics* 7.4 (Dec. 16, 2020), p. 132. DOI: 10.3390/photonics7040132.
- [43] Mathuranathan. *Performance comparison of Digital Modulation techniques*. GaussianWaves. Apr. 14, 2010. URL: <https://www.gaussianwaves.com/2010/04/performance-comparison-of-digital-modulation-techniques-2/>.
- [44] Mathuranathan Viswanathan. *Digital modulations using Python*. Place of publication not identified: Independently Published, 2019. ISBN: 978-1-71232-163-8.
- [45] A. K. M. Sharoar Jahan Choyon and Ruhin Chowdhury. "Performance Comparison of Free-Space Optical (FSO) Communication Link Under OOK, BPSK, DPSK, QPSK and 8-PSK Modulation Formats in the Presence of Strong Atmospheric Turbulence". In: *Journal of Optical Communications* 0.0 (Mar. 31, 2020). DOI: 10.1515/joc-2019-0250.
- [46] Tanuja Pande and Narendra Kumar Shukla. "Comparison among OOK, BPSK, DPSK, and QPSK with turbulence in FSO links". In: *Journal of Optical Communications* (May 5, 2023). DOI: 10.1515/joc-2021-0221.
- [47] Yan Li et al. "Performance analysis of OOK, BPSK, QPSK modulation schemes in uplink of ground-to-satellite laser communication system under atmospheric fluctuation". In: *Optics Communications* 317 (Apr. 2014), pp. 57–61. DOI: 10.1016/j.optcom.2013.12.032.
- [48] D. Anandkumar and R. G. Sangeetha. "A survey on performance enhancement in free space optical communication system through channel models and modulation techniques". In: *Optical and Quantum Electronics* 53.1 (Jan. 2021), p. 5. DOI: 10.1007/s11082-020-02629-6.

- [49] Samir Ahmed Al-Gailani et al. "A Survey of Free Space Optics (FSO) Communication Systems, Links, and Networks". In: *IEEE Access* 9 (2021), pp. 7353–7373. DOI: 10.1109/ACCESS.2020.3048049.
- [50] Joseph M. Kahn. "Modulation and Detection Techniques for Optical Communication Systems". In: *Optical Amplifiers and Their Applications*. Optica Publishing Group, June 25, 2006, CThC1. DOI: 10.1364/COTA.2006.CThC1.
- [51] Alberto Carrasco-Casado and Ramon Mata-Calvo. "Space Optical Links for Communication Networks". In: *Springer Handbook of Optical Networks*. Ed. by Biswanath Mukherjee et al. Springer Handbooks. Cham: Springer International Publishing, 2020, pp. 1057–1103. DOI: 10.1007/978-3-030-16250-4_34.
- [52] J. Panasiewicz et al. "All-Digital Optical Phase-Locked Loop for satellite communications under Turbulence Effects". In: 2022 IEEE International Topical Meeting on Microwave Photonics, MWP 2022 - Proceedings. 2022. DOI: 10.1109/MWP54208.2022.9997784.
- [53] Exail. *Introduction to Exail Modulator Bias Controller (MBC)*. June 2023. URL: <https://www.ixblue.com/wp-content/uploads/2022/01/Introduction%20To%20ixblue%20MBC%202019.pdf>.
- [54] Exail. *MBC-DG-LAB-A1 Datasheet*. Jan. 2023. URL: <https://www.ixblue.com/wp-content/uploads/2022/02/MBC-DG-LAB.pdf>.
- [55] Exail. *MODULATOR BIAS CONTROLLER MBC-DG-LAB USER MANUAL*. 2023. URL: https://www.ixblue.com/wp-content/uploads/2022/01/MBC-DG-LAB%20operating%20Manual%20v1.3_0.pdf.
- [56] Thorlabs. *Triplet Fiber Optic Collimators/Couplers*. 2025. URL: https://www.thorlabs.com/newgrouppage9.cfm?objectgroup_id=5124.
- [57] iXblue Photonics. *Electro-Optical Modulators Operating Manual*. Aug. 2, 2021. URL: https://www.ixblue.com/wp-content/uploads/2022/01/EOM%20operating%20Manual_ED0_27.pdf.
- [58] Rajkumar Nagarajan. "Technique for measuring the Vpi-AC of a mach-zehnder modulator". Pat. 6204954. Nortel Networks Limited (Montreal CA). Mar. 20, 2001. URL: <https://patents.google.com/patent/US6204954B1/en>.
- [59] A.H Gnauck and Peter J. Winzer. "Optical phase-shift-keyed transmission". In: *Journal of Light-wave Technology* 23.1 (Jan. 2005), pp. 115–130. DOI: 10.1109/JLT.2004.840357.
- [60] William K. Pratt. *Laser communication systems*. Wiley series in pure and applied optics. New York: Wiley, 1969. 271 pp. ISBN: 978-0-471-69650-6.
- [61] Fan Yang, Flavien Gyger, and Luc Thévenaz. "Giant Brillouin amplification in gas using hollow-core waveguides". In: (2019). DOI: 10.48550/ARXIV.1911.04430.
- [62] Eugene Hecht. *Optics*. 5 ed/fifth edition, global edition. Harlow England: Pearson, 2017. 722 pp. ISBN: 978-1-292-09693-3.
- [63] Yobani Mejía-Barbosa. *Fundamentals of optics: an introductory course*. Bellingham, Washington, USA : Bogota, Colombia: SPIE ; Universidad Nacional de Colombia, 2023. 312 pp. ISBN: 978-1-5106-5780-9.



Derivations and Calculations

A.1. Photodetector current calculation

Consider the electric fields for the modulated and LO signal:

$$E_s(t) = \sqrt{2P_s} A_s(t) \cos(\omega_s t + \theta_s(t)) \quad (\text{A.1})$$

$$E_l(t) = \sqrt{2P_l} \cos(\omega_l t + \theta_l(t)) \quad (\text{A.2})$$

where A, P, ω, θ are the amplitude, power, angular frequency, and phase with subscripts s and l to indicate the carrier signal and LO respectively. For each of the signals, it is assumed that both fields are copolarized and aligned perpendicularly to the photodetector surface. [20, 26, 27, 60] By combining them, the signal intensity $S(t)$ becomes:

$$\begin{aligned} S(t) &= (E_s(t) + E_l(t))^2 \\ S(t) &= 2P_s A_s^2(t) \cos^2(\omega_s t + \theta_s(t)) + 2P_l \cos^2(\omega_l t + \theta_l(t)) \\ &\quad + 2\sqrt{4P_s P_l} A_s(t) \cos(\omega_s t + \theta_s(t)) \cos(\omega_l t + \theta_l(t)) \end{aligned} \quad (\text{A.3})$$

Using the product-to-sum identity (A.4) gives the Equation A.5 for $S(t)$

$$\cos(x) \cos(y) = [\cos(x+y) + \cos(x-y)] / 2 \quad (\text{A.4})$$

$$\begin{aligned} S(t) &= 2P_s A_s^2(t) \cos^2(\omega_s t + \theta_s(t)) + 2P_l \cos^2(\omega_l t + \theta_l(t)) \\ &\quad + 2\sqrt{P_s P_l} A_s(t) \cos\{(\omega_s - \omega_l)t + \theta_s(t) - \theta_l(t)\} \\ &\quad + 2\sqrt{P_s P_l} A_s(t) \cos\{(\omega_s + \omega_l)t + \theta_s(t) + \theta_l(t)\} \end{aligned} \quad (\text{A.5})$$

The time average is denoted as $\langle \cdot \rangle$ and is defined below

$$\langle f(t) \rangle = \frac{1}{T} \int_0^T f(t) dt \quad \text{where } T = \frac{2\pi}{\omega} \quad (\text{A.6})$$

Computing the the time average of the first 2 terms is done with relation A.7

$$\begin{aligned} a(t) &= A \cos(\omega t + \alpha) \\ \langle a(t)^2 \rangle &= \frac{1}{T} \int_0^T A^2 \cos^2(\omega t + \alpha) dt = \frac{A^2}{2} \end{aligned} \quad (\text{A.7})$$

Applying this to $S(t)$ gives:

$$\langle S(t) \rangle = P_s A_s^2(t) + P_l + \langle 3\text{rd term} \rangle + \langle 4\text{th term} \rangle \quad (\text{A.8})$$

The relation for the photodetector current is:

$$i_p(t) = \mathcal{R}\langle S(t) \rangle \quad (\text{A.9})$$

In the case of a homodyne scheme, $\omega_s = \omega_l$ and gives the following equation:

$$i_p(t) = \mathcal{R} \left[P_s A_s^2 + P_l + \langle 2\sqrt{P_s P_l} A_s \cos \{ \theta_s - \theta_l \} \rangle + \langle 2\sqrt{P_s P_l} A_s \cos \{ 2\omega_s t + \theta_s + \theta_l \} \rangle \right] \quad (\text{A.10})$$

The 4th term is filtered out ([20]) and so the final photodetector current for a homodyne detector is:

$$i_p(t) = \mathcal{R} \left[P_s A_s^2 + P_l + 2\sqrt{P_s P_l} A_s \cos \{ \theta_s(t) - \theta_l(t) \} \right] \quad (\text{A.11})$$

For heterodyne detection, the IF filter only lets through the 3rd term and suppresses the others. Furthermore the amplitude of the third term is considered as constant due to the short duration over which the time average is taken. [20, 60] This gives the following photodetector current for heterodyne detection:

$$i_p(t) = \mathcal{R} \left[2\sqrt{P_s P_l} A_s \cos \{ (\omega_s - \omega_l)t + \theta_s(t) - \theta_l(t) \} \right] \quad (\text{A.12})$$

A.2. Incorrect half-wave voltage example calculation

The power transfer function for OOK (biased at the quadrature point) is:

$$P_{out}(t) = P_0 \cdot \left[\cos \left(\frac{\pi}{4} + \frac{\pi V(t)}{2V_\pi} \right) \right]^2 \quad (\text{A.13})$$

For OOK the amplitude of the signal should be $\pm 3.2/2$ [V]. Entering that into the power transfer function yields a minimum normalized power of 0.0153 and a maximum power of 0.9847. This means a power difference of 0.969, which in the ideal case is 1.0 .

For DPSK, suppose that we have two plane waves E_1 and E_2 , with phase ϕ_1, ϕ_2 and amplitudes A_1 , A_2 . The amplitude of the interfered wave is:

$$A_{1+2} = \sqrt{A_1^2 + A_2^2 + 2A_1 A_2 \cos(\phi_2 - \phi_1)} \quad (\text{A.14})$$

The phase when using the correct V_π is from 0° to 180° . When using the amplitude of ± 3.2 [V] instead of ± 3.8 [V], the phase becomes:

$$\phi_1 = \frac{3.8 - 3.2}{2 \cdot 3.8} \cdot 180^\circ = 14.2^\circ, \quad \phi_2 = 180 - \phi_1 = 165.8^\circ$$

For these phases, the amplitude of the wave is:

$$A = \cos \left(\frac{\phi}{180} \cdot \pi \right) = \pm 0.97 \quad (\text{A.15})$$

Assuming the ideal scenario where $A_1 = A_2$, and setting $A_1 = 1$, the amplitude of the interfered wave becomes:

$$A_{1+2} = \sqrt{0.97^2 + 2(0.97)^2 \cos(165.8 - 14.2)} = 0.476 \quad (\text{A.16})$$

When $\phi_1 = \phi_2$, the amplitude is:

$$A_{1+2} = 2A_1 = 1.94 \quad (\text{A.17})$$

Setting the power of waves E_1, E_2 to be P_0 , the power of the destructive wave is $0.223P_0$ and $3.76P_0$ for the constructive interference. Again in the ideal case, this would be 0 and $4P_0$. This means that the new power difference between constructive and destructive interference is 88% of the original, or a 12% loss.

A.3. Modulation Transfer Function

For a single waveguide across which a voltage is applied, the phase delay that is induced can be described as follows:

$$\phi(t) = \frac{\pi V(t)}{V_\pi} \quad (\text{A.18})$$

For a voltage of $V = V_\pi$, a π phase difference is created. The output electric field with the phase delay is given below:

$$E_{out} = E_{in} \cdot e^{j\phi(t)} = E_{in} \cdot \exp\left(j \frac{\pi V(t)}{V_\pi}\right) \quad (\text{A.19})$$

For an intensity modulator using two waveguides, a simplified schematic can be seen in Figure A.1.

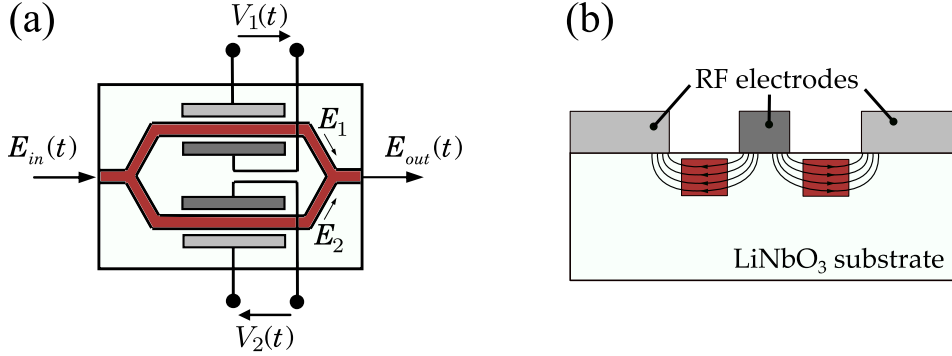


Figure A.1: Schematic representation of the MZM. (a) Top view of the MZM with a simplified view of the electrodes. The waveguides are colored red. (b) Cross section of the MZM, where the electric field through the waveguides has been visualized for a positive voltage on the center electrode. Adapted from: [39, p. 18] and [61, S. 15].

The output electric field of each arm can be described using the following equation.

$$E_1 = \frac{E_{in}}{\sqrt{2}} e^{j\theta_1}, \quad E_2 = \frac{E_{in}}{\sqrt{2}} e^{j\theta_2} \quad (\text{A.20})$$

Subsequently, the output electric field becomes:

$$E_{out} = \frac{1}{\sqrt{2}} (E_1 + E_2) = \frac{E_{in}}{2} (e^{j\phi_1} + e^{j\phi_2}) \quad (\text{A.21})$$

Writing it in terms of the phase difference gives the following:

$$E_{out} = \frac{E_{in}}{2} \cdot \exp\left(j \frac{\phi_1 + \phi_2}{2}\right) \cdot \left[\exp\left(j \frac{\phi_1 - \phi_2}{2}\right) + \exp\left(j \frac{-(\phi_1 - \phi_2)}{2}\right) \right] \quad (\text{A.22})$$

Simplifying using the cosine function to represent the exponential terms:

$$E_{out} = E_{in} \cdot \exp\left(j \frac{\phi_1 + \phi_2}{2}\right) \cdot \cos\left(\frac{\phi_1 - \phi_2}{2}\right) \quad (\text{A.23})$$

Because of the configuration of the MZM, the voltage is applied in the middle of the two arms (center electrode), resulting in a push pull configuration where $V(t) = V_1 = -V_2$ and thus $\phi_1 = -\phi_2$. For a Mach-Zehnder Modulator, the half-wave voltage or V_π is defined as the voltage needed to induce a ϕ phase difference *between* the two arms. In other words, the voltage required to go from constructive to destructive interference (and vice versa). Assuming the phase in each arm is written as follows, with unknown variable x that represents the half-wave voltage for a single phase modulator, we get:

$$\phi_1 = \frac{\pi \cdot V(t)}{x} \quad \phi_2 = \frac{\pi \cdot -V(t)}{x}, \quad V(t) = V_\pi \rightarrow \phi_1 = \frac{\pi \cdot V_\pi}{x} \quad \phi_2 = \frac{\pi \cdot -V_\pi}{x} \quad (\text{A.24})$$

Then using the definition of V_π for an intensity modulator we can determine the variable x :

$$\Delta\phi = \phi_1 - \phi_2 = \frac{2V_\pi \cdot \pi}{x} = \pi \rightarrow x = 2V_\pi \quad (\text{A.25})$$

This gives the following relation between the phase delay on each arm and the voltage that is applied:

$$\phi_1 = \frac{\pi \cdot V(t)}{2V_\pi} \quad \phi_2 = \frac{\pi \cdot -V(t)}{2V_\pi} \quad (\text{A.26})$$

Comparing these phase delays to Equation A.18, it becomes clear that the half-wave voltage V_π for an intensity modulator is half of that for the single phase modulator. This results in the following equation for the output electric field of the MZM:

$$E_{out} = E_{in} \cos(\phi_1) = E_{in} \cos\left(\frac{\pi V(t)}{2V_\pi}\right) \quad (\text{A.27})$$

The power at time t is derived from the Poynting vector for a plane wave, and results in the electric field squared:

$$P_{out}(t) = P_0 \left[\cos\left(\frac{\pi V(t)}{2V_\pi}\right) \right]^2 \quad (\text{A.28})$$

In reality, we have two different voltages: a DC bias and an RF voltage signal. This changes the equation to the following:

$$P_{out}(t) = P_0 [\cos(\phi_{bias} + \phi_{RF})]^2 = P_0 \left[\cos\left(\phi_{bias} + \frac{\pi V(t)}{2V_\pi}\right) \right]^2 \quad (\text{A.29})$$

where the bias phase shift is:

$$\phi_{bias} = \frac{\pi V_{DC}}{2V_{\pi,DC}} + \phi_0 \quad (\text{A.30})$$

A.4. Coherence length

The coherence time is defined as *"the temporal interval over which we can reasonably predict the phase of the lightwave at a given point in space."* [62, p. 588]. The term 'coherence length' refers to the length this time represents in space, and relates to *temporal coherence*, not spatial coherence. The coherence time/length depends on the emission spectrum of a laser source. For this laser, the linewidth is given to be $\Delta\nu < 0.1$ [kHz]. The linewidth $\Delta\nu$ is the spectral range that corresponds to the full width at half maximum (FWHM). Considering the two frequencies at the edge of this range ν_1, ν_2 , the interference of these two frequencies is:

$$E(t) = E_1(t) + E_2(t) = A \cos(2\pi\nu_1 t) + A \cos(2\pi\nu_2 t) \quad (\text{A.31})$$

This can also be written as the multiplication of two periodic terms:

$$E(t) = 2A \cos\left(2\pi \frac{\nu_1 + \nu_2}{2} t\right) \cos\left(2\pi \frac{\nu_1 - \nu_2}{2} t\right) \quad (\text{A.32})$$

The first cosine term describes the carrier frequency of this wave, which is equivalent to the center frequency ν_0 if the spectral distribution is symmetric. The second term is the modulation envelope. At points of constructive interference, the phase of both waves is equal. The period of this second term describes the time (or length) between the constructive (or destructive) points. The coherence length can thus be calculated as follows:

$$L_c = \frac{c}{n\Delta\nu} \approx \frac{3 \cdot 10^8}{1 \cdot 100} = 3000 \text{ [km]} \quad (\text{A.33})$$

As long as the total length (or time) of the communication link is smaller than the coherence length, the phase can still be predicted accurately.

A.5. Modulator bias and half-wave voltage determination

In section 3.1 a method ([58]) was used to determine the half-wave voltage. This method works by comparing the average output power between a sinusoidal input signal and no input signal. One essential condition is that the modulator is biased at the maximum point during operation. The patent describes that this can be verified by observing that the odd harmonics in the spectrum of the output signal disappear. However, no explanation is given as to why this is true. Therefore, this section will deal with the derivations showing why the odd harmonics disappear when the modulator is biased at the maximum point.

The input signal is described in Equation A.34, where V_0 is the amplitude of the signal and f is the frequency of the signal.

$$V(t) = V_0 \cos(2\pi ft) \quad (\text{A.34})$$

The average power is found by substituting this voltage signal into the power transfer function when biased at the maximum point, and is integrated over the duration of one period. The average power for an input signal ($P_{avg}(\text{On})$) and without input signal ($P_{avg}(\text{Off})$) can be seen in the equation below. Using both powers allows for the calculation of V_π to be performed.

$$\begin{aligned} P_{avg}(\text{On}) &= P_0 \cdot \frac{1}{T} \int_0^T \left[\cos \left(\frac{\pi}{2V_\pi} V_0 \cos(2\pi ft) \right) \right]^2 dt \\ P_{avg}(\text{Off}) &= P_0 \cdot \frac{1}{T} \int_0^T [\cos(0)]^2 dt = P_0 \\ \frac{P_{avg}(\text{On})}{P_{avg}(\text{Off})} &= \frac{1}{T} \int_0^T \left[\cos \left(\frac{\pi}{2V_\pi} V_0 \cos(2\pi ft) \right) \right]^2 dt \end{aligned} \quad (\text{A.35})$$

These equations are only true when the modulator is biased at the maximum point. As stated earlier, when this is the case, the spectrum of the output signal $P_{avg}(\text{On})$ should only show the remaining even harmonics. To show why this is the case, the Fourier transform of the power transfer function needs to be derived. Consider the general equation for the output power:

$$P(t) = P_0 \left[\cos \left(\phi_{bias} + \frac{\pi}{2V_\pi} V_0 \cos(2\pi ft) \right) \right]^2 = \frac{P_0}{2} \left[1 + \cos \left(2\phi_{bias} + \frac{\pi V_0}{V_\pi} \cos(2\pi ft) \right) \right] \quad (\text{A.36})$$

This equation can be simplified to the following form:

$$x(t) = \cos(a + b \cos(2\pi ft)) \quad (\text{A.37})$$

Using the angle sum identity, this can be split up into two terms:

$$x(t) = \cos(a) \cdot \cos(b \cos(2\pi ft)) - \sin(a) \cdot \sin(b \cos(2\pi ft)) \quad (\text{A.38})$$

The terms $\cos(\cos(t))$ and $\sin(\sin(t))$ do not have a closed-form Fourier transform, so they need to be represented as an infinite sum, which is done using the Jacobi-Anger Expansion:

$$\begin{aligned} \cos(z \cos \theta) &\equiv J_0(z) + 2 \sum_{n=1}^{\infty} (-1)^n J_{2n}(z) \cos(2n\theta) \\ \sin(z \sin \theta) &\equiv 2 \sum_{n=1}^{\infty} J_{2n-1}(z) \sin[(2n-1)\theta] \end{aligned} \quad (\text{A.39})$$

Here $J_n(z)$ represents the n -th Bessel function of the first kind, shown in Equation A.40.

$$J_n(z) = \sum_{m=0}^{\infty} \frac{(-1)^m}{m! \Gamma(m+n+1)} \left(\frac{z}{2} \right)^{2m+n} \quad (\text{A.40})$$

Performing this expansion results in Equation A.41.

$$\begin{aligned}
 x(t) &= \cos(a) \cdot \alpha(t) - \sin(a) \cdot \beta(t) \\
 A(t) &= \cos(b \cos(2\pi ft)) = J_0(b) + 2 \sum_{n=1}^{\infty} (-1)^n J_{2n}(b) \cos(2n \cdot 2\pi ft) \\
 B(t) &= \sin(b \cos(2\pi ft)) = -2 \sum_{n=1}^{\infty} (-1)^n J_{2n-1}(b) \cos((2n-1) \cdot 2\pi ft)
 \end{aligned} \tag{A.41}$$

The final Fourier transform of $x(t)$ is obtained by applying the definition found in Equation A.42 along with the closed-form transforms in Equation A.43. The result is illustrated in Equation A.44.

$$x(t) \xleftrightarrow{\mathcal{F}} X(\xi) \quad X(\xi) = \int_{-\infty}^{\infty} x(t) e^{-j2\pi\xi t} dt \tag{A.42}$$

$$\begin{aligned}
 \mathcal{F}[\cos(kt)] &= \frac{1}{2} \left[\delta\left(\xi - \frac{k}{2\pi}\right) + \delta\left(\xi + \frac{k}{2\pi}\right) \right] \\
 \mathcal{F}[C] &= C \cdot \delta(\xi)
 \end{aligned} \tag{A.43}$$

$$\begin{aligned}
 \mathcal{F}[x(t)] &= X(\xi) = \cos(a) \cdot \mathcal{F}[A(t)] - \sin(a) \cdot \mathcal{F}[B(t)] \\
 \mathcal{F}[A(t)] &= J_0(b)\delta(\xi) + 2 \sum_{n=1}^{\infty} (-1)^n J_{2n}(b) \cdot \frac{1}{2} [\delta(\xi - 2nf) + \delta(\xi + 2nf)] \\
 \mathcal{F}[B(t)] &= -2 \sum_{n=1}^{\infty} (-1)^n J_{2n-1}(b) \cdot \frac{1}{2} [\delta(\xi - (2n-1)f) + \delta(\xi + (2n-1)f)]
 \end{aligned} \tag{A.44}$$

Combining all terms, obtaining the magnitude spectrum and including only the positive frequencies results in Equation A.45.

$$\begin{aligned}
 |X(\xi)| &= \cos(a) \cdot \left[J_0(b)\delta(\xi) + \sum_{n=1}^{\infty} J_{2n}(b) \cdot \delta(\xi - 2nf) \right] \\
 &\quad - \sin(a) \cdot \left[- \sum_{n=1}^{\infty} J_{2n-1}(b) \cdot \delta(\xi - (2n-1)f) \right]
 \end{aligned} \tag{A.45}$$

This result can now be used to describe the Fourier spectrum of the original function $P(t)$. Using the substitutions in Equation A.46, the final Fourier transform is shown in Equation A.47.

$$a = 2\phi_{bias}, \quad b = \frac{\pi V_0}{V_\pi} \tag{A.46}$$

$$\begin{aligned}
 |\mathcal{F}[P(t)]| &= \frac{1}{2} P_0 \delta(\xi) + \frac{1}{2} P_0 \cdot \cos(2\phi_{bias}) \cdot \left[J_0\left(\frac{\pi V_0}{V_\pi}\right) \delta(\xi) + \sum_{n=1}^{\infty} J_{2n}\left(\frac{\pi V_0}{V_\pi}\right) \cdot \delta(\xi - 2nf) \right] \\
 &\quad + \frac{1}{2} P_0 \cdot \sin(2\phi_{bias}) \cdot \sum_{n=1}^{\infty} J_{2n-1}\left(\frac{\pi V_0}{V_\pi}\right) \cdot \delta(\xi - (2n-1)f)
 \end{aligned} \tag{A.47}$$

Examining Equation A.47, the even harmonics are represented by the term $\delta(\xi - 2nf)$, while the odd harmonics are represented by the term $\delta(\xi - (2n-1)f)$. The magnitude of these terms is dependent on ϕ_{bias} . Biasing the modulator at the maximum point is achieved when $\phi_{bias} = 0$. As $\phi_{bias} \rightarrow 0$ we find that $\cos(2\phi_{bias}) \rightarrow 1$ and $\sin(2\phi_{bias}) \rightarrow 0$. Analyzing the equation, it can be seen that this reduces the magnitude of the odd harmonics to 0, while retaining the full magnitude of the even harmonics. To illustrate a best-case scenario of the spectrum (with $\phi_{bias} = 0$) see Figure A.2. The first harmonic at 25 [MHz] disappears completely, and the third harmonic (75 [MHz]) is minimally present.

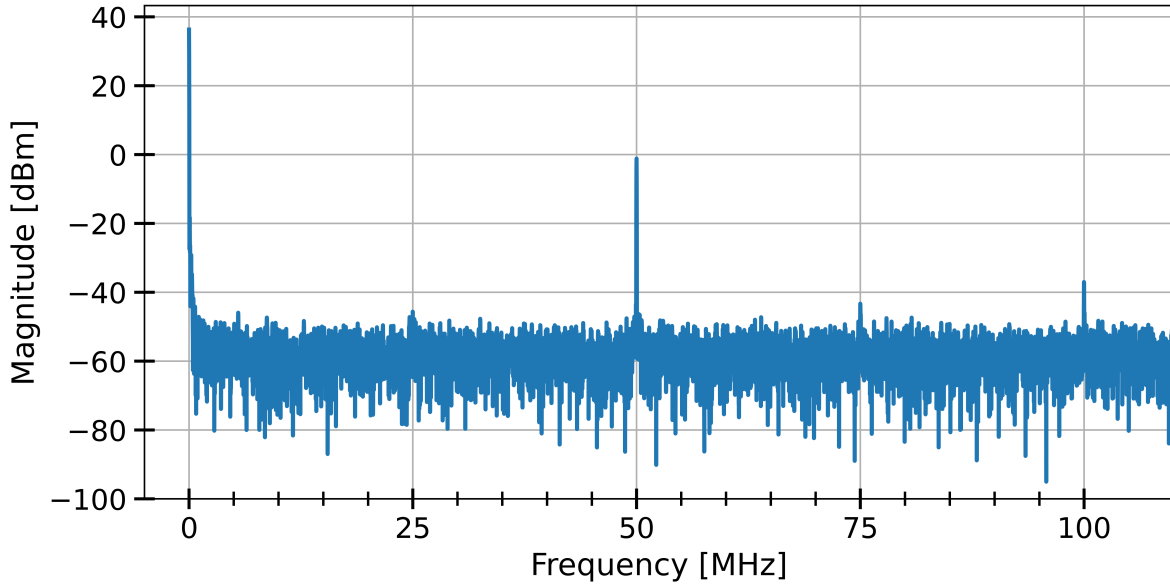


Figure A.2: Magnitude spectrum of the photodetector voltage for an input sine-wave with an amplitude of 1.0 [V] and a frequency of 25 [MHz] when perfectly biased at the maximum point. With this bias point, the odd harmonics (25, 75 [MHz]) disappear, while the even harmonics (50, 100 [MHz]) are kept. For this plot a 50 [Ω] reference is used.

Using this method, the half-wave voltage V_π was determined at a number of frequencies, and can be seen in Figure 3.5. To quantify the uncertainty for the final V_π value, the error for each measured power was converted into the total uncertainty on the power ratio. The standard deviation of the power ratio is computed using Equation A.48. The average power for the input signal 'on' and 'off' are independent variables, and allow the use of the following propagation of uncertainty equation. $P_{avg}(\text{Off})$ and $P_{avg}(\text{On})$ are denoted in short as P_{Off} , P_{On} respectively.

$$\psi = \frac{P_{\text{On}}}{P_{\text{Off}}} \rightarrow \sigma_\psi \approx |\psi| \sqrt{\left(\frac{\sigma_{P_{\text{On}}}}{P_{\text{On}}}\right)^2 + \left(\frac{\sigma_{P_{\text{Off}}}}{P_{\text{Off}}}\right)^2} \quad (\text{A.48})$$

Using this standard deviation, the uncertainty on the V_π is calculated by using the upper and lower value for the power ratio as seen in the equation below.

$$[\psi + \sigma_\psi, \psi - \sigma_\psi] \quad (\text{A.49})$$

B

Gaussian Beam Parameters and Simulation

The light coming out of the fiber (and collimator) is a Gaussian beam and can be described mathematically using Equation B.1.

$$\mathbf{E}(\mathbf{r}, t) = \hat{\mathbf{e}} E_0 \frac{w_0}{w(\mathbf{r} \cdot \hat{\mathbf{k}})} \exp\left(-\frac{\rho^2}{w^2(\mathbf{r} \cdot \hat{\mathbf{k}})}\right) \exp\left[j\left(k\mathbf{r} \cdot \hat{\mathbf{k}} - \omega t + \frac{k\rho^2}{2R(\mathbf{r} \cdot \hat{\mathbf{k}})} + \zeta(\mathbf{r} \cdot \hat{\mathbf{k}})\right)\right] \quad (\text{B.1})$$

where

- $\hat{\mathbf{e}}$ is the unit polarization vector.
- E_0 is the amplitude of the field.
- \mathbf{r} is the position vector $[x \ y \ z]^T$
- $\hat{\mathbf{k}}$ is the propagation direction unit vector and k is the wavenumber $\frac{2\pi}{\lambda}$
- $\mathbf{r} \cdot \hat{\mathbf{k}}$ represents the projection of the position vector along the direction of propagation.
- $w(\mathbf{r} \cdot \hat{\mathbf{k}})$ is the radius of the beam evaluated at the point $\mathbf{r} \cdot \hat{\mathbf{k}}$ and w_0 is the beam waist.
- ρ is the radial distance from the beam axis and is equal to: $\rho = |\mathbf{r} - (\mathbf{r} \cdot \hat{\mathbf{k}})\hat{\mathbf{k}}|$
- $R(\mathbf{r} \cdot \hat{\mathbf{k}})$ is the radius of curvature of the phase front at the point $\mathbf{r} \cdot \hat{\mathbf{k}}$.
- $\zeta(\mathbf{r} \cdot \hat{\mathbf{k}})$ is the Gouy phase.

Simulating the interference of Gaussian beams requires knowledge about the beam waist and beam radius at a given point in space. Using the IR camera, the divergence/beam radius and the amplitude of the Gaussian spots were determined separately for the fixed and delayed beam. Subsequently, the IR camera was placed at several distances to find the approximate beam waist w_0 . The true location of the beam waist (z_0) could not be accurately determined and therefore the equations that describe the radius of curvature R were not used. Instead, the radius of curvature was estimated on the basis of the real interference spots. The Gaussian beam parameters have been summarized in Table B.1.

Table B.1: Gaussian beam parameters used to generate Figure 3.6.

Description	Symbol	Value
Beam radius for fixed beam	w_1	0.72 [mm]
Beam radius for delayed beam	w_2	0.95 [mm]
Beam waist	w_0	0.64 [mm]
Radius of curvature for at z_1	R_1	-2 [m]
Radius of curvature for at z_2	R_2	2 [m]
Amplitude for fixed beam	E_{01}^2	1
Amplitude of delayed beam	E_{02}^2	0.678

To produce the interference fringes seen in Figure 3.8, the delayed beam must be rotated with the two angles θ and φ . This is done with the rotation matrices shown in Equation B.2.

$$\mathbf{R}_y(\theta) = \begin{bmatrix} \cos \theta & 0 & \sin \theta \\ 0 & 1 & 0 \\ -\sin \theta & 0 & \cos \theta \end{bmatrix}, \quad \mathbf{R}_x(\varphi) = \begin{bmatrix} 1 & 0 & 0 \\ 0 & \cos \varphi & -\sin \varphi \\ 0 & \sin \varphi & \cos \varphi \end{bmatrix} \longrightarrow \mathbf{R} = \mathbf{R}_x(\varphi)\mathbf{R}_y(\theta) \quad (\text{B.2})$$

This creates a new rotated coordinate system (x', y', z') which is expressed in Equation B.3.

$$\begin{aligned} x' &= x \cos \theta + z \sin \theta \\ y' &= x \sin \varphi \sin \theta + y \cos \varphi - z \sin \varphi \cos \theta \\ z' &= -x \cos \varphi \sin \theta + y \sin \varphi + z \cos \varphi \cos \theta \end{aligned} \quad (\text{B.3})$$

Using this convention, the fixed beam (\mathbf{E}_1) and the delayed beam (\mathbf{E}_2) are represented in Equation B.4.

$$\begin{aligned} \mathbf{E}_1(\mathbf{r}, t) &= \hat{\mathbf{e}}_1 E_{01} \frac{w_0}{w(\mathbf{r} \cdot \hat{\mathbf{k}}_1)} \exp\left(-\frac{\rho_1^2}{w^2(\mathbf{r} \cdot \hat{\mathbf{k}}_1)}\right) \exp\left[j\left(k\mathbf{r} \cdot \hat{\mathbf{k}}_1 - \omega t + \frac{k\rho_1^2}{2R(\mathbf{r} \cdot \hat{\mathbf{k}}_1)}\right)\right] \\ \mathbf{E}_2(\mathbf{r}', t) &= \hat{\mathbf{e}}_2 E_{02} \frac{w_0}{w(\mathbf{r}' \cdot \hat{\mathbf{k}}_2)} \exp\left(-\frac{\rho_2^2}{w^2(\mathbf{r}' \cdot \hat{\mathbf{k}}_2)}\right) \exp\left[j\left(k\mathbf{r}' \cdot \hat{\mathbf{k}}_2 - \omega t + \frac{k\rho_2^2}{2R(\mathbf{r}' \cdot \hat{\mathbf{k}}_2)}\right)\right] \end{aligned} \quad (\text{B.4})$$

Some simplifications can be made. First, the way the coordinate system was defined in Figure 3.7, means that the fixed beam's propagation axis is coincident with the z-axis.¹ The polarization of the beam is assumed to be along the x-axis. This results in the following equation:

$$\begin{aligned} \mathbf{r} &= [x \ y \ z]^T & \hat{\mathbf{e}}_1 &= \hat{\mathbf{x}} & \hat{\mathbf{k}}_1 &= \hat{\mathbf{z}} & \mathbf{r} \cdot \hat{\mathbf{k}}_1 &= z & \rho_1^2 &= x^2 + y^2 \\ \mathbf{r}' &= [x' \ y' \ z']^T & \hat{\mathbf{e}}_2 &= \hat{\mathbf{x}}' & \hat{\mathbf{k}}_2 &= \hat{\mathbf{z}}' & \mathbf{r} \cdot \hat{\mathbf{k}}_2 &= z' & \rho_2^2 &= (x')^2 + (y')^2 \end{aligned} \quad (\text{B.5})$$

The interference produced by two electric fields is the superposition of both fields and is shown in Equation B.6

$$\mathbf{E}(\mathbf{r}, t) = \mathbf{E}_1(\mathbf{r}, t) + \mathbf{E}_2(\mathbf{r}, t) \quad (\text{B.6})$$

The irradiance (or intensity) produced by the two fields is described in Equation B.7. [63, p. 157]

$$I(\mathbf{r}) = \frac{\varepsilon_0 c}{2} \langle \mathbf{E}_1 \cdot \mathbf{E}_1^* + \mathbf{E}_2 \cdot \mathbf{E}_2^* + 2 \operatorname{Re} \{ \mathbf{E}_1 \cdot \mathbf{E}_2^* \} \rangle \quad (\text{B.7})$$

where ε_0 is the electric constant, c is the speed of light, $\langle \cdot \rangle$ is the time average (see Equation A.6), \mathbf{E}^* is the complex conjugate of \mathbf{E} and $\operatorname{Re}\{\cdot\}$ denotes the real part.

¹In actuality the beam is traveling in the direction towards the origin, so $\hat{\mathbf{k}}_1$ should be $-\hat{\mathbf{z}}$. But it is ignored here for ease of explanation.

This expression can be simplified further by assuming that the polarization of each beam is the same. For small angles of θ and φ , this can be done:

$$\hat{\mathbf{x}} \cdot \hat{\mathbf{x}}' = \cos(\theta) \approx 1 \quad (\text{B.8})$$

The irradiance can thus be written as follows:

$$I(\mathbf{r}) = \frac{\varepsilon_0 c}{2} \left(I_1(\mathbf{r}) + I_2(\mathbf{r}) + 2\sqrt{I_1(\mathbf{r})I_2(\mathbf{r})} \cos(\delta) \right) \quad (\text{B.9})$$

where δ is the phase difference between \mathbf{E}_1 and \mathbf{E}_2 . Each term is expressed in Equation B.10.

$$\begin{aligned} I_1(x, y, z) &= E_{01}^2 \left(\frac{w_0}{w(z)} \right)^2 \exp\left(-\frac{2(x^2 + y^2)}{w(z)^2} \right) \\ I_2(x, y, z) &= E_{02}^2 \left(\frac{w_0}{w(z')} \right)^2 \exp\left(-\frac{2((x')^2 + (y')^2)}{w(z')^2} \right) \\ \delta(x, y, z) &= k(z - z') + k \left(\frac{x^2 + y^2}{2R(z)} + \frac{(x')^2 + (y')^2}{2R(z')} \right) \end{aligned} \quad (\text{B.10})$$

Lastly, irradiance is evaluated in the XY plane, so $z = 0$. This gives the final expression for each term in the equation below.

$$\begin{aligned} I_1(x, y) &= E_{01}^2 \left(\frac{w_0}{w_1} \right)^2 \exp\left(-\frac{2(x^2 + y^2)}{w_1^2} \right) \\ I_2(x, y) &= E_{02}^2 \left(\frac{w_0}{w_2} \right)^2 \exp\left(-\frac{2((x')^2 + (y')^2)}{w_2^2} \right) \\ \delta(x, y) &= k \cdot -z' + k \left(\frac{x^2 + y^2}{2R_1} + \frac{(x')^2 + (y')^2}{2R_2} \right) \end{aligned} \quad (\text{B.11})$$

The orientation of the fringes can be found by projecting the plane that $\hat{\mathbf{k}}_1$ and $\hat{\mathbf{k}}_2$ share onto the XY plane. This can be seen in Figure B.1. The vectors and angles in the figure are expressed in the equations below:

$$\mathbf{n} = \hat{\mathbf{z}}' \times \hat{\mathbf{z}} = [\sin(\varphi) \quad \cos(\varphi) \sin(\theta) \quad 0]^T \quad (\text{B.12})$$

$$\mathbf{m} = \hat{\mathbf{z}} \times \mathbf{n} = [-\cos(\varphi) \sin(\theta) \quad \sin(\varphi) \quad 0]^T \quad (\text{B.13})$$

$$\tan(\beta) = \frac{\cos(\varphi) \sin(\theta)}{\sin(\varphi)} \quad (\text{B.14})$$

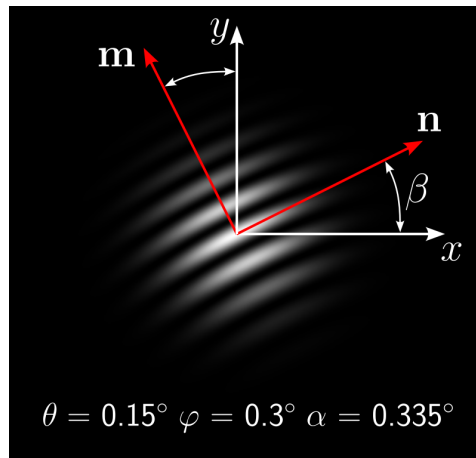


Figure B.1: Fringes produced by the interference of two Gaussian beams, where one beam is rotated by two angles θ, φ . The direction of the fringes can be found with the vectors \mathbf{n} and \mathbf{m} .

In addition to the simulation, some additional images are shown that contain the interference pattern of the spot for two phase differences. For roughly 200° and 210° , the interference pattern can be seen in Figure B.2.

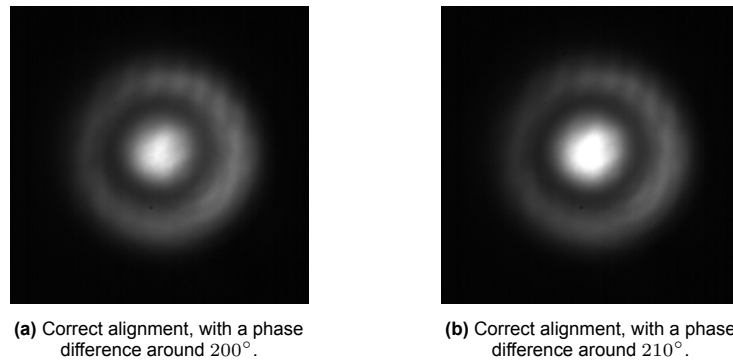


Figure B.2: Interference image of the fixed and delayed beam, captured with an infrared camera. Figures B.2a and B.2b show the correctly aligned spot, each with a different phase difference. The rings present in these spots occur around the destructive interference point. For reference, see Figure 3.6.

Because the divergence and subsequently the amplitude at the center are not the same for both beams, their interference is not efficient. In Figure B.3 the result of having the same divergence and power can be seen.

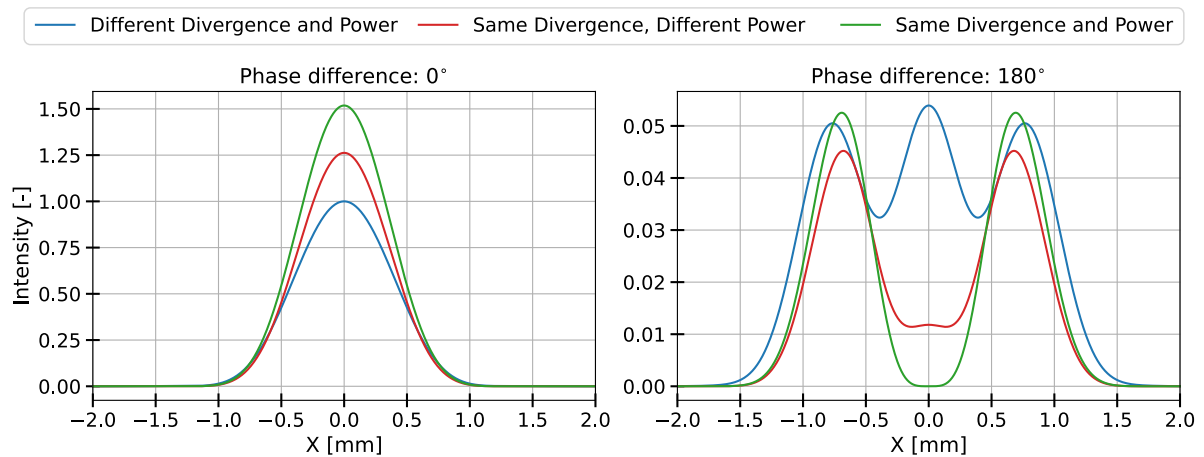


Figure B.3: Intensity across the spot seen at the photodetector, simulated for two beams with varying divergence and power. Simulations can be seen for both constructive (0°) and destructive interference (180°). With the same divergence and power, the intensity at the center of the spot becomes better for each case.

C

Additional Results

C.1. Setup render

A simple render has been made of the implemented setup, to give an impression of the system architecture in its most basic form.

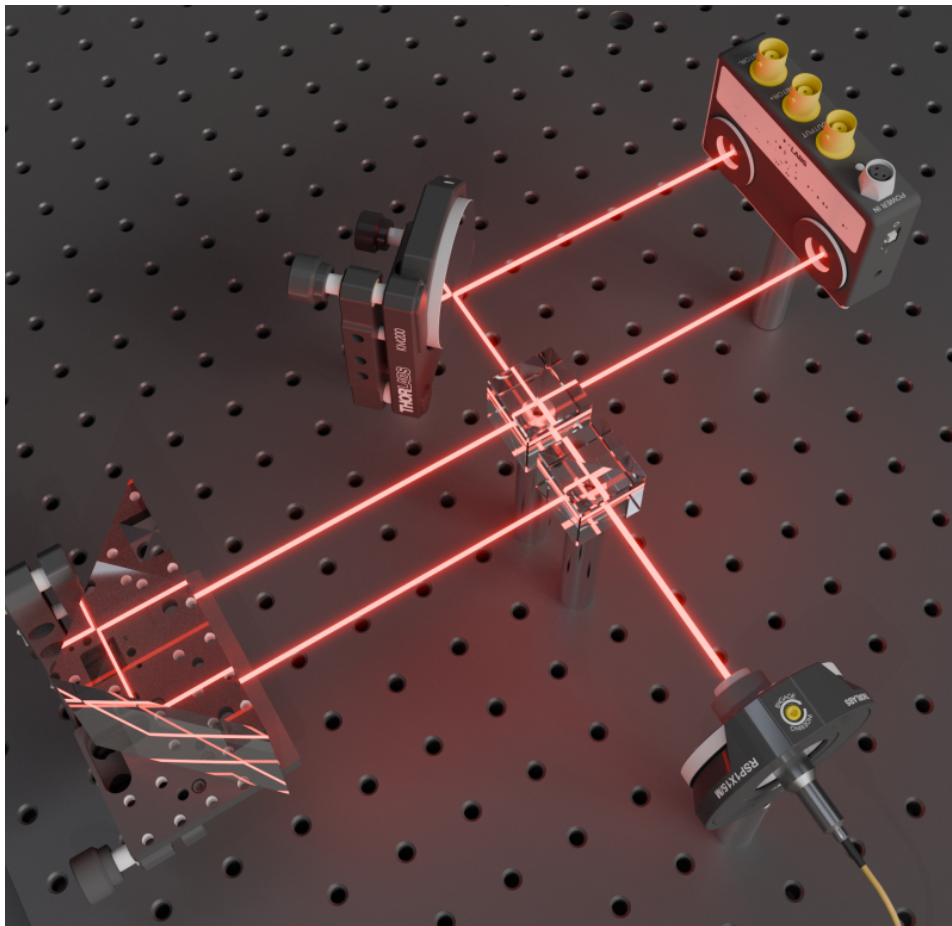


Figure C.1: Stylized and simplified rendering of the implemented hardware setup. It features the fiber mount, the two beamsplitters (shown without cage), the prism, the mirror and finally the balanced detector.

C.2. Communication performance for non-ideal conditions

The results (see chapter 4) have shown that the delay line is not stable. For most of the duration, the interference conditions are suboptimal, leading to a suboptimal output signal. An example of a waveform for single detector DPSK can be seen in Figure C.2. This particular example contains a single dip, but there are also waveforms that contain less (zero) or more dips within a 50 [ms] time span.

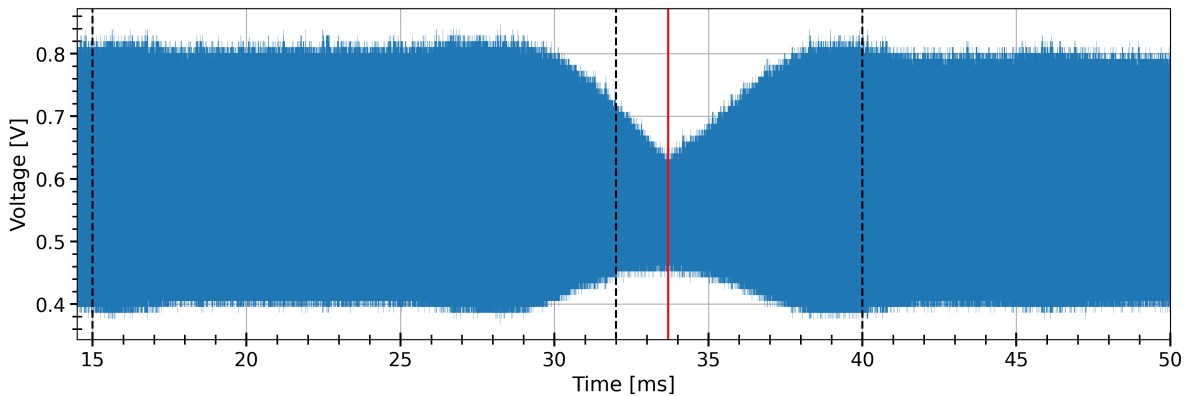


Figure C.2: Example section of a single detector DPSK waveform. The dip seen in the middle illustrates the instability the delay line experiences. The red line indicates the highest BER moment, and occurs at 33.7 [ms]. The black dashed lines indicate moments at which eye diagrams are made for illustration purposes.

At the start of the waveform, the optimal interference conditions are met, which results in a high SNR output signal. This can be seen in the eye diagram made at 15 [ms] in Figure C.3. In the transition period where the phase in the delay line is shifting, the signal still has a usable SNR, but does not resemble the shape that is expected. This can be seen in the eye diagram in Figure C.4 made at 32 [ms]. Instead of the 4 eye crossing points in the optimal signal, the new signal has 6.

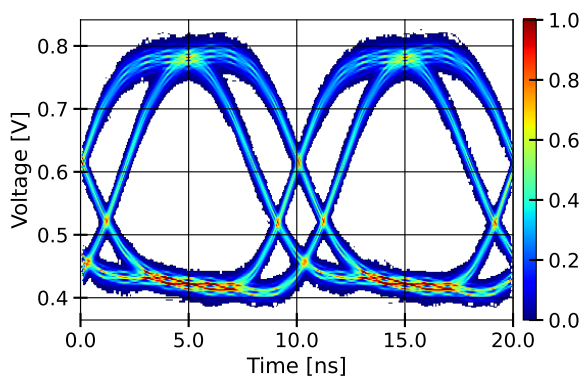


Figure C.3: Eye diagram of the DPSK waveform from Figure C.2 taken at 15 [ms].

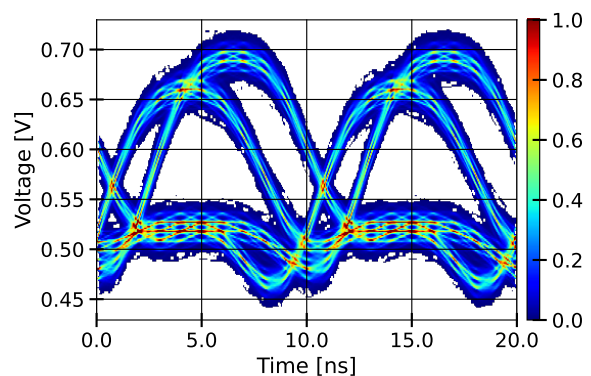


Figure C.4: Eye diagram of the DPSK waveform from Figure C.2 taken at 32 [ms].

Looking at the eye diagram at 15 [ms], the optimal sampling time occurs at 5.0 [ns]. Assuming that the drift from 15 to 32 [ms] is minimal, sampling at the same time of 5 [ns] in Figure C.4 would still allow for error-free bits. This changes the further you approach the dip. At the lowest SNR (or highest BER) moment, the signal is effectively useless. The eye diagram at this moment can be seen in Figure C.5. When sampling at the same 5 [ns] point, the distribution becomes unusable for threshold determination with the Gaussian approach, as can be seen in Figure C.6.

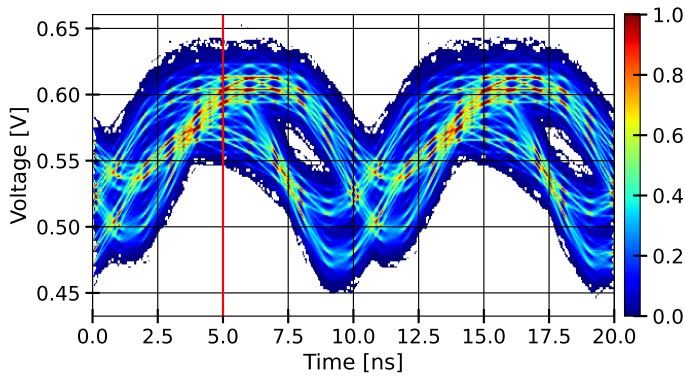


Figure C.5: 33.7ms in the waveform (exactly at the dip)

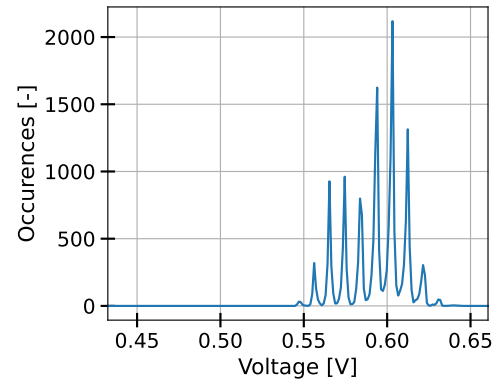


Figure C.6: Probability distribution at 5 [ns], for the signal in Figure C.5.

After the dip, the phase of the delay line approaches $\pm 90^\circ$ again. This 180° phase shift results in the bit flipping. This can be seen by comparing the signal at 15 [ms] and 40 [ms], which is shown in Figures C.7 and C.8 respectively.

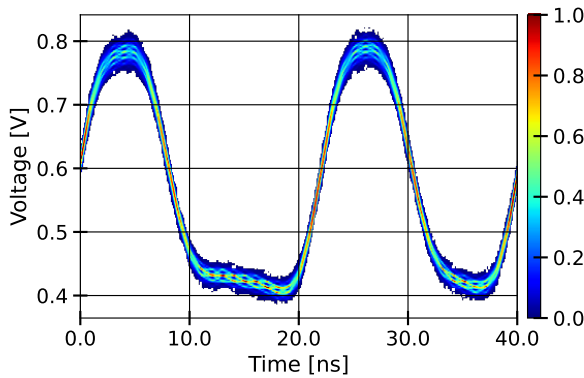


Figure C.7: Full period eye diagram at 15 ms.

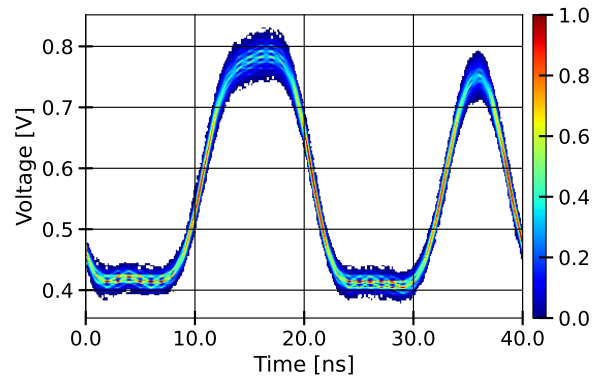


Figure C.8: Full period eye diagram at 40 ms.

This bit flip needs to be taken into account by a BER tester. This was done manually by splitting the waveform into sections and determining the BER for each one. Because changing SNR also results in a changing optimal threshold, for the most optimal case, the threshold was determined for each section individually. The results can be seen in Table C.1. For the low SNR section (33-34 [ms]), the BER is so high that the signal is useless.

Table C.1: Partial and total BER of the single detection DPSK waveform seen in Figure C.2

Time span [ms]	15-32	32-33	33-34	34-35	35-50	Total (15-50)
BER	0	0.0398	0.5166	0.1201	0	0.01933

The same analysis was also performed for the balanced detection of DPSK. An example waveform with a single dip can be seen in Figure C.9.

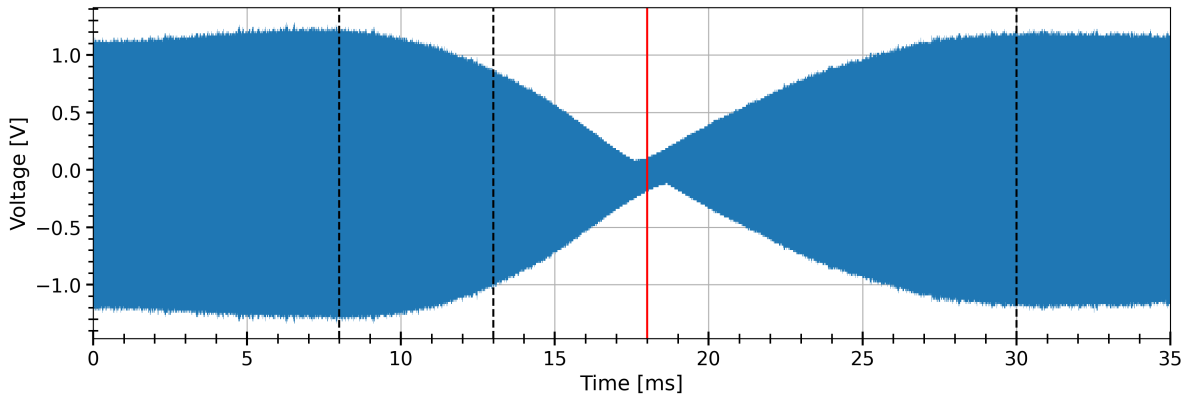


Figure C.9: Example section of a balanced detector DPSK waveform. The dip seen in the middle illustrates the instability the delay line experiences. The red line indicates the highest BER moment, and occurs at 18.0 [ms]. The black dashed lines indicate moments at which eye diagrams are made for illustration purposes.

The eye diagrams at times 8, 13 and 18 [ms] can be seen in Figures C.10, C.11 and C.12 respectively.

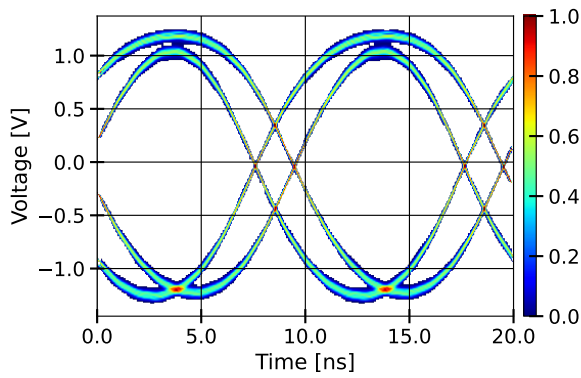


Figure C.10: Eye diagram of the DPSK waveform from Figure C.9 taken at 8 [ms].

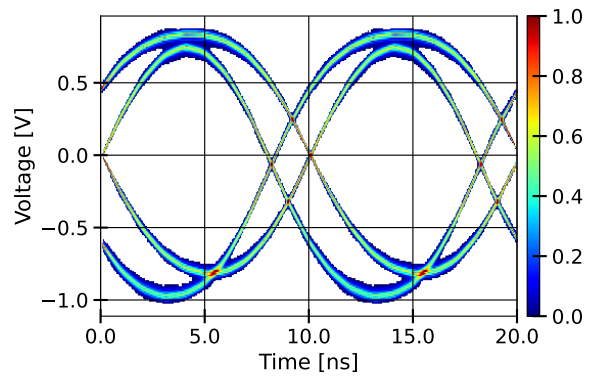


Figure C.11: Eye diagram of the DPSK waveform from Figure C.9 taken at 13 [ms].

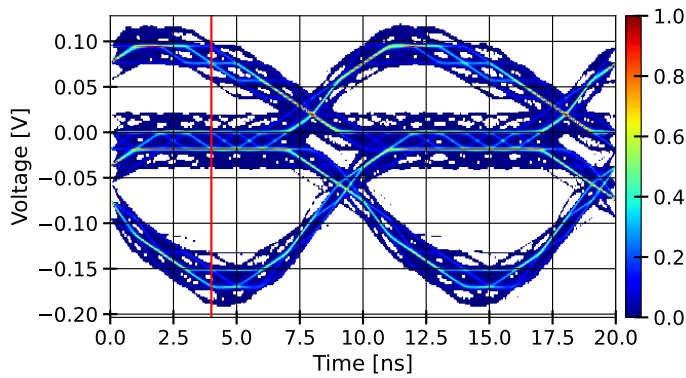


Figure C.12: 18ms in the waveform (exactly at the dip). Let us add an extra sentence to align the figures

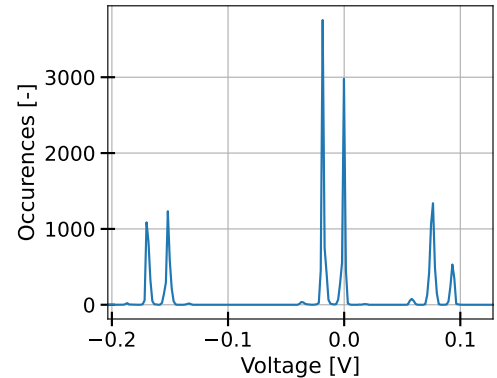


Figure C.13: Probability distribution at 4 [ns], for the signal in Figure C.12.

Again, due to a 180° phase shift in the delay line, the bits flip. This behaviour for balanced detection can be seen in Figures C.14 and C.15.

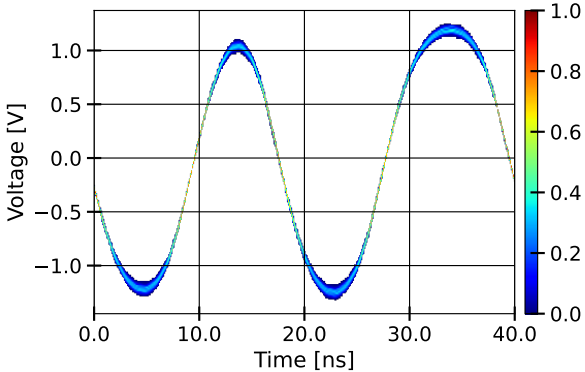


Figure C.14: Full period eye diagram at 8 ms.

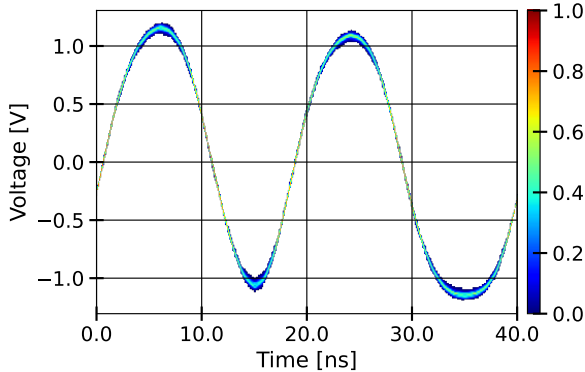


Figure C.15: Full period eye diagram at 30 ms.

Finally, the BER for the waveform was determined similarly to before. The results are summarized in Table C.2. Again, during (and close to) the dip, the BER is so high that the signal is essentially useless.

Table C.2: Partial and total BER of the balanced detection DPSK waveform seen in Figure C.9

Time span [ms]	0-16	16-17	17-18	18-19	19-20	20-35	0-35
BER	0	0	0.1397	0.2501	0	0	0.01114

C.3. Communication performance during stable conditions

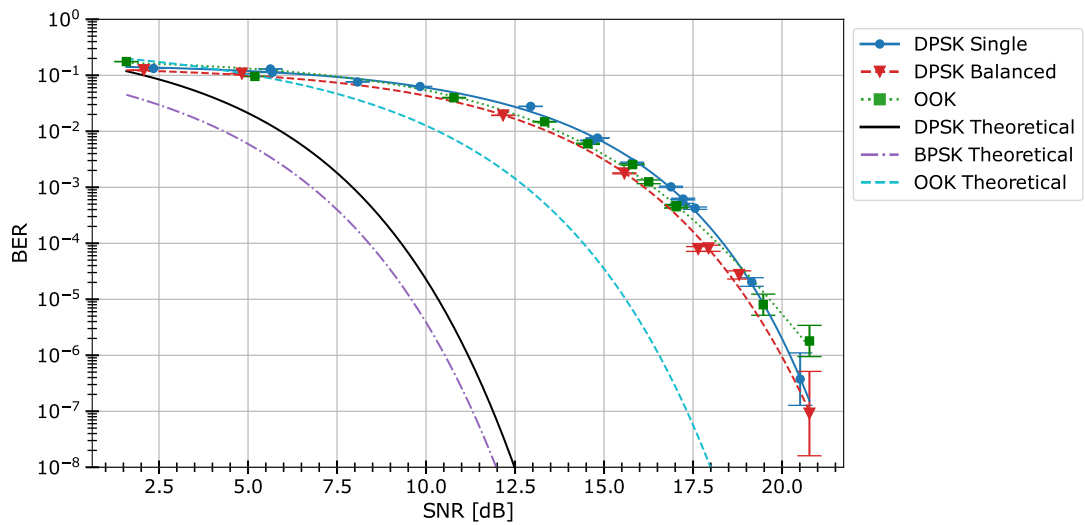


Figure C.16: BER performance of the OOK and DPSK modulation scheme. For DPSK the results for the single detector and a balanced detection setup can be seen separately.

The difference between the single- and balanced-detection DPSK signals can be seen in the figure below.

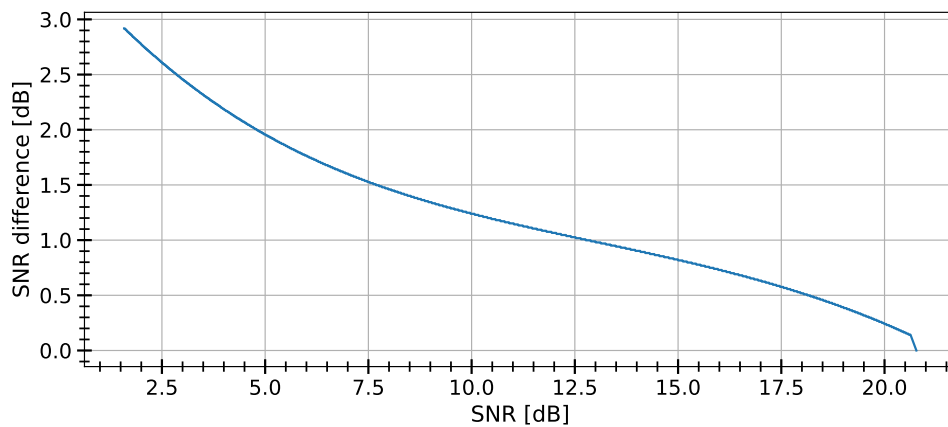


Figure C.17: SNR difference between the polynomial fits of the DPSK single detector BER performance versus the DPSK balanced detection BER performance.